Karlsruhe Institute of Technology

Liquid-liquid phase separation with phase-field method

Zur Erlangung des akademischen Grades eines
Doktors der Ingenieurwissenschaften (Dr.-Ing.)
von der KIT-Fakultät für Maschinenbau
des Karlsruher Instituts für Technologie (KIT)

angenomene **Dissertation**

von

M.Sc. Haodong Zhang

Tag der mündlichen Prüfung: 12.12.2023
Hauptreferentin: Prof. Dr. rer. nat. Britta Nestler
Korreferent: Prof. Dr. rer. nat. Dr. h.c. Lorenz Ratke

I declare that I have developed and written the enclosed thesis completely by myself, and have not used sources or means without declaration in the text.

Karlsruhe, Sept. 20, 2023

. . . .

(ZHANG, Haodong)

Abstract

This thesis extensively investigates liquid phase separation in conjunction with diverse physical fields, employing three thermodynamically consistent phase-field (PF) models designed for multi-component systems: the pure diffusion-controlled Cahn-Hilliard (CH) model, the hydrodynamically coupled Cahn-Hilliard-Navier-Stokes (CHNS) model, and the electrohydrodynamic Cahn-Hilliard-Navier-Stokes-Gauss (CHNSG) model. Building upon the beta version in Pace3D tailored for binary fluids, each model is expanded to accommodate multicomponent systems. The energy law is meticulously scrutinized, taking into account the coupling of concentration, velocity, and electrical fields, rectifying any inaccuracies in the algorithms. Of particular significance, the surface stress tensor and Maxwell stress tensor in the Navier-Stokes equations are derived and formulated in a thermodynamically consistent manner. Additionally, the requisite boundary conditions for different models are implemented in Pace3D.

Subsequently, a comprehensive examination of the numerical stability and convergence of the PF models is conducted by varying parameters such as mesh fineness (Δx), timestep (Δt), and simulation residual (EPS). Through comparisons between simulations and previous experimental results, the accuracy of the PF models is validated across three critical dimensions: (I) thermodynamics, (II) hydrodynamics, and (III) electrohydrodynamics. (I) Thermodynamic consistency for all three PF models is verified by accurately reproducing the system's phase diagram via simulation. This entails comparing correct spinodal/binodal compositions and interfacial tension with theoretical or experimental values. (II) For models coupled with hydrodynamics, a keen focus is placed on validating flow velocity and Young-Laplace pressure. (III) In the case of the CHNSG model, validation is achieved by comparing droplet deformation inside an electric field with previous analytical formulations.

Preceding the phase separation simulations, the algorithm for thermal noise in Pace3D is revisited through the investigation of droplet Brownian motion (BM). Stochastic velocity and displacement of droplets at equilibrium are compared with statistical mechanics. Notably, attention is drawn to the interface effect on BM, often overlooked in prior studies based on Einstein's rigid body assumption. Furthermore, owing to the surface stress tensor in the Navier-Stokes equation, composition fluctuations can trigger fluid flow, significantly impacting droplet coalescence behaviors, especially for small, deformable droplets at elevated temperatures, such as those generated by phase separation.

Finally, for each model, a pertinent scenario is selected and simulated. Multi-layer emulsion formation via Non-solvent-induced phase separation is studied using the CH model, Janus droplet production by thermally induced phase separation is investigated employing the CHNS model, and phase separation within electric fields is explored adopting the CHNSG model.

Zusammenfassung

Diese Dissertation untersucht umfassend die Phasentrennung von Flüssigkeiten in Verbindung mit verschiedenen physikalischen Feldern unter Verwendung von drei thermodynamisch konsistenten Phasenfeld (PF)-Modellen, die für Mehrkomponentensysteme entwickelt wurden: das reine diffusionsgesteuerte Cahn-Hilliard (CH)-Modell, das hydrodynamisch gekoppelte Cahn-Hilliard-Navier-Stokes (CHNS)-Modell und das elektrohydrodynamische Cahn-Hilliard-Navier-Stokes-Gauss (CHNSG)-Modell. Aufbauend auf der Beta-Version in Pace3D, die für binäre Fluide maßgeschneidert ist, werden die Modelle jeweils erweitert, um Mehrkomponentensysteme aufzunehmen. Das Energierecht wird sorgfältig untersucht, wobei die Kopplung von Konzentration, Geschwindigkeit und elektrischen Feldern berücksichtigt wird, um etwaige Ungenauigkeiten in den Algorithmen zu korrigieren. Von besonderer Bedeutung ist der Oberflächenspannungstensor und der Maxwell-Spannungstensor in den Navier-Stokes-Gleichungen, die auf thermodynamisch konsistente Weise abgeleitet und formuliert werden. Zusätzlich werden die erforderlichen Randbedingungen für verschiedene Modelle in Pace3D implementiert.

Anschließend wird eine umfassende Untersuchung der numerischen Stabilität und Konvergenz der PF-Modelle durchgeführt, wobei Parameter wie Maschenfeinheit (Δx), Zeitschritt (Δt) und Simulationsschwund (EPS) variiert werden. Durch den Vergleich zwischen Simulationen und früheren experimentellen Ergebnissen wird die Genauigkeit der PF-Modelle über drei kritische Dimensionen validiert: (I) Thermodynamik, (II) Hydrodynamik und (III) Elektrohydrodynamik. (I) Die thermodynamische Konsistenz für alle drei PF-Modelle wird durch die genaue Reproduktion des Phasendiagramms des Systems über die Simulation verifiziert. Dies beinhaltet den Vergleich der richtigen Spinodal-/Binodal-Zusammensetzungen und der Grenzflächenspannung mit theoretischen oder experimentellen Werten. (II) Bei Modellen, die mit Hydrodynamik gekoppelt sind, wird ein besonderer Fokus auf die Validierung von Strömungsgeschwindigkeit und Young-Laplace-Druck gelegt. (III) Im Fall des CHNSG-Modells wird die Validierung durch den Vergleich der Deformation von Tropfen innerhalb eines elektrischen Feldes mit vorherigen analytischen Formulierungen erreicht.

Vor den Phasentrennungssimulationen wird der Algorithmus für thermische Rauschen in Pace3D durch die Untersuchung der Brownschen Bewegung (BM) von Tropfen erneut überprüft. Die stochastische Geschwindigkeit und Verschiebung der Tropfen im Gleichgewicht werden mit der statistischen Mechanik verglichen. Es wird insbesondere auf den Schnittstelleneffekt auf BM hingewiesen, der in früheren Studien auf Grundlage der starren Körperannahme von Einstein häufig übersehen wurde. Darüber hinaus können durch den Oberflächenspannungstensor in der Navier-Stokes-Gleichung Konzentrationsfluktuationen Strömungen auslösen, was sich erheblich auf das Koaleszenzverhalten von Tropfen auswirkt, insbesondere für kleine, verformbare Tropfen bei erhöhten Temperaturen, wie sie bei der Phasentrennung entstehen.

Schließlich wird für jedes Modell ein relevante Szenario ausgewählt und simuliert. Die Bildung von Mehrschichtemulsionen durch Phasentrennung induziert durch Nichtlösemittel wird mit Hilfe des CH-Modells untersucht, die Produktion von Janus-Tropfen durch thermisch induzierte Phasentrennung wird unter Verwendung des CHNS-Modells untersucht und die Phasentrennung innerhalb elektrischer Felder wird unter Verwendung des CHNSG-Modells erforscht.

Acknowledgement

The completion of this dissertation coincided with my stay as a research assistant at the Institute of Applied Materials-Microstructure Modelling and Simulation (IAM-MMS) within the Karlsruhe Institute of Technology (KIT).

Foremost, I extend my appreciation to my supervisor, Prof. Dr. rer. nat. Britta Nestler. Her invaluable guidance and scientific insights were indispensable; they not only shaped my exploration of intriguing phenomena within the realm of computational material science but also granted me the opportunity to venture into diverse research domains not directly aligned with my primary project. I am profoundly grateful for her mentorship.

Special acknowledgment is due to my group leader, Dr. Fei Wang, whose exceptional patience and adeptness in elucidating intricate aspects of the phase-field model proved instrumental. His guidance in unraveling challenging equations was invaluable to my progress, especially as a newcomer in this field.

Additionally, I wish to express my lasting gratitude to Prof. Lorenz Ratke for his uplifting feedback and enlightenment, generously shared upon reviewing my initial drafts. These interactions have left a lasting impression on my academic journey.

Furthermore, I extend my gratitude to my steadfast companions, Yanchen Wu, Yuhan Cai, and Yinghan Zhao, for their camaraderie and unwavering support, particularly during the challenging times of the Covid-19 pandemic. These shared experiences are etched deep in my memory, and their support remains cherished.

I extend my appreciation to the dedicated secretarial team, including Ms. Inken Heise, Ms. Birgitt Hardt, and Ms. Michelle Ritzinger, for their valuable administrative support. Additionally, my thanks go to Mr. Christof Ratz and Mr. Domenic Frank for their technical expertise and support with computer systems.

Also, I acknowledge funding of the research through the Gottfried-Wilhelm Leibniz prize NE 822/31-1 of the German Research Foundation (DFG).

Lastly, I offer my heartfelt gratitude to my parents for the gift of life and their unending love and nurturing support throughout my journey.

Preface

This dissertation undertakes an investigation into the phase separation behaviors of multicomponent systems utilizing phase-field simulations. The inquiry commences with an exploration of the thermodynamic underpinnings of phase separation. Guided by the principle of energy minimization, the morphological transformations during the phase separation process manifest different off-equilibrium pathways significantly influenced by diverse dynamics. Integrated with assorted fields into the standard Cahn-Hilliard type of the phase-field model, three distinct models are introduced and tailored to address specific problems.

The initial model delineates phase separation dominated by diffusion, wherein material morphologies are determined by the interplay between spinodal decomposition and the minimization of surface energy. The second model incorporates hydrodynamics, enabling phase separation to be expedited through the Marangoni effect, stemming from imbalanced chemical potential. Furthermore, the fluid flow induced by phase separation also shows impacts on phase coalescence, exerting a pivotal influence during the late stages of phase separation and dramatically altering phase morphologies, encompassing parameters such as droplet size, porosity, and permeability. The third model integrates an electric field, significantly influencing the phase separation process. The fluid phases resulting from phase separation exhibit altered shapes under the influence of electrostatic forces. The dissertation meticulously explores the mechanism governing droplet deformation within the electric field and scrutinizes electric field-induced spinodal decomposition.

Additionally, a thorough investigation of thermal noise, often regarded as the initiator of phase separation yet frequently overlooked, is presented. Through the application of various noise levels to the fluid system, the interface's impact on droplet stochastic behavior is elucidated. Notably, the simulation of droplet Brownian motion reveals unexpected distinctions from classic theories pertaining to rigid bodies, as posited by Einstein and Langevin.

The first chapter provides an introduction along with the fundamental physical aspects underlying the phase separation process. The subsequent chapter extensively delves into three distinct phase-field models, emphasizing their derivations. Chapters 3-6 encompass a compilation of two published and three unpublished articles, with minor adjustments made to preserve the original content. The articles are enumerated as follows:

- **Article 1: H. Zhang**, F. Wang, and B. Nestler. Janus droplet formation via thermally induced phase separation: a numerical model with diffusion and convection. *Langmuir*, 2022, **38**(22), 6882-6895, `DOI: 10.1021/acs.langmuir.2c00308`.

- **Article 2: H. Zhang**, Y. Wu, F. Wang, F. Guo, and B. Nestler. Phase-field modeling of multiple emulsions via spinodal decomposition. *Langmuir*, 2021, **37**(17), 5275–5281, `DOI: 10.1021/acs.langmuir.1c00275`.

- **Article 3: H. Zhang**, F. Wang, L. Ratke, and B. Nestler. Brownian motion of droplets induced by thermal noise. *Physical Review E*, 2024, **109**(2): 024208, `DOI: 10.1103/PhysRevE.109.024208`.

- **Article 4: H. Zhang**, F. Wang, B. Nestler. Multi-component electro-hydro-thermodynamic model with phase-field method. I. Dielectric. *Journal of Computational Physics*, 2024, **505**: 112907, `DOI: 10.1016/j.jcp.2024.112907`.

- **Article 5: H. Zhang**, F. Wang, L. Ratke, and B. Nestler. Thermal noises are so different: the energy fluctuation and dissipation at interfaces. *In preparation.*

In the last chapter, summaries and future directions are given.

The following works were published during the Ph.D. study, and not included in the present dissertation.

- **H. Zhang**, F. Wang, and B. Nestler. Line tension of sessile droplets: Thermodynamic considerations. *Physical Review E*, 2023, **08**(5): 054121, `DOI: 10.1103/PhysRevE.108.054121`.

- **H. Zhang**, F. Wang, and B. Nestler. Electric-field induced phase separation and dielectric breakdown in leaky dielectric mixtures: Thermodynamics and kinetics. *Journal of Chemical physics*, 2024, **161**(4): 054121, `DOI: 10.1063/5.0203527`.

- F. Wang, **H. Zhang**, Y. Wu, and B. Nestler. A thermodynamically consistent diffuse interface model for the wetting phenomenon of miscible and immiscible ternary fluids. *Journal of Fluid Mechanics*, 2023, **970**, A17, `DOI: 10.1017/jfm.2023.561`.

- S.F. Kalourazi, F. Wang, **H. Zhang**, M. Selzer, and B. Nestler. Phase-field simulation for the formation of porous microstructures due to phase separation in polymer solutions on substrates with different wettabilities. *Journal of Physics: Condensed Matter*, 2022, **34**(44), 444003, `DOI: 10.1088/1361-648X/ac8b4d`.

- Z. Dong, H. Cui, **H. Zhang**, F. Wang, X. Zhan, F. Mayer, B. Nestler, M. Wegener, P.A. Levkin. 3D printing of inherently nanoporous polymers via polymerization-induced phase separation. *Nature communications*, 2021, **12**(1): 247, `DOI: 10.1038/s41467-020-20498-1`.

- F. Wang, O. Tschukin, T. Leisner, **H. Zhang**, B. Nestler, M. Selzer, G.C. Marques, and J. Aghassi-Hagmann. Morphological stability of rod-shaped continuous phases. *Acta Materialia*, 2020, **192**: 20-29, `DOI: 10.1016/j.actamat.2020.04.028`.

- F. Wang, L. Ratke, **H. Zhang**, P. Altschuh, and B. Nestler. A phase-field study on polymerization-induced phase separation occasioned by diffusion and capillary flow—a mechanism for the formation of porous microstructures in membranes. *Journal of Sol-Gel Science and Technology*, 2020, **94**: 356-374, `DOI: 10.1007/s10971-020-05238-7`.

- F. Wang, P. Altschuh, L. Ratke, **H. Zhang**, M. Selzer, and B. Nestler. Progress report on phase separation in polymer solutions. *Advanced Materials*, 2019, **31**(26): 1806733, `DOI: 10.1002/adma.201806733`.

The permission to use the figures from literature has been granted by the corresponding publishers.

Author's contribution

The supervisor for the whole project is Prof. Dr. rer. nat. Britta Nestler.

- **Article 1:** H. Zhang performed the simulations, analyzed the data, discussed with F. Wang, and wrote the draft with the feedback from F. Wang, and B. Nestler.
- **Article 2:** H. Zhang performed the simulations, analyzed the data and discussed with F. Wang. H. Zhang and Y. Wu wrote the draft with the feedback from F. Wang, and B. Nestler.
- **Article 3:** H. Zhang performed the simulations, analyzed the data, and discussed with F. Wang, and L. Ratke. H. Zhang and F. Wang wrote the draft with the feedback from F. Wang, L. Ratke, and B. Nestler.
- **Article 4:** H. Zhang and F. Wang developed the model and implement the code. H. Zhang conducted simulations. H. Zhang and F. Wang wrote the draft with the feedback from F. Wang, and B. Nestler.
- **Article 5:** H. Zhang performed the simulations, analyzed the data and discussed with F. Wang. H. Zhang wrote the draft with feedback from F. Wang, L. Ratke, and B. Nestler.

Tao (Nihil) **bears One**
(Existentia, Singularity)

One begets Two
(Yin/Yang, +/- spins)

Two breed Three
(Heaven/Earth/Creature, X-Y-Z coordinate)

Three become every things

—Lao Tzu—

Contents

Abstract i

Zusammenfassung iii

1. Introduction 1
- 1.1. Liquid-liquid phase separation 1
- 1.2. Thermodynamics 2
  - 1.2.1. free energy functional 2
  - 1.2.2. Phase diagram 5
- 1.3. Kinetics 8
  - 1.3.1. Diffusion 8
  - 1.3.2. convection 9
  - 1.3.3. Marangoni effect 11
  - 1.3.4. Droplet coalescence 11
- 1.4. Types of phase separation 11
  - 1.4.1. Thermally induced phase separation 11
  - 1.4.2. Polymerization induced phase separation 13
  - 1.4.3. Non-solvent induced phase separation 14

2. Methods 17
- 2.1. Model A: The multi-component Cahn-Hilliard model 17
  - 2.1.1. Free energy functional 17
  - 2.1.2. Evolution equation 18
  - 2.1.3. Volume conservation 19
  - 2.1.4. Energy law 20
  - 2.1.5. Interfacial tension 20
- 2.2. Model B: The multi-component Cahn-Hilliard-Navier-Stokes model 21
  - 2.2.1. Free energy functional 21
  - 2.2.2. Evolution equation 21
  - 2.2.3. Energy law 23
  - 2.2.4. Young-Laplace pressure 24
- 2.3. Model C: The multi-component Cahn-Hilliard-Navier-Stokes-Gaussian model 25
  - 2.3.1. Free energy functional 25
  - 2.3.2. Electrochemical potential 26
  - 2.3.3. Evolution equation 26
  - 2.3.4. Energy law 27
  - 2.3.5. Young-Laplace pressure and interfacial tension 29

2.4. Non-dimensionalization of the models . . . 30
2.5. Discretization and staggered mesh . . . 30
    2.5.1. Bulk region . . . 31
    2.5.2. Boundary condition . . . 33

3. Thermal noise for triggering the phase separation 35
3.1. System definition . . . 35
3.2. Simulation setup . . . 35
3.3. Model validation . . . 35
    3.3.1. Brownian coefficient measurement . . . 35
    3.3.2. Numerical convergence . . . 37
    3.3.3. Capillary wave theory . . . 38
    3.3.4. Dispersion relation . . . 39
3.4. Stochastic Cahn-Hilliard model . . . 41
    3.4.1. Anomaly of the Brownian motion with dimensions . . . 41
    3.4.2. Equipartition theorem . . . 43
    3.4.3. Noise reduction mechanism . . . 45
3.5. Stochastic Cahn-Hilliard-Navier-Stokes model . . . 47
    3.5.1. Equilibrium . . . 47
    3.5.2. Non-equilibrium . . . 49
3.6. Conclusion . . . 53

4. Multi-component phase separation induced multi-layer emulsion 55
4.1. System definition . . . 55
4.2. Simulation setup . . . 57
4.3. Model validation . . . 57
    4.3.1. Resolution . . . 57
    4.3.2. Interfacial tension of DEP and water . . . 58
    4.3.3. Selection of Flory-Huggins parameters . . . 58
    4.3.4. Validation of the phase diagram . . . 60
4.4. Results and discussion . . . 61
    4.4.1. Emulsion composition . . . 61
    4.4.2. Surface tension . . . 62
    4.4.3. Size effect . . . 64
    4.4.4. Fitting of emulsion multiplicities . . . 65
4.5. Conclusion . . . 68

5. Multi-component phase separation producing Janus droplet with hydrodynamics 71
5.1. System definition and simulation setup . . . 71
5.2. Results and discussion . . . 72
    5.2.1. The formation of Janus droplet . . . 72
    5.2.2. Radius and initial composition . . . 74
    5.2.3. Interfacial tension . . . 77
    5.2.4. Asymmetric phase separation . . . 79
    5.2.5. Fluid dynamics . . . 83

5.3. Conclusion 89

6. Multi-component phase separation inside the electric field **91**
- 6.1. System definition 91
- 6.2. Numerical stability and validation 91
  - 6.2.1. Mesh resolution 91
  - 6.2.2. Interface width-Cahn number Cn 93
  - 6.2.3. Residual threshold eps and time step 95
- 6.3. Model validation with Taylor’s theory 95
  - 6.3.1. Permittivity 96
  - 6.3.2. Conductivity 97
  - 6.3.3. Electro-capillary number 97
- 6.4. Thermodynamics with electric fields 98
- 6.5. Dynamics with capillary wave theory 100
- 6.6. Result and discussion 101
  - 6.6.1. Ternary droplet coalescence 101
  - 6.6.2. Ternary spinodal decomposition 104
- 6.7. Conclusion 105

7. Conclusion **107**
- 7.1. Conclusion and remarks 107
- 7.2. Future directions 109

A. Appendix **111**
- A.1. Non-dimensionalization 111
- A.2. List of symbols 113
- A.3. List of Abbreviations 115

Bibliography **127**

Bibliography **129**

1. Introduction

1.1. Liquid-liquid phase separation

Liquid phase separation (PS) is ubiquitous and fundamental physical phenomenon which plays a crucial significance in the both fundamental research and industrial applications. Phase separation occurs as the initially homogeneous multi-component fluid gradually undergoes differentiation into distinct phases [1, 2, 3, 4]. Here, a brief explanation is needed. The term 'phase', rooted in Plato's theory of forms, represents a highly idealized concept. It is conventionally defined as a collective of materials possessing identical physical and chemical properties. For instance, a partially filled water bottle exhibits two immiscible phases. Water droplets drawn from any location within the bottle retain consistent density, taste, smell, and transparency, regardless of the droplet size or measurement circumstances. These characteristics contrast with the air phase, which, while colorless and odorless, is nearly 800 times lighter than water. Hence, density serves as a distinguishing factor between the water and air phases. To depict the two-phase water-air system mathematically, each phase is denoted by a phase variable normalized by water density ($998\mathrm{g/m}^3$). In this representation, the water phase is assigned '1', while the air phase is labeled '0' (approximately 1.27/998). An alternative representation involves utilizing water concentration c where c=1 signifies the water phase with 100% water molecules, and c=0 denotes the dry air phase. The concentration parameter allows for the definition of miscible fluid systems, as observed in water-ethanol mixtures. In such mixtures, medical alcohol is characterized by $c = 0.75$, vodka by $c = 0.40$, Pils by $c = 0.05$. The disparity between miscible and immiscible scenarios lies in phase miscibility. Despite the distinct tastes of water and ethanol, they amalgamate into a single phase when combined, rendering the water-ethanol mixture a homogeneous single-phase system. During the Covid-19 pandemic, individuals might attempt to manufacture disinfectants by concentrating vodka at home to purify the ethanol phase. Distillation stands as the most straightforward method for phase separation — separating water from ethanol. By applying heat, volatile ethanol evaporates first. Although this disinfectant production method is not notably efficient, it underscores an intriguing physical principle. At elevated temperatures, the water-ethanol solution spontaneously segregates into a two-phase system comprising gaseous alcohol and liquid water. In fact, besides the utilization of phase separation technologies in the food industry for centuries, PS is a ubiquitous process that has been observed in diverse contexts, ranging from biological systems [5, 6, 7, 8, 9], such as the phase separation of proteins in human cell [10], to industrial processes [11, 12]. Understanding liquid phase separation enables us to elucidate the behavior of complex systems, so that the optimization and extending of its applications becomes possible and efficient. Before discussing the application, I present the fundamental theories for the phase separation process from two aspects, namely, the thermodynamics and the kinetics.

1.2. Thermodynamics

As discussed above, the essence of phase separation lies in a process commencing from an unstable, high-energy uniform single phase, progressing towards a reduction in total energy, and ultimately achieving a stable, low-energy multiphase state. Here, the stable state, especially its properties, such as composition, temperature, morphology, is the key study aspect of the thermodynamics.

1.2.1. free energy functional

1.2.1.1. Bulk free energy

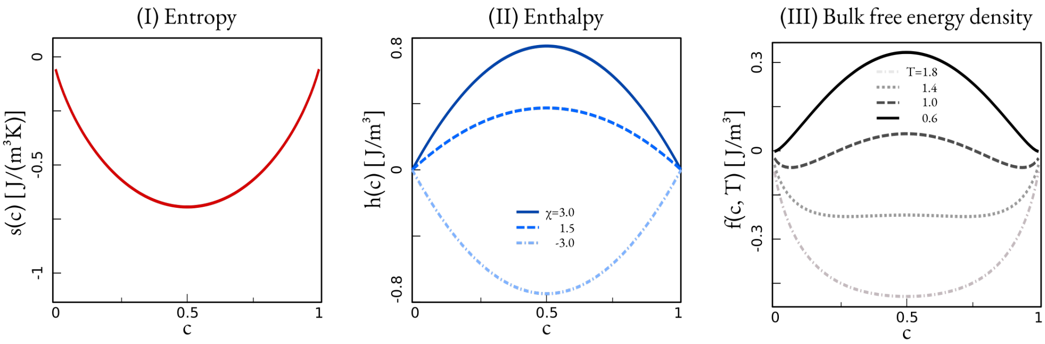

Figure 1.1.: Free energy of mixture for a binary system. (I) Entropy s as a function of the composition c. (II) Enthalpy h by different Flory parameter χ. (III) Free energy density $f = s + h$ with the increase in temperature T.

The term "energy" within the context of phase separation pertains to the mixing free energy functional of the system,

$$\mathcal{F} = T\mathcal{S} + \mathcal{H} + \mathcal{G}, \tag{1.1}$$

encompassing three fundamental components: the entropy of mixing ($\mathcal{S}$), the enthalpy of mixing ($\mathcal{H}$), and the interfacial term ($\mathcal{G}$). Following Boltzmann's theory, the mixing entropy is represented as a function of the Boltzmann constant (k_B), temperature (T), and characteristic volume (v_m),

$$\mathcal{S} = \int_\Omega s(\boldsymbol{c})\, d\Omega = \int_\Omega \frac{k_B}{v_m} \sum_{i=1}^{N} c_i \ln c_i \, d\Omega, \tag{1.2}$$

In Fig. 1.1(I), the entropy of a binary system is graphically depicted by the red line. The entropy consistently displays a global minimum at $c = 0.5$, indicating that in multi-component systems, the mixing of different substances is favorable and occurs spontaneously, aligning with the second law of thermodynamics for a closed system. Based on the lattice model demonstrate in Fig. 1.2, the enthalpy term is expressed by considering the short range interactions between components, resulting in the enthalpy term, as exemplified in the lattice model illustrated in Fig. 1.2, accounts for short-range interactions between components,

$$\mathcal{H} = \int_\Omega h(\boldsymbol{c})\, d\Omega = \int_\Omega \left(\sum_{1\le i<j}^{N,N} \chi_{ij}\, c_i\, c_j + \sum_{1\le i<j<k}^{N,N,N} \chi_{ijk}\, c_i\, c_j\, c_k + \dots \right) d\Omega, \tag{1.3}$$

involving the Flory parameter χ_{ij} which not only represents the interaction strength between different components i and j, but also has a significant impact on phase separation.

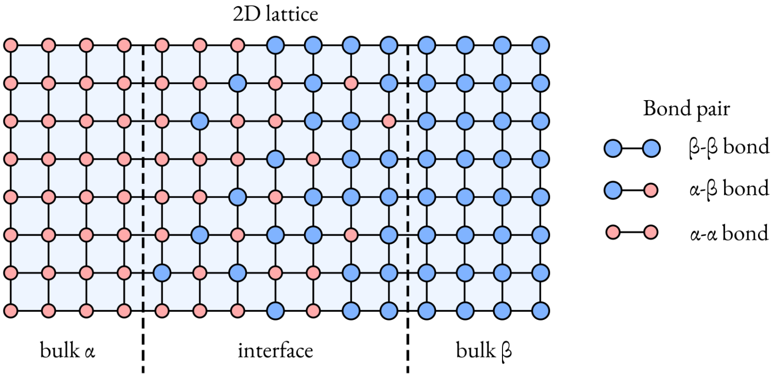

Figure 1.2.: The schematic binary lattice in 2 dimension. Red and blue dots represent the α and β molecules, respectively. The black stick connecting the dots stands for 3 different bonding types.

A more tangible understanding of χ_{ij} is derived from the bonding energy (e_{ij}) between different species.

$$\chi_{ij} = \frac{k_B T}{Z} \frac{2\, e_{ij} - (e_{ii} + e_{jj})}{2}. \tag{1.4}$$

Here, Z is the coordination number meaning how many nearest molecules has the short range interactions with the central molecule. Here, Z denotes the coordination number, signifying the number of nearest molecules with short-range interactions with the central molecule. Typically, Z is considered as 4 for 2-dimensional systems and is set to 6 in 3-dimensional cases. If $\chi_{ij} < 0$, it implies that $2e_{ij} < e_{ii} + e_{jj}$, hence the lower energy state of mixing with the bonding energy e_{ij} is more preferred than demixing $e_{ii} + e_{jj}$, and vice versa. Therefore, a positive χ_{ij} can be construed as repulsive enthalpic interaction, while a negative value denotes attraction. Evidently, phase separation is highly associated with a positive enthalpy of mixing.

Combining the entropy contributions, the summation of s and h is denoted as the bulk free energy f, illustrated in Fig. 1.1(III) for various T in a binary system. Due to the entropy effect, the sign of χ_{ij} alone cannot dictate molecular interactions or phase separation, especially at higher temperatures where the entropy term becomes more pronounced (see Fig. 1.1(I)), as demonstrated by the grey dot-dashed line at $T = 1.8$ in Fig. 1.1(III). Mathematically, a critical point exists, defined by the second derivative of f with respect to the composition $\boldsymbol{c} = (c_1, c_2, \ldots, c_N)$

$$\frac{\partial^2 f}{\partial \boldsymbol{c}^2} = \det \begin{vmatrix} \frac{\partial^2 f}{\partial c_1^2} & \frac{\partial^2 f}{\partial c_1 \partial c_2} & \cdots & \frac{\partial^2 f}{\partial c_1 \partial c_N} \\ \frac{\partial^2 f}{\partial c_1 \partial c_2} & \frac{\partial^2 f}{\partial c_2^2} & \cdots & \frac{\partial^2 f}{\partial c_2 \partial c_N} \\ \vdots & \vdots & \ddots & \vdots \\ \frac{\partial^2 f}{\partial c_1 \partial c_N} & \frac{\partial^2 f}{\partial c_2 \partial c_N} & \cdots & \frac{\partial^2 f}{\partial c_2 \partial c_N} \end{vmatrix} = 0, \tag{1.5}$$

constituting a quadratic function of $\boldsymbol{c}$, T, and χ_{ij}. By fixing the Flory parameter χ_{ij}, a composition pair fulfilling Eq. (1.5) is determined at different temperatures T, akin to finding the eigenvalue of the Hessian matrix in Eq. (1.5). Particularly, at a specific temperature, the Hessian matrix possesses only one eigenvalue. This temperature is termed the critical temperature T_c, above which the quadratic function Eq. (1.5) lacks a root, as seen by the red dot in Fig. 1.3(II). Given that the critical point occurs precisely at $c = 0.5$, the critical temperature of a binary system is easily computed as

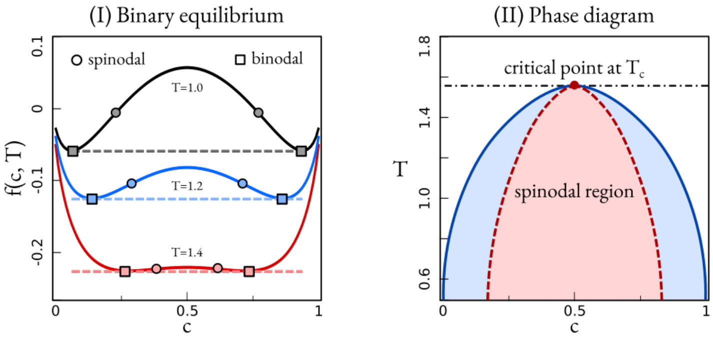

Figure 1.3.: (I) The free energy density of a binary system and the equilibrium with the dashed common tangent lines for various temperatures. Square: equilibrium binodal compositions; circle: spinodal compositions. (II) The $c - T$ phase diagram corresponding to (I).

$$T_c = \frac{v_m}{2\, k_B}\, \chi, \tag{1.6}$$

beyond which no phase separation can occur, and all components are homogeneously mixed in a single phase. For $T \leq T_c$, the composition pair fulfilling Eq. (1.5) are termed spinodal compositions, delineated by the red dashed spinodal lines in Fig. 1.3(II) for a binary system. The light red region enclosed by these spinodal lines is referred to as the spinodal region, wherein the homogeneous mixing of all components is thermodynamically metastable. With the presence of slight thermal fluctuations, the system reduces its energy by initiating the phase separation process, also referred to as spinodal decomposition.

1.2.2. Phase diagram

An inquiry may arise regarding the extent to which phase separation ceases. Physically, the destination of phase separation is referred to as equilibrium, deriving from the Latin words 'aequus' (equal) and 'libra' (balance). Etymologically, 'equilibrium' conveys that the various separated phases are all thermodynamically equal. Mathematically, the equilibrium state can be described by the following equations

$$\frac{\partial f}{\partial \boldsymbol{c}_\alpha} = \frac{\partial f}{\partial \boldsymbol{c}_\beta} = \boldsymbol{\mu}^e, \tag{1.7}$$

$$f(\boldsymbol{c}_\alpha) - \boldsymbol{\mu}^e \boldsymbol{c}_\alpha = f(\boldsymbol{c}_\beta) - \boldsymbol{\mu}^e \boldsymbol{c}_\beta. \tag{1.8}$$

Here, α and β can represent any phases existing at equilibrium, with equilibrium compositions denoted as $\boldsymbol{c}_\alpha = (c_{1\alpha}, c_{2\alpha}, \cdots, c_{N\alpha})$, $\boldsymbol{c}_\beta = (c_{1\beta}, c_{2\beta}, \cdots, c_{N\beta})$ are denominated as the binodal compositions. Schematically illustrated in Fig. 1.3(I), the binodal composition of a binary system at a given temperature is calculated by the colored dashed common tangent line of f, forming the blue binodal lines in Fig. 1.3(II). The phase separation process ceases when all phases reach their respective equilibrium compositions on the binodal lines. However, the essence of phase separation is fundamentally determined by the term $\boldsymbol{\mu}^e = (\mu_1^e, \mu_2^e, \cdots, \mu_N^e)$ in Eq. (1.7), denoted as the chemical potential. According to the Gibbs-Duhem equation, under an isotherm and isobaric conditions, phase separation only halts when the equilibrium chemical potential $\boldsymbol{\mu}^e$ is reached for all phases. In other words, phase separation occurs if the chemical potential μ_i in any phase for any component i is not equal to the equilibrium μ_i^e.

Furthermore, the triple interaction parameter χ_{ijk} for ternary systems in Eq. (1.3) is not discussed. Given that the diffusion equation and Fokker-Planck equation are equivalent, the concentration c_i can be analogized as a probability of finding a component i molecule at position $\boldsymbol{x}$ and time t. Consequently, the term $c_i c_j c_k$ interpreted as the joint probability or conditional probability of finding a component i molecule when the probabilities of existing the j molecule and k molecule at the same position are c_j and c_k, respectively. χ_{ijk} functions as a scaling factor, converting the conditional probability into energy density. Phenomenologically, larger χ_{ijk} indicates a more intense energy requirement for placing an i molecule at the position $\boldsymbol{x}$ where j and k molecules already exist. In other words, $\chi_{ijk} > 0$ can be interpreted as repulsive triple interactions. However, unlike the Flory parameter χ_{ij}, the magnitude of χ_{ijk} is unknown for most multicomponent systems. Typically, it is set to a positive man-made value to penalize the co-existence of three components in a specific region, especially at triple junctions. Here, it is suggested that the triple interaction parameter χ_{ijk} contributes to the system's energy and may play a vital role in microscopic droplet systems, such as the line tension effect for nanoscale sessile droplets and liquid lenses.

1.2.2.1. Interfacial free energy functional

The foregoing section provided a concise discussion on the thermodynamics of bulk regions, where free energy is primarily described by the entropy $\mathcal{S}$ and enthalpy $\mathcal{H}$. Now, attention is directed towards the interface region, which has its own energy contribution $\mathcal{G}$

to the system in the free energy functional Eq. (1.1). The mathematical expression for this term is deduced by J.W. Cahn in his ground-breaking paper [13]. An alternative derivation of the classic Cahn-Hilliard theory is presented as follows.

In Fig. 1.2, the interface between phase α and β is depicted by a mixture of red and blue molecules. Eq. (1.2) describes the entropy of a homogeneous cell assumed to have composition c. However, for materials at the interface, the composition gradually transitions from the equilibrium compositions c_α to c_β, as shown in Fig. 1.4. The cell boundaries, marked by dashed lines, have different compositions from the cell center. The composition at the boundary positions is taken as the mean average of the adjacent cells. For instance, at the boundary of cells 3 and 4, the composition is $c_3 + dc = c_4 - dc$. Consequently, the entropy at the interface is derived from the cell center. Employing a first-order approximation, the entropy at the interface is expanded using a Taylor series, resulting in

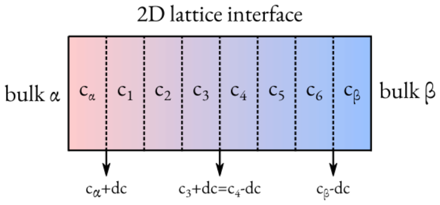

Figure 1.4.: The schematic lattices at the interface. The composition varies from red α phase to blue β phase. At the black dashed cell boundaries, c deviates from the cell center by dc.

$$\begin{aligned} s_b &= (c + dc)\ln(c + dc) + \Big(1 - c - dc\Big)\ln\Big(1 - c - dc\Big) \\ &= c\ln c + \Big(1 - c\Big)\ln\Big(1 - c\Big) - \frac{(dc)^2}{2\,c(1 - c)}, \end{aligned}$$

where the odd terms of dc are canceled due to the reflection symmetry of $\boldsymbol{x} \longrightarrow -\boldsymbol{x}$. Similarly, the enthalpy term is also expanded as

$$h_b = \chi(c + dc)(1 - c - dc) = \chi c(1 - c) - \chi(dc)^2.$$

Therefore, the energy density changed by the interface yields

$$\Delta f = (s + h) - (s_b + h_b) = \Big(\frac{k_B T}{2c(1 - c)v_m} + \chi\Big)\epsilon^2(\nabla c)^2.$$

And the interfacial energy term is written as

$$\mathcal{G} = \int_\Omega \Delta f d\Omega = \int_\Omega \kappa\,\epsilon^2(\nabla c)^2 d\Omega.$$

Here, the interfacial tension parameter is denoted as $\kappa = k_B T/[2c(1 - c)v_m] + \chi$ and ϵ is the interface width parameter with $dc = \epsilon\nabla c$. At the temperature far below the critical temperature T_c, the entropy effect can be neglected and $\kappa \approx \chi$, reflecting the relation between macroscopic interfacial tension and microscopic intermolecular forces.

1.2.2.2. Flory-Huggins theory

In the free energy density expressions of Eqs. (1.2) and (1.3), where Van der Waals forces are considered as the intermolecular interactions, represent a type of free energy density formulation known as the regular solution model. In contrast, polymer chains comprise monomers (large blue dots) connected by covalent bonds (dark blue lines), as schematically shown in Fig. 1.5(I). Due to the new chemical bonds, the polymer chain is less flexible than the monomers and has a reduced entropy formulation, known as Flory-Huggins theory, expressed as

$$\mathcal{S} = \int_{\Omega} \frac{k_B T}{v_m} \sum_{i=1}^{N} \frac{c_i \ln c_i}{N_i} \, d\Omega, \tag{1.9}$$

in which N_i is the degree of polymerization (DP) of component i. For non-polymers, $DP = 1$. Notably, the deduction of Eq. (1.9) by Flory is based on the Gauss chain assumption, allowing for intersections of polymer chains with zero entanglement, as highlighted by the red dashed square in Fig. 1.5(I). This assumption is valid for polymer solutions near the critical temperature T_c or melting polymers. Consequently, the polymer solution in Flory-Huggins theory results in an asymmetric free energy and phase diagram in Fig. 1.5(II) and (III).

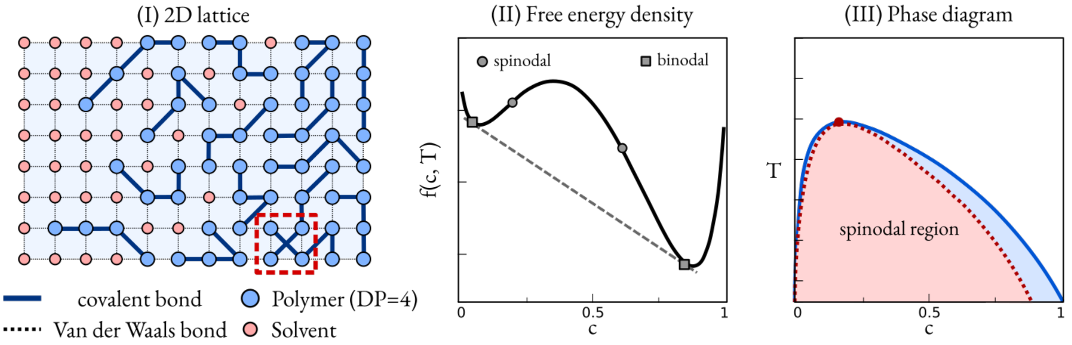

Figure 1.5.: Flory-Huggins theory for the binary polymer solution. (I) The schematic polymer solution in 2 dimensional lattice. The degree of polymerization (DP) is 4. Red and blue dots represent the solvent and monomer molecules, respectively. The dark blue stick connecting the monomers stands for covalent bond and the thin dashed line indicates the Van der Waals bond. The red square highlights the entanglement. (II) Free energy density with spinodal and binodal compositions. The common tangent line decides the equilibrium. (III) Phase diagram.

Compared with the free energy f and phase diagram of the regular solution model in Fig. 1.3, The polymerization, as opposed to the non-polymers, reduces the entropy on the polymer-dense side (large c), so that both f and PD becomes asymmetric to the composition, thus drastically influencing phase separation behavior. For instance, the spinodal and equilibrium composition shown in Fig. 1.5(II)(III) become lopsided for the polymer solution with $N = 4$. Moreover, the tilted common tangent line not only moves the equilibrium compositions, but also indicated the equilibrium chemical potential $\mu_e \neq 0$

which has a great impact on the surface stress tensor in the momentum balance equations (discussed later in Sec. 2.2 of chapter 2).

Another distinction in polymeric phase separation is that the polymer reaches its equilibrium composition c_p over a much longer time t_p than the solvent matrix t_s, as demonstrated in Fig. 1.6. Therefore, in addition to thermodynamics, the kinetics of phase separation are also prominent in determining system morphologies and will be discussed in next section.

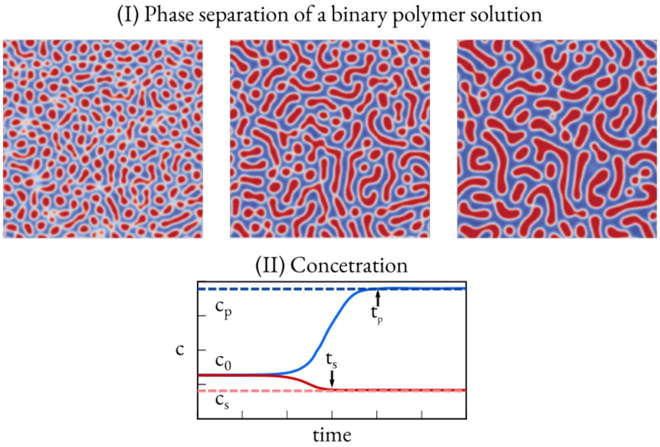

Figure 1.6.: Morphological transition of a binary polymer solution from Ref. [14]. Reproduced with permission. Copyright 2017, American Physical Society. The blue and the red areas represent polymer-rich and solvent-rich phases, respectively. (I) Phase separation with time. (II) The delayed equilibrium of polymer phase which reaches the equilibrium composition c_p slower than the solvent phase ($t_s < t_p$).

1.3. Kinetics

In the preceding section, a succinct discussion on the thermodynamics of phase separation was presented, elucidating the ultimate trajectory of the phase transformation. However, in reality, the final morphology is also highly dependent on kinetics, particularly diffusion and convection.

1.3.1. Diffusion

Commencing with the classic physical model for diffusion, Fick's law describes the microscopical diffusion flux $\boldsymbol{j}_d$, stemming from the composition gradient as

$$\frac{\partial c}{\partial t} = \nabla \cdot (-\boldsymbol{j}_d), \tag{1.10}$$

$$\boldsymbol{j}_d = \mathcal{D} \nabla c. \tag{1.11}$$

where $\mathcal{D}$ stands for the interdiffusivity. However, this equation is inadequate for elucidating the phase separation process, during which uphill diffusion with negative $\mathcal{D}$ happens. Instead of the composition gradient, the chemical potential gradient serves as the driving force for phase separation, with the composition evolving as

$$\frac{\partial c}{\partial t} = \nabla \cdot (-\boldsymbol{j}_d) = \nabla \cdot (\mathcal{M}\nabla\mu), \tag{1.12}$$

$$\mu = \frac{\delta\mathcal{F}}{\delta c} = \frac{\partial(s+h)}{\partial c} - 2\kappa\epsilon^2\nabla^2 c. \tag{1.13}$$

Here, the functional derivative follows

$$\frac{\delta}{\delta c} = \frac{\partial}{\partial c} - \nabla \cdot \frac{\partial}{\partial(\nabla c)} + \nabla^2 \cdot \frac{\partial}{\partial(\nabla^2 c)} + \cdots + (-1)^n \nabla^n \cdot \frac{\partial}{\partial(\nabla^n c)}. \tag{1.14}$$

Comparing Eq (1.12) with Eq.(1.11), the relation between the mobility and diffusivity is derived as

$$\mathcal{M} = \frac{\mathcal{D}}{\partial\mu/\partial c} = \frac{\mathcal{D}}{\partial^2 f/\partial c^2}. \tag{1.15}$$

Importantly, this relationship necessitates a one-to-one mapping (bijection) between μ and c, valid only for miscible liquid systems. Furthermore, this relationship explains the delayed phase separation behavior observed in polymeric solutions, as shown in Fig. 1.6. For polymer and solvent phases reaching their individual equilibrium compositions, the kinetic speed is dominated by the mobility $\mathcal{M}$, scaled by the thermodynamic-related factor $\partial^2 f/\partial c^2$. Apparently illustrated in Fig. 1.3(II), different curvatures of the free energy density f at the polymer and solvent equilibrium compositions (squares) are noticeable, resulting in different second derivative values ($\partial^2 f/\partial c^2$). In this way, the larger $\partial^2 f/\partial c^2$ for polymer densed phases leads to smaller mobility and slower phase separation speed than the solvent phase.

1.3.2. convection

In some multicomponent liquid systems, pronounced fluid flows are observed, such as the droplets inside microfluidic devices in Fig. 1.7. The phase separation can thus be influenced by convection, which transports material through another flux term $\boldsymbol{j}_c$ as

$$\frac{\partial c}{\partial t} = \nabla \cdot (-\boldsymbol{j}_c - \boldsymbol{j}_d) = \nabla \cdot (-\boldsymbol{u}c + \mathcal{M}\nabla\mu), \tag{1.16}$$

$$\mu = \frac{\delta\mathcal{F}}{\delta c} = \frac{\partial(s+h)}{\partial c} - 2\kappa\epsilon^2\nabla^2 c. \tag{1.17}$$

In this context, the fluid velocity denoted by $\boldsymbol{u}$, which accelerates the particle system (PS), is induced by the so-called Marangoni effect.

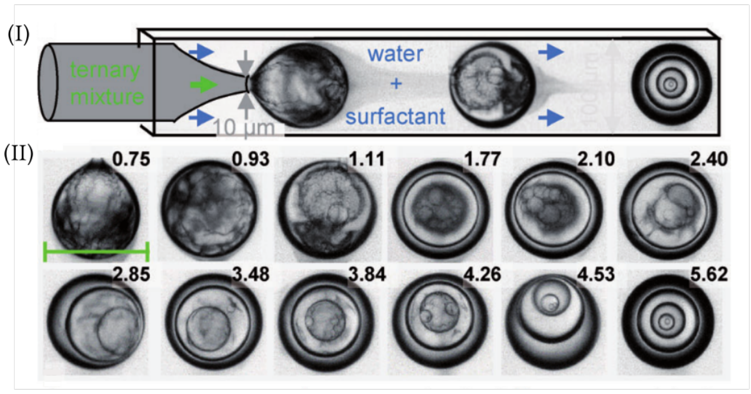
(I)
ternary mixture
water
+
surfactant
10 µm
100 µm
(II)
0.75
0.93
1.11
1.77
2.10
2.40
2.85
3.48
3.84
4.26
4.53
5.62

Figure 1.7.: Morphological transition of a ternary DEP/ethanol/water solution from Ref. [15]. Reproduced with permission. Copyright 2014, Wiley-VCH Verlag GmbH & Co. KGaA, Weinheim. (I) Schematic illustration of a microfluidic glass capillary. (II) Formation of a quintuple droplet over time (in seconds) from a ternary DEP/ethanol/water mixture (0.41/0.42/0.17 vol %).

(I) Fluid flow inside the droplet

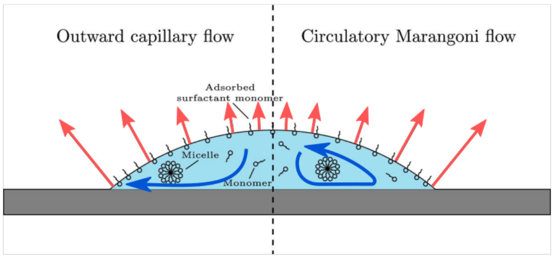
Outward capillary flow
Circulatory Marangoni flow
Adsorbed surfactant monomer
Micelle
Monomer

(II) Pattern fomation via Marangoni effect

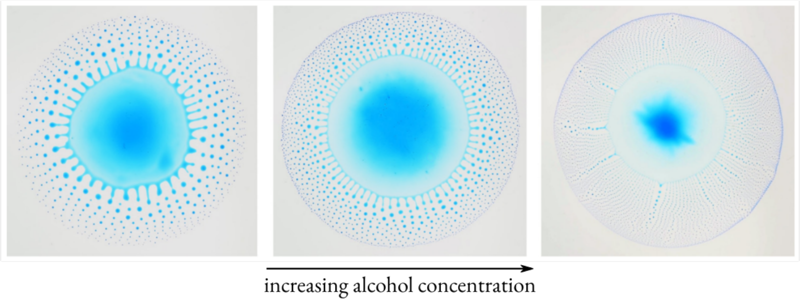
increasing alcohol concentration

Figure 1.8.: (I) Schematic illustration of the evaporation induced surfactant inhomogeneity causes fluid flows from Ref. [16]. Copyright 2020 The Author(s). Published by Elsevier Inc. (II) Formation of multiple ejected droplets from the central large drop via phase separation with Marangoni effect from Ref. [17]. The mass fraction of alcohol is increased from 0.4 (left) to 0.5 (right), which decreases the size of the ejected droplets.

1.3.3. Marangoni effect

The Marangoni effect is fundamentally characterized as the transfer of material along an interface between two phases due to a surface tension gradient. In Fig. 1.8(I), for instance, evaporation of solvent (depicted by the red arrows) leads to a concentration difference of surfactants within the droplet, triggering the fluid flow (illustrated by the blue arrows).

The Marangoni effect can also be combined with the phase separation and create different morphologies, as shown in Fig. 1.8(II). Here, the blue ink/alcohol solution is slightly heated and the volatile alcohol being evaporated, bring the system into the metastable spinodal region and propels PS. Additionally, the surface tension gradient between the thin edge and thick center engenders the Marangoni effect which ejects the PS produced tiny droplets away from the center. By changing the alcohol concentration inside the initial drop, the magnitude of the Marangoni effect, as well as the phase separation region, are also altered accordingly which modifies the different patterns consisted of tiny droplets with diverse radii.

1.3.4. Droplet coalescence

The fluid flow not only impacts droplet formation during the phase separation process but also instigates droplet coalescence [18, 19]. As depicted in Fig. 1.9(I), the PS produced droplets are merging with each other which results in large drops in the end. Here, three mechanisms are attributed to the droplet coalescence, namely, the slow Ostwald ripening via diffusion [21], the droplet Brownian motion with thermal noises, and the rapid Tanaka-Golovin mechanism by convection. Actually, the droplet motion is mainly consisted of two aspects. Due to the thermal noises, the Brownian motion can continuously drift the droplet, as shown in the left panel of Fig. 1.9(II).

The rapid Tanaka-Golovin mechanism moves the droplet with a deterministic way which can be clearly seen in the droplet trajectories in Fig. 1.9(III). The droplet coalescence via Tanaka-Golovin mechanism can be seen by plotting the mean radius $\bar{R}$ versus the normalized time $\tilde{t}$ in Fig. 1.9(IV) which shows the linear tendency of $\bar{R} \sim \tilde{t}$, totally different from the $1/3$ scaling law for Ostwald ripening and Brownian motion. The primary mechanism driving droplet coalescence is attributed to the unbalanced chemical potential. Within the gap between two droplets, the concentration is higher than outside the gap due to overlapping concentration profiles shown in the right panel of Fig. 1.9(V). The concentration disparity, indicated by the green horizontal lines, generates an unbalanced chemical potential,initiating droplet motion. Theoretically, the Tanaka-Golovin mechanism is essentially an alternative interpretation of the Marangoni effect. A detailed mathematical model describing the Marangoni effect is documented in Sec. 2.2 of chapter 2.

1.4. Types of phase separation

1.4.1. Thermally induced phase separation

Thermally induced phase separation (TIPS) manifests the phase separation driven by temperature changes. This phenomenon finds its application in many diverse fields, ranging

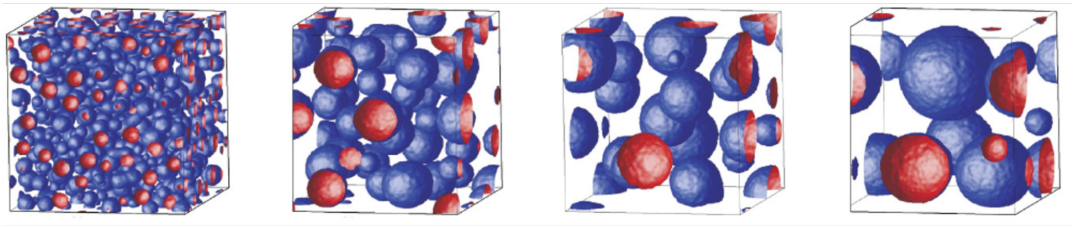
(I) Binary phsese paration with hydrodynamics

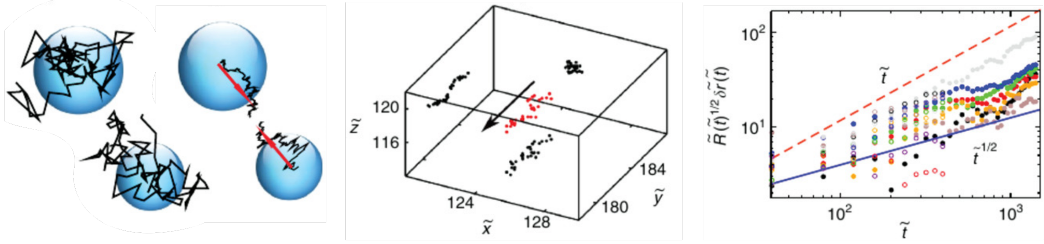
(II) Droplet motion

(III) Deterministic motion

(IV) Mean radius vs. time

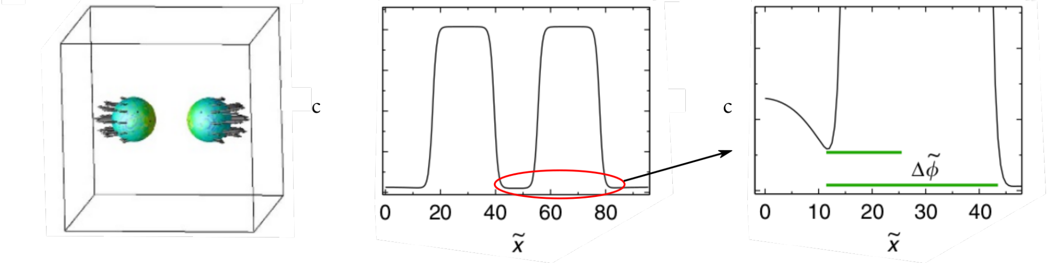
(V) Droplet motion induced by concentration overlapping

Figure 1.9.: Spontaneous motion of droplets. (I) Phase separation microstructures at different times with an initial concentration $c_0 = 0.25$. (II) Schematic pictures for random and directional motions, respectively. (III) An example of single droplet trajectories from the microstructures shown in (II). (IV) Symbols with different colors depict the dimensionless displacements of different droplets shown in (II) as a function of time. The blue straight line illustrates the displacement from Brownian motion and the red dashed line has a slope of 1 corresponding to Marangoni effect. (V) The double droplet motion. Left: Simulation snapshot. Mid: the composition profile of the droplets along the line connecting their centres of mass for two droplets. Right: Enlargement of the composition profile of the left droplet. Reproduced with permission. [20] Copyright 2015, Springer Nature.

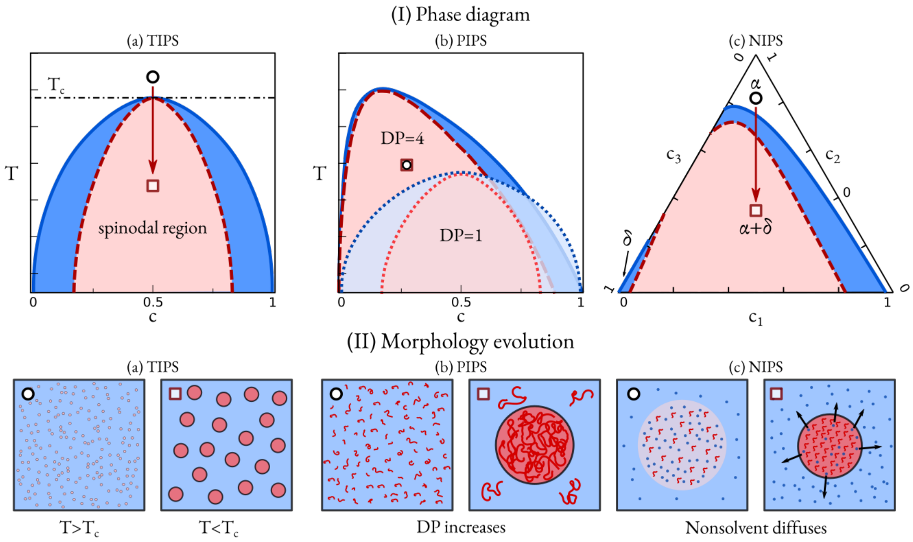

Figure 1.10.: Three types of phase separation. (I) Phase diagram. (a) Thermally induced phase separation (TIPS); (b) polymerization induced phase separation (PIPS); (c) non-solvent induced phase separation (NIPS). The open black circle and red square denote the start and end state, respectively. (II) Schematic pictures for phase separation with time.

from material sciences to environmental engineering. Understanding the thermodynamics and kinetics of TIPS enables us to extent its potential for tailored material design and efficient industrial processes. Thermodynamically, PS is driven by composition fluctuations which stems from perturbations in chemical free energy functional Eq. (1.1). As shown in the phase diagram in Fig. 1.10(I)(a), when a homogeneous system (open dot) experiences temperature drop from temperature above the critical temperature T_c to $T < T_c$, the enthalpic and entropic contributions to chemical free energy undergo a discernible changes. As entropy loses its importance with decreasing T, the enthalpy becomes more pronounced which enhances repulsive interactions between different species. The balance between enthalpic and entropic in the wake of temperature changes brings the system into the metastable region where PS starts which results in the emergence of tiny droplets and their coalescence, as shown in Fig. 1.10(II)(a). Understanding TIPS has far-reaching implications across several disciplines.

In engineering, the precise control over temperature enables us to achieve the phase separation which allows for the design and fabrication of composite materials with properties, including enhanced strength, or optical characteristics [22]. A deep understanding on TIPS is also vital in the medical field, where TIPS can be applied to formulate drug delivery systems with controlled release profiles [23, 24, 25].

1.4.2. Polymerization induced phase separation

Polymerization-induced phase separation (PIPS) takes place within polymeric systems [26], characterized by the demixing of monomers during forming long polymer chains via polymerization, and results in the formation of polymer-riched and polymer-lean phases with different compositions. The principles of polymerization-induced phase separation is governed by interplay of thermodynamic, kinetic and reaction. Here, considering the polymerization reaction speed orders faster than diffusion, the formation of long chain from monomers is mimic via assigning the degree of polymerization DP as a function of time t. At the onset of polymerization, the entropy of the long polymer chains decreases with the polymerization reaction which curtails the mixing tendency of polymer with solvent, as guided by the Flory-Huggins theory Eq. (1.9). Concurrently, the enthalpy which is related to molecular interactions dominates. Consequently, with the increase in DP, the metastable region expands [27] and the homogeneous mixing at small DP enters the spinodal region at large DP; see Fig. 1.10(I)(b). Resulting from this, the assemble of long polymer chains generates the polymer densed droplet, as demonstrated in Fig. 1.10(II)(b).

In applications, by controlling the polymerization conditions, such as monomer composition, polymerization speed, temperature, various morphologies which directly translate into desired mechanical, thermal, and biological properties, can be achieved. Furthermore, PIPS holds promise in finding new receipts for the development of new materials in many sophisticated applications. With a deeper understanding of the principles, as well as kinetics, the potential for tailored materials with enhanced functionality and performance is substantially heightened, making PIPS a focal point of academic research and industrial innovation.

1.4.3. Non-solvent induced phase separation

Non-solvent induced phase separation (NIPS) represents a phase separation process wherein the diffusion of non-solvent molecules into the matrix phase prompts the separation of phases, as illustrated in Fig. 1.10(II)(c). Due to the different solubility of the blue tiny non-solvent molecules in droplet and matrix, the diffusion brings the system from the white one phase region into the pink metastable area, as shown in the phase diagram Fig. 1.10(I)(c).

Non-solvent-induced phase separation serves as a versatile platform for designing and fabricating functional materials, encompassing a broad spectrum of applications in medical field and food industry. Modifying the solubility of non-solvent molecules across various phases, achieved through techniques like pH adjustments and surfactant addition, affords precise control over phase separation processes. Moreover, non-solvent-induced phase separation (NIPS) can be synergistically employed in conjunction with polymer-induced phase separation (PIPS) and temperature-induced phase separation (TIPS), where polymerization and temperature alterations further modify solubility. This suggests the coexistence or domination of TIPS, PIPS, and NIPS within the same system, influencing phase separation at different stages for distinct compositions and under varying conditions. Such interactions prove intricate and demand careful consideration during experimental investigations.

In contrast, computer simulations facilitate the handling of complex systems. By selecting appropriate simulation parameters in corresponding mathematical models, researchers can meticulously examine the intensity and extent of diverse phase separation mechanisms—an endeavor often unfeasible in experimental setups. Particularly, spatial and temporal properties, such as local composition distribution, transient fluid velocity, which are challenging to measure experimentally yet crucial for elucidating the underlying mechanisms, can be readily traced and scrutinized through simulation. Consequently, in the ensuing chapters, I introduce and employ the phase-field method to delve into the intricacies of the phase separation process.

2. Methods

In this chapter, three different phase-field (PF) models are presented which are correlated with respective problems, namely,

- (I) The multi-component Cahn-Hilliard (CH) type PF model deals with the standard phase separation (PS) is developed, which is applied in Ref. [28]. In this scenario, PS is governed by two main mechanisms, namely, the reduction of the chemical free energy and the minimization of surface energy.

- (II) The Cahn-Hilliard-Navier-Stokes (CHNS) model is expanded to multiple component systems to simulate the PS coupled with hydrodynamics in many complex fluid systems. Besides the CH equation, the convection is treated by the momentum-conserved incompressible Navier-Stokes (NS) equations. Mathematically, the CH and NS equations are connected by the thermodynamic force term which can either be derived from the energy law, or with the aid of Noether's theorem in Ref. [29]. Consequently, the inhomogeneous chemical potential inside the system propels the so-called Marangoni flow which in return promotes the droplet motion and coalescence during PS.

- (III) The Cahn-Hilliard-Navier-Stokes-Gauss (CHNSG) is demonstrated to deal with the PS of the dielectric fluids inside the electric field. Starting from the energy minimization principle, the thermodynamic-consistent electrochemical potential is deduced which complements the widely accepted electrohydrodynamic model in the society of fluid mechanics [30, 31]. By these means, the effect of the electric field on the droplet-matrix interfacial tension, as well as the phase diagram, are heedfully studied which shows the magnificent impact on PS.

2.1. Model A: The multi-component Cahn-Hilliard model

2.1.1. Free energy functional

Based on the mean field theory, I consider the free energy functional of mixture for the N-component system $\mathcal{F}$ inside the domain Ω as

$$\mathcal{F} = \int_\Omega g(\boldsymbol{c}, \nabla \boldsymbol{c})\, d\Omega = \int_\Omega \left[f(\boldsymbol{c}(\boldsymbol{x}, t)) + \boldsymbol{\kappa}\, \epsilon (\nabla \boldsymbol{c})^2 \right] d\Omega, \tag{2.1}$$

where g denotes the chemical free energy density. The composition is represented by a vector $\boldsymbol{c}(\boldsymbol{x}, t) = (c_1, c_2, \cdots, c_N)$ which is spatial $\boldsymbol{x}$ and temporal t dependent. In the bracket of Eq. (2.1), the first term f describes the bulk free energy and takes the Flory-Huggins model [32] as

$$f = \frac{k_B T}{v_m}\left(\sum_{i=1}^{N}\frac{c_i \ln c_i}{N_i} + \sum_{i=1 i<j}^{N,N}\chi_{ij}\, c_i c_j + \sum_{\substack{i=1\\ i<j<k}}^{N,N,N}\chi_{ijk}\, c_i c_j c_k\right), \tag{2.2}$$

in which k_B, T and v_m stand for the Boltzmann constant, the temperature, and the simulation cell volume, respectively. N_i indicates the polymerization degree of the ith component. For monomers and non-polymers, N is set to be 1.0. The double molecular interaction between component i and j is characterized by the Flory parameter χ_{ij}, while χ_{ijk} scales the triple interaction. The composition gradient term in Eq. (2.1) reflects the interfacial tension which is parameterized by the surface tension parameter $\boldsymbol{\kappa} = (\kappa_1, \kappa_2, \cdots, \kappa_N)$, altogether with the interface width parameter ϵ. For brevity, $\epsilon = 4.0$ is set for all components in this work and guarantees the numerical stability of the simulations. In this way, the chemical potential $\boldsymbol{\mu} = (\mu_1, \mu_2, \cdots, \mu_N)$ of the system is reckoned with the functional derivative as

$$\boldsymbol{\mu} = \frac{\delta g}{\delta \boldsymbol{c}} = \frac{\partial f}{\partial \boldsymbol{c}} - 2\boldsymbol{\kappa}\epsilon\nabla^2\boldsymbol{c}, \tag{2.3}$$

in which the functional derivative obeys the principle of least action in Lagrangian mechanics

$$\frac{\delta}{\delta \boldsymbol{c}} = \frac{\partial}{\partial \boldsymbol{c}} + \sum_{k=1}^{\infty}(-1)^k\nabla^k\frac{\partial}{\partial\nabla^k\boldsymbol{c}}, \quad k \in \mathbb{Z}.$$

Hence, the thermodynamic equilibrium is decided by the state where the chemical potential for all component i reaches the constant values.

2.1.2. Evolution equation

The previous defined chemical potential Eq. (2.3) indicates that the inhomogeneous chemical potential turns out to be the propeller of the phase separation process. So the diffusion equation (the Fickian laws), is reformulated as the classic stochastic Cahn-Hilliard equation [13]

$$\begin{aligned}\frac{\partial c_i}{\partial t} &= \nabla\cdot\Big(\sum_{j=1}^{N} D_{ij}\nabla c_j + \xi_i\Big) = \nabla\cdot\left(\sum_{j=1}^{N} D_{ij}\frac{\partial c_j}{\partial \mu_j}\nabla\mu_j + \xi_i\right)\\ &= \nabla\cdot\left(\sum_{j=1}^{N}\frac{D_{ij}}{\partial_{cc}f}\nabla\mu_j + \xi_i\right)\\ &= \nabla\cdot\left(\sum_{j=1}^{N} M_{ij}\nabla\mu_j + \xi_i\right).\end{aligned} \tag{2.4}$$

Here, the mobility is assigned with the Onsager's relationship as

$$M_{ij} = D_{ij}/\partial_{cc}f = M_0 c_i(\delta_{-} c_j), \tag{2.5}$$

in which δ_K is the Dirac delta and $M_0 = \sum_{i=1}^{N} D_i c_i$ obeys the Darken's law with D_i denoting the diffusivity of pure component i. The Gaussian white composition noise $\boldsymbol{\xi}_i$ follows the fluctuation-dissipation theorem [33] as

$$\left\langle \boldsymbol{\xi}_i, \boldsymbol{\xi}_i' \right\rangle = \frac{2\mathcal{M}_{ii} k_B T}{v_m \Delta t} \nabla^2 \delta(\boldsymbol{x} - \boldsymbol{x}') \delta(t - t'), \tag{2.6}$$

where δ is the Dirac delta and Δt is the simulation timestep.

2.1.3. Volume conservation

By nature, the evolution equation Eq. (2.4) is intrinsic volume conserved. In other words, at arbitrary position and time $(\boldsymbol{x}, t)$, the constraint $\sum_{i=1}^{N} c_i = 1$ is proven as follows. From Eq. (2.4), I express the mass flux for each component as

$$\boldsymbol{j} = \begin{bmatrix} j_1 \\ j_2 \\ \vdots \\ j_N \end{bmatrix} = - \sum_{j=1}^{N} M_{ij} \nabla \mu_j = - \begin{bmatrix} M_{11} & M_{12} & \cdots & M_{1N} \\ M_{21} & M_{22} & \cdots & M_{2N} \\ \vdots & \vdots & \ddots & \vdots \\ M_{N1} & M_{N2} & \cdots & M_{NN} \end{bmatrix} \begin{bmatrix} \nabla \mu_1 \\ \nabla \mu_2 \\ \vdots \\ \nabla \mu_N \end{bmatrix}. \tag{2.7}$$

Due to the property of the Gaussian thermal noise, the summation of composition fluctuation $\boldsymbol{\xi}_i$ has a zero expectation, thus, has no contribution to the mass flux and is cancelled in Eq. (2.7). By adding the mass flux for all components, the volume conservation demands the zero flux,

$$\sum_{i=1}^{N} j_i = -\left(\nabla \mu_1 \sum_{j=1}^{N} M_{j1} + \nabla \mu_2 \sum_{j=1}^{N} M_{j2} + \cdots + \nabla \mu_N \sum_{j=1}^{N} M_{jN} \right) = 0. \tag{2.8}$$

Considering that the gradient of chemical potential $\nabla \mu_i$ can have arbitrary values, the realization of Eq. (2.8) needs the mobility matrix to be constraint as

$$\sum_{j=1}^{N} M_{ij} \equiv 0.$$

Applying the Onsager's relation Eq. (2.5), the volume conservation is recovered as

$$\sum_{j=1}^{N} M_{ij} = M_0 c_i \left(1 - \sum_{j=1}^{N} c_j \right) \equiv 0.$$

In addition, the constant mobility $M_{ij} = M_0$ gives rise to the positive $\sum_{j=1}^{N} M_{ij} = N M_0 > 0$. It implies that the constant mobility setup does not naturally conserve the volume. The equilibrium state with $\nabla \boldsymbol{\mu} \equiv \boldsymbol{0}$ is the only scenario where the constant mobility setup works.

2.1.4. Energy law

According to the second law of thermodynamics, for the system off-equilibrium, the total chemical free energy functional $\mathcal{F}$ ought to decrease with time before reaching the steady state. The phase separation process also obeys the energy minimization principle and its thermodynamic consistency is demonstrated as follows. The total chemical free energy dissipation with time is written as

$$\begin{aligned}
\frac{d\mathcal{F}}{dt} &= \int_{\Omega} \frac{dg}{dt} d\Omega = \int_{\Omega} \left[\frac{\partial f}{\partial \boldsymbol{c}} \frac{d\boldsymbol{c}}{dt} + \frac{\partial [\boldsymbol{\kappa} \epsilon (\nabla \boldsymbol{c})^2]}{\partial \nabla \boldsymbol{c}} \cdot \frac{d(\nabla \boldsymbol{c})}{dt} \right] d\Omega \\
&= \int_{\Omega} \left[\frac{\partial f}{\partial \boldsymbol{c}} \frac{d\boldsymbol{c}}{dt} + \boldsymbol{\kappa}\, \epsilon \nabla \boldsymbol{c} \cdot \frac{d(\nabla \boldsymbol{c})}{dt} \right] d\Omega \\
&= \int_{\Omega} \left[\frac{\partial f}{\partial \boldsymbol{c}} \frac{d\boldsymbol{c}}{dt} + \boldsymbol{\kappa}\, \epsilon \nabla \boldsymbol{c} \cdot \nabla (\partial_t \boldsymbol{c}) + \kappa\, \epsilon \nabla \boldsymbol{c} \cdot \boldsymbol{u} \cdot \nabla \nabla \boldsymbol{c} \right] d\Omega. \qquad (2.9)
\end{aligned}$$

During a diffusion-dominated phase separation process, convection can be ignored which results in the zero fluid flow with $\boldsymbol{u} \equiv 0$. With the following simple calculus of derivatives,

$$\frac{d\nabla \boldsymbol{c}}{dt} = \frac{\partial \nabla \boldsymbol{c}}{\partial t} + \boldsymbol{u} \cdot \nabla \nabla \boldsymbol{c}, \qquad \frac{\partial \nabla \boldsymbol{c}}{\partial t} = \nabla \frac{\partial \boldsymbol{c}}{\partial t}, \qquad (2.10)$$

as well as the application of integral by parts, I substitute the composition evolution equation Eq. (2.4) into Eq. (2.9) and arrive at

$$\begin{aligned}
\frac{d\mathcal{F}}{dt} &= \int_{\Omega} \left(\frac{\partial f}{\partial \boldsymbol{c}} - 2\, \boldsymbol{\kappa}\, \epsilon \nabla^2 \boldsymbol{c} \right) \frac{d\boldsymbol{c}}{dt} d\Omega = \int_{\Omega} \sum_{i=1}^{N} \mu_i \nabla \cdot \left(\sum_{j=1}^{N} M_{ij} \nabla \mu_j \right) d\Omega \\
&= -\int_{\Omega^*} \sum_{i=1}^{N} \mathbf{M}_{ii} (\nabla^* \mu_i)^2 d\, \Omega^* \leq 0. \qquad (2.11)
\end{aligned}$$

Because the mobility M_{ij} defined by Onsager's relation is positive semi-definite, I transform the gradient operator $\nabla^* := \mathbf{L} \nabla$ into the Ω^* space. The transformation matrix $\mathbf{L}$ is calculated with the Cholesky decomposition as $M = \mathbf{L}^T \mathbf{M}\, \mathbf{L}$. Finally, the total chemical free energy during the phase separation process decreases with time. The energy minimum state with zero energy dissipation is nothing but the thermodynamic equilibrium for all components with $\nabla \mu_i = 0$ (or $\nabla^* \mu_i = 0$).

2.1.5. Interfacial tension

To recover the interfacial tension, I consider the equilibrium state of the α/β binary phase system. The solution of the Cahn-Hilliard equation results in the homogeneous chemical potential in the whole system as

$$\frac{\partial f}{\partial \boldsymbol{c}} - 2\, \boldsymbol{\kappa}\, \epsilon \nabla^2 \boldsymbol{c} = \boldsymbol{\mu}^e \qquad (2.12)$$

$$\boldsymbol{\mu}^e_{\alpha} = \boldsymbol{\mu}^e_{\beta} = \boldsymbol{\mu}^e. \qquad (2.13)$$

Multiplying both sides of Eq. (2.12) by $\partial \boldsymbol{c}/\partial r$ and integrating, I have

$$\int_0^x \left(\frac{\partial f}{\partial \boldsymbol{c}} - 2\,\boldsymbol{\kappa}\,\epsilon \nabla^2 \boldsymbol{c}\right)\frac{\partial \boldsymbol{c}}{\partial r}\,dr = \int_0^x \boldsymbol{\mu}^e \frac{\partial \boldsymbol{c}}{\partial r}\,dr$$

$$\boldsymbol{\kappa}\,\epsilon \left(\frac{\partial \boldsymbol{c}}{\partial r}\right)^2\Bigg|_0^x = (f - \boldsymbol{\mu}^e \boldsymbol{c})\Big|_0^x.$$

In this way, the interfacial tension γ between phase α and β is calculated by the path integral starting from the location $r = 0$ for the bulk α, to $r = \infty$ for the bulk β, which yields

$$\gamma = \int_0^\infty f - \boldsymbol{\mu}^e \boldsymbol{c} + \boldsymbol{\kappa}\,\epsilon \left(\frac{\partial \boldsymbol{c}}{\partial r}\right)^2 dr = \int_0^\infty 2\,\boldsymbol{\kappa}\,\epsilon \left(\frac{\partial \boldsymbol{c}}{\partial r}\right)^2 dr \tag{2.14}$$

in which $\boldsymbol{c}^e_\alpha$ and $\boldsymbol{c}^e_\beta$ stand for the equilibrium composition for phase α and β, respectively.

2.2. Model B: The multi-component Cahn-Hilliard-Navier-Stokes model

2.2.1. Free energy functional

To couple the convection into the phase separation process, I define the total energy function as $\mathcal{L}$ which is contributed by the free energy functional of mixture $\mathcal{F}$, and the kinetic energy $\mathcal{K}$

$$\mathcal{L} = \mathcal{F} + \mathcal{K},$$

in which

$$\mathcal{K} = \int_\Omega \frac{1}{2}\rho\,\boldsymbol{u}^2\,d\,\Omega. \tag{2.15}$$

Here, ρ stands for the fluid density and $\boldsymbol{u}$ is the flow velocity.

2.2.2. Evolution equation

Now considering the phase separation coupled with hydrodynamics, the advection term is added into the standard Cahn-Hilliard equation Eq. (2.4)

$$\frac{\partial c_i}{\partial t} + \nabla \cdot (\boldsymbol{u}\,c_i) = \nabla \cdot \left(\sum_{j=1}^N M_{ij} \nabla \mu_j + \xi_i\right), \tag{2.16}$$

which indicates that the mass transport of the liquid phases is not only facilitated by the diffusion, but also achieved by convection. Thus, the mass flux is formulated as

$$j_i = \boldsymbol{u}\,c_i - \sum_{j=1}^N M_{ij} \nabla \mu_j - \xi_i. \tag{2.17}$$

Meanwhile, the inhomogeneous composition leads to so-called Marangoni flow by adding the thermodynamic force $\boldsymbol{f}_s$ into the momentum conservation Navier-Stokes equation as

$$\begin{gathered} \nabla \cdot \boldsymbol{u} = 0, \\ \rho \left(\frac{\partial \boldsymbol{u}}{\partial t} + \boldsymbol{u} \cdot \nabla \boldsymbol{u} \right) = -\nabla p + \boldsymbol{f}_s + \nabla \cdot \left[\eta \left(\nabla \boldsymbol{u} + \nabla \boldsymbol{u}^T \right) \right] + \boldsymbol{f}_i. \end{gathered} \tag{2.18}$$

Here, p is the pressure solved by the incompressible condition $\nabla \cdot \boldsymbol{u} = 0$. The density ρ and viscosity η are interpolated as $\rho = \sum_{i=1}^{N} \rho_i c_i$ and $\eta = \sum_{i=1}^{N} \eta_i c_i$, with ρ_i and η_i taking the values of the pure component i, respectively. Conform with FDT, the random body force term $\boldsymbol{f}_i$ are Gaussian and spatial/temporal relevant with

$$\left\langle \boldsymbol{f}_i, \boldsymbol{f}_i' \right\rangle = \frac{2\,\eta\, k_B T}{v_m \Delta t} \nabla^2 \delta(\boldsymbol{x} - \boldsymbol{x}') \delta(t - t'), \tag{2.19}$$

In this chapter, I present the following expression for the inhomogeneous composition-induced thermodynamic force

$$\boldsymbol{f}_s = -\boldsymbol{c}\, \nabla \boldsymbol{\mu}. \tag{2.20}$$

which has two alternative expressions in some literature. The first formulation [34] says

$$\boldsymbol{f}_s = \nabla \cdot \left[\gamma \left(\mathbf{I} - \boldsymbol{n} \otimes \boldsymbol{n} \right) \delta_D \right], \tag{2.21}$$

where γ is the interfacial tension and $\mathbf{I}$ is the identity matrix. δ_D denotes the Dirac delta function to localize the force explicitly on the droplet-matrix interface. The normal vector of the interface $\boldsymbol{n}$ is computed as

$$\boldsymbol{n} = \frac{\nabla c_i}{|\nabla c_i|}. \tag{2.22}$$

which may become a harm to the calculation accuracy, if not carefully treated. Another difficulty of Eq. (2.21) is that this treatment cannot deal with the changing interfacial tension γ, which prevails in the diffusion-dominated process, as well as phase separation. This formulation is widely applied in the level-set and volume-of-fluid (VOF) methods, and more details can be found in Ref. [35, 36, 37, 38, 39].

The second approach is deduced by Noether's theorem in a quite decent way and reads

$$\boldsymbol{f}_s = \nabla \cdot \left[\left(g - \boldsymbol{\mu} \boldsymbol{c} \right) \mathbf{I} - 2\, \boldsymbol{\kappa}\, \epsilon \nabla \boldsymbol{c} \otimes \nabla \boldsymbol{c} \right]. \tag{2.23}$$

Differing from Eq. (2.21), the interfacial tension γ is replaced by the excessive energy term $g - \boldsymbol{\mu c}$. In this way, the alternating interfacial tension during the phase separation process can be correctly recovered. But compared with Eq. (2.20), this treatment is more difficult to implement, due to the mathematical complexity of doing the matrix calculus.

In addition, one may find a similar expression with Eq. (2.20) in some publications [40],

$$\boldsymbol{f}_s = \boldsymbol{\mu} \nabla \boldsymbol{c}. \tag{2.24}$$

Apparently, this expression turns out to be the Legendre transformation of $-\boldsymbol{c}\nabla\boldsymbol{\mu}$ and could be correct if and only if the equilibrium chemical potential is zero for all components. Widely applied in the hydrodynamic models to study fluid flow dominated phenomena, such as the flow inside the pipe with larger Reynold number, droplet wetting and dewetting, Eq. (2.24) may not lead to any noticeable flaw. Because the diffusion is so subtle in those scenarios that the composition can hardly be off-equilibrium. Therefore, to recover the unchanged surface tension, the free energy density f is simply assigned with a quartic polynomial of composition c to mimic the energy barrier between different phases which have the same f value at equilibrium. In this way, the equilibrium chemical potential is zero and the expression of Eq. (2.24) does not lost its validity. But for those scenarios with pronounced phase transformations, such as evaporation, condensation, or the phase separating polymeric solution, Eq. (2.24) may lead to errors. This incorrectness is emerged from the misunderstanding of the underlying mechanism for the Marangoni flow. Instead of the composition gradient ∇c, the chemical potential gradient $\nabla \mu$ should be the only dominate contributor to the fluid flow. In next part, I will present the deduction of thermodynamic force $\boldsymbol{f}_s$ Eq. (2.20) in Navier-Stokes equation with the energy law.

2.2.3. Energy law

Since both diffusion and convection are intertwined in the CHNS model, the total energy $\mathcal{L}$ is composed of two parts, namely, the chemical free energy $\mathcal{F}$ and the kinetic energy $\mathcal{K}$. Therefore, the total energy dissipation is interpreted as

$$\frac{d\mathcal{L}}{dt} = \frac{d\mathcal{F}}{dt} + \frac{d\mathcal{K}}{dt}. \tag{2.25}$$

- (i) The dissipation of $\mathcal{F}$ follows Eq. (2.9) as

  $$\begin{aligned}\frac{d\mathcal{F}}{dt} &= \int_\Omega \left[\frac{\partial f}{\partial \boldsymbol{c}}\frac{d\boldsymbol{c}}{dt} + 2\,\boldsymbol{\kappa}\,\epsilon\nabla\boldsymbol{c}\cdot\nabla(\partial_t\boldsymbol{c}) + 2\,\boldsymbol{\kappa}\,\epsilon\nabla\boldsymbol{c}\cdot\boldsymbol{u}\cdot\nabla\nabla\boldsymbol{c}\right]d\Omega \\ &= \int_\Omega \left[\boldsymbol{\mu}\,\frac{d\boldsymbol{c}}{dt} + 2\,\boldsymbol{\kappa}\,\epsilon\nabla^2\boldsymbol{c}\,\left(\boldsymbol{u}\cdot\nabla\boldsymbol{c}\right) + 2\,\boldsymbol{\kappa}\,\epsilon\nabla\boldsymbol{c}\cdot\boldsymbol{u}\cdot\nabla\nabla\boldsymbol{c}\right]d\Omega.\end{aligned}$$

  By using a well-known equality of vector calculus, $\nabla\cdot(\mathbf{a}\otimes\mathbf{b}) = (\nabla\cdot\mathbf{a})\mathbf{b} + \mathbf{a}\cdot\nabla\mathbf{b}$, the above equation is further simplified as

  $$\frac{d\mathcal{F}}{dt} = \int_\Omega \left[\boldsymbol{\mu}\,\frac{d\boldsymbol{c}}{dt} + \nabla\cdot\left(2\,\boldsymbol{\kappa}\,\epsilon\nabla\boldsymbol{c}\otimes\nabla\boldsymbol{c}\right)\cdot\boldsymbol{u}\right]d\Omega \tag{2.26}$$

- (ii) The kinetic energy $\mathcal{K}$ decays with time as

  $$\frac{d\mathcal{K}}{dt} = \int_\Omega \frac{1}{2}\frac{d\left(\rho\boldsymbol{u}^2\right)}{dt}\,d\Omega = \int_\Omega \rho\,\frac{d\boldsymbol{u}}{dt}\cdot\boldsymbol{u}\,d\Omega.$$

  Substituting the Navier-Stokes equations Eq. (2.18) into above formulation,

  $$\begin{aligned}\frac{d\mathcal{K}}{dt} &= \int_\Omega \left\{-\nabla p + \boldsymbol{f}_s + \nabla\cdot\left[\eta\left(\nabla\boldsymbol{u} + \nabla\boldsymbol{u}^T\right)\right]\right\}\cdot\boldsymbol{u}\,d\Omega \\ &= \int_\Omega \nabla\cdot\left[-P\,\mathbf{I} - (g - \boldsymbol{\mu}\boldsymbol{c})\,\mathbf{I} - \nabla\cdot\underline{\underline{\Theta}} + \eta\left(\nabla\boldsymbol{u} + \nabla\boldsymbol{u}^T\right)\right]\cdot\boldsymbol{u}\,d\Omega.\end{aligned}$$

Here, the thermodynamic force $\boldsymbol{f}_s$ is defined as $-\nabla\cdot\underline{\underline{\Theta}}$ and $\underline{\underline{\Theta}}$ is named as the surface stress tensor. Moreover, in contrast to the thermodynamic potential, the Landau potential P is defined as,

$$P = p - \big(g - \boldsymbol{\mu}\boldsymbol{c}\big). \tag{2.27}$$

Considering the no-slip boundary condition and the incompressible condition $\nabla\cdot\boldsymbol{u} = 0$, it is noteworthy that

$$\int_\Omega -\nabla\cdot(P\,\mathbf{I})\cdot\boldsymbol{u}\,d\Omega = 0.$$

Now, I arrive at

$$\frac{d\mathcal{K}}{dt} = \int_\Omega \nabla\cdot\Big[-(g-\boldsymbol{\mu}\boldsymbol{c})\,\mathbf{I} - \underline{\underline{\Theta}} + \eta\big(\nabla\boldsymbol{u}+\nabla\boldsymbol{u}^T\big)\Big]\cdot\boldsymbol{u}\,d\Omega. \tag{2.28}$$

- (iii) Combining Eq. (2.26) and Eq. (2.28), $\mathcal{L}$ has to decrease with time until the equilibrium is established, so that

$$\frac{d\mathcal{L}}{dt}=\int_\Omega \boldsymbol{\mu}\,\frac{d\boldsymbol{c}}{dt}+\nabla\cdot\Big[2\,\boldsymbol{\kappa}\,\epsilon\nabla\boldsymbol{c}\otimes\nabla\boldsymbol{c}-(g-\boldsymbol{\mu}\boldsymbol{c})\,\mathbf{I}-\underline{\underline{\Theta}}+\eta\big(\nabla\boldsymbol{u}+\nabla\boldsymbol{u}^T\big)\Big]\cdot\boldsymbol{u}\,d\Omega \le 0,$$

requiring the following formulation for the surface stress tensor to be held for any velocity field $\boldsymbol{u}$, in any position $\boldsymbol{x}$, and at any time t,

$$\underline{\underline{\Theta}} = -\big(g-\boldsymbol{\mu}\boldsymbol{c}\big)\,\mathbf{I} + 2\,\boldsymbol{\kappa}\,\epsilon\nabla\boldsymbol{c}\otimes\nabla\boldsymbol{c}. \tag{2.29}$$

Hence, the thermodynamic force is expressed identically to Eq. (2.23) and after simplification,

$$\boldsymbol{f}_s = -\boldsymbol{c}\nabla\boldsymbol{\mu}. \tag{2.30}$$

- (iv) Taking the CH equation Eq. (2.16), the total energy dissipation reads

$$\frac{d\mathcal{L}}{dt} = -\int_\Omega \Big[\eta\nabla\boldsymbol{u}:\nabla\boldsymbol{u}\Big]d\Omega - \int_{\Omega^*}\sum_{i=1}^{N}\mathbf{M}_{ii}\big(\nabla^*\mu_i\big)^2 d\,\Omega^* \le 0.$$

The notations inside the last integral are referred to in the paragraph below Eq. (2.11).

2.2.4. Young-Laplace pressure

In this part, I present the deduction of the Young-Laplace pressure which can be recovered by solving the CHNS equations. Considering a droplet with radius R inside the domain Ω, the chemical potential in the entire domain reaches the equilibrium $\boldsymbol{\mu}^e$ which is expressed in d-dimensional polar coordinate ($d = 2,\ 3$)

$$\boldsymbol{\mu}^e = \frac{\delta g}{\delta\boldsymbol{c}} = \frac{\partial f}{\partial\boldsymbol{c}} - 2\,\boldsymbol{\kappa}\,\epsilon\Big(\frac{\partial^2\boldsymbol{c}}{\partial r^2} + \frac{d-1}{r}\frac{\partial\boldsymbol{c}}{\partial r}\Big).$$

Multiplying by $\partial \boldsymbol{c}/\partial r$ and integrating from 0 (droplet center) to ∞ yields

$$\begin{aligned}\int_0^\infty \boldsymbol{\mu}^e \frac{\partial \boldsymbol{c}}{\partial r}\, dr &= g\Big|_0^\infty - \int_0^\infty (d-1)\frac{2\,\boldsymbol{\kappa}\,\epsilon}{r}\Big(\frac{\partial \boldsymbol{c}}{\partial r}\Big)^2 dr \\ &= (\boldsymbol{\mu}^e \boldsymbol{c})\Big|_0^\infty .\end{aligned} \tag{2.31}$$

At equilibrium, with the formulation of Landau pressure P in Eq. (2.27), the curvature effect on the pressure ΔP with the first-order approximation is replicated

$$\begin{aligned}\Delta P = P(0) - P(\infty) = (g - \boldsymbol{\mu}^e \boldsymbol{c})\Big|_0^\infty &= \int_0^\infty (d-1)\frac{2\,\boldsymbol{\kappa}\,\epsilon}{r}\Big(\frac{\partial \boldsymbol{c}}{\partial r}\Big)^2 dr \\ = \frac{(d-1)\,\gamma}{R} + \mathcal{O}\Big(\frac{1}{R^2}\Big),\end{aligned}$$

in which the Young-Laplace pressure is recovered and the surface tension γ is identical to Eq. (2.14) as

$$\gamma = \int_0^\infty 2\,\boldsymbol{\kappa}\,\epsilon\Big(\frac{\partial \boldsymbol{c}}{\partial r}\Big)^2 dr.$$

2.3. Model C: The multi-component Cahn-Hilliard-Navier-Stokes-Gaussian model

2.3.1. Free energy functional

To couple the electrical field into the phase separation process, the first step is to reevaluate the total energy of system $\mathcal{L}$. Besides, the chemical free energy $\mathcal{F}$ and the kinetic energy $\mathcal{K}$, the electric potential energy $\mathcal{U}$ also contribute to $\mathcal{L}$ by taking the following formulation

$$\mathcal{L} = \mathcal{F} + \mathcal{K} + \mathcal{U},$$

in which

$$\mathcal{U} = \int_\Omega u(\rho_e, \nabla\Psi)\, d\,\Omega = \int_\Omega \Big[-\frac{\varepsilon}{2}\,(\nabla\Psi)^2 + \rho^e\,\Psi\Big] d\,\Omega. \tag{2.32}$$

The electrical potential energy density u is composed of two aspects. One stems from the energy density of the electric field related to the material permittivity $\varepsilon(\boldsymbol{c}) = \sum_{i=1}^N \varepsilon_i c_i$ with ε_i representing the permittivity of component i. The other term $\rho^e\,\Psi$ denotes the energy needed for putting the charge density ρ^e onto the electric potential Ψ. In perfect dielectric systems, there exists no charge, and the $\rho^e\,\Psi$ term can be canceled. By applying the Gauss' law $\nabla\cdot(\varepsilon\nabla\Psi) = -\rho_e$ and the divergence theorem, as well as the no-flux boundary condition $\nabla\Psi\cdot\boldsymbol{n} = 0$ on the domain boundary S, the electrostatic energy functional can also be rewritten as

$$\begin{aligned}\mathcal{U} &= \int_\Omega \Big[-\frac{\varepsilon}{2}\,(\nabla\Psi)^2 - \nabla\cdot(\varepsilon\,\Psi\nabla\Psi) + \varepsilon\,(\nabla\Psi)^2\Big] d\,\Omega \\ &= \int_\Omega \frac{\varepsilon}{2}\,(\nabla\Psi)^2 d\,\Omega - \int_S \varepsilon\,\Psi\nabla\Psi\cdot\boldsymbol{n}\,d\,S \\ &= \int_\Omega \frac{\varepsilon}{2}\,(\nabla\Psi)^2 d\,\Omega.\end{aligned}$$

Moreover, since the electrical potential energy density u is a function of the material permittivity $\varepsilon(\boldsymbol{c})$, the chemical potential $\boldsymbol{\mu}$ becomes electric field dependent and therefore, is renamed as the electrochemical potential in the Cahn-Hilliard-Navier-Stokes-Gauss model (CHNSG).

2.3.2. Electrochemical potential

With the above total energy functional, I define the electrochemical potential $\boldsymbol{\mu}$ as the functional derivative of the potential energy $\mathcal{F}+\mathcal{U}$ with respect to the composition $\boldsymbol{c}$. So the electrochemical potential contains two parts, namely, the contributions from the chemical free energy density $\delta g/\delta\boldsymbol{c}$ and the electric potential energy density $\delta u/\delta\boldsymbol{c}$

$$\boldsymbol{\mu} = \frac{\delta g}{\delta\boldsymbol{c}} + \frac{\delta u}{\delta\boldsymbol{c}} = \frac{\partial f}{\partial\boldsymbol{c}} - 2\,\boldsymbol{\kappa}\,\epsilon\,\nabla^2\boldsymbol{c} - \frac{1}{2}\frac{\partial\varepsilon}{\partial\boldsymbol{c}}\big(\nabla\Psi\big)^2. \tag{2.33}$$

2.3.3. Evolution equation

Based on the CHNS model, I present the CHNSG model for two typical dielectric systems, namely, the leaky dielectric and the perfect dielectric.

- (i) For the leaky dielectric system where charges are induced by the external field, I replace the chemical potential with the newly defined electrochemical potential into Eq. (2.16) and obtain the corresponding CH equation,

$$\frac{\partial c_i}{\partial t} + \nabla\cdot(\boldsymbol{u}\,c_i) = \nabla\cdot\left\{\sum_{j=1}^{N}\mathcal{M}_{ij}\nabla\Big[\frac{\partial f}{\partial c_i} - 2\,\kappa_i\,\epsilon\,\nabla^2 c_i - \frac{1}{2}\frac{\partial\varepsilon}{\partial c_i}\big(\nabla\Psi\big)^2\Big] + \xi_i\right\}. \tag{2.34}$$

  Moreover, with Ohm's law, the conservation equation of charges ρ^e reads

$$\frac{\partial\rho^e}{\partial t} + \nabla\cdot\big(\boldsymbol{u}\,\rho^e\big) = \nabla\cdot(\sigma\nabla\Psi), \tag{2.35}$$

  in which the material conductivity is interpolated by $\sigma(\boldsymbol{c}) = \sum_{i=1}^{N}\sigma_i c_i$ with σ_i indicating the conductivity of component i. The induced charge also interacts with the external field Ψ which is described by Gauss' law

$$\nabla\cdot(\varepsilon\nabla\Psi) = -\rho^e. \tag{2.36}$$

Furthermore, both the composition field and the electric field are influenced by the fluid flow. In return, the unbalanced concentration and charge fields can modify the flow field by adding the corresponding force into Navier-Stokes equations

$$\nabla \cdot \boldsymbol{u} = 0, \tag{2.37}$$

$$\rho \frac{d\boldsymbol{u}}{dt} = -\nabla p - \boldsymbol{c}\nabla\boldsymbol{\mu} - \rho^e \nabla\Psi + \nabla \cdot \Big[\eta \left(\nabla\boldsymbol{u} + \nabla\boldsymbol{u}^T\right)\Big] + \boldsymbol{f}_i. \tag{2.38}$$

- (ii) For the perfect dielectric system where the external field induces no charge, the above-listed CHNSG model is simplified to

$$\begin{aligned} \nabla \cdot \boldsymbol{u} &= 0, \\ \nabla \cdot (\varepsilon \nabla\Psi) &= 0, \\ \frac{\partial c_i}{\partial t} + \nabla \cdot (\boldsymbol{u}\, c_i) &= \nabla \cdot \Big(\sum_{j=1}^{N} \mathcal{M}_{ij} \nabla\mu_j + \xi_i\Big), \\ \rho \frac{d\boldsymbol{u}}{dt} &= -\nabla p - \boldsymbol{c}\nabla\boldsymbol{\mu} + \nabla \cdot \Big[\eta \left(\nabla\boldsymbol{u} + \nabla\boldsymbol{u}^T\right)\Big] + \boldsymbol{f}_i. \end{aligned} \tag{2.39}$$

Most importantly, taking out the term $-\boldsymbol{c}\nabla\boldsymbol{\mu} = -\boldsymbol{c}\nabla(\delta g/\delta\boldsymbol{c}) - \boldsymbol{c}\nabla(\delta u/\delta\boldsymbol{c})$ from Navier-Stokes equation, I expand the electric field related $-\boldsymbol{c}\nabla(\delta u/\delta\boldsymbol{c})$ as

$$-\boldsymbol{c}\nabla\Big(\frac{\delta u}{\delta\boldsymbol{c}}\Big) = -\boldsymbol{c}\nabla\Big[-\frac{1}{2}\frac{\partial\varepsilon}{\partial\boldsymbol{c}}\big(\nabla\Psi\big)^2\Big] = \nabla\Big[\frac{\boldsymbol{c}}{2}\frac{\partial\varepsilon}{\partial\boldsymbol{c}}\big(\nabla\Psi\big)^2\Big] - \frac{1}{2}\nabla\varepsilon\big(\nabla\Psi\big)^2. \tag{2.40}$$

In previous electrohydrodynamic models [30, 41], the first term in Eq. (2.40) is expressed as a function of the fluid density ρ, rather than composition $\boldsymbol{c}$, and understood as the dielectric constraint force

$$\nabla\Big[\frac{\rho}{2}\frac{\partial\varepsilon}{\partial\rho}\big(\nabla\Psi\big)^2\Big],$$

which is often misleadingly neglected. The reason may be associated with the incompressible assumption which says the fluid density must be a constant. Insisting on this notion, one may erroneously cancel this term by thinking $\partial\varepsilon/\partial\rho = 0$. However, for the sake of thermodynamic consistency, Eq. (2.40) is the only expression that correctly describes the electro-hydro-thermodynamical interactions in the system, especially for the phase separating fluid systems where the permittivity ε changes drastically with the composition.

2.3.4. Energy law

In this part, I demonstrate the energy dissipation of the CHNSG model in which the total energy dissipation $d\mathcal{L}/dt$ is composed of three parts,

$$\frac{d\mathcal{L}}{dt} = \frac{d\mathcal{F}}{dt} + \frac{d\mathcal{K}}{dt} + \frac{d\mathcal{U}}{dt}. \tag{2.41}$$

- (i) The dissipation of chemical free energy $d\mathcal{F}/dt$ still follows Eq. (2.26) and is not shown here for brevity.
- (ii) The kinetic energy of the whole system $\mathcal{K}$ dissipates as

  $$\begin{aligned}\frac{d\mathcal{K}}{dt} &= \int_\Omega \rho \frac{d\boldsymbol{u}}{dt} \cdot \boldsymbol{u}\, d\Omega \\ &= \int_\Omega \nabla \cdot \Big[-P\mathbf{I} - \frac{\partial g}{\partial \nabla \boldsymbol{c}} \otimes \nabla \boldsymbol{c} + \frac{\partial u}{\partial \nabla \Psi} \otimes \nabla \Psi + \eta \big(\nabla \boldsymbol{u} + \nabla \boldsymbol{u}^T \big) \Big] \cdot \boldsymbol{u}\, d\Omega. \qquad (2.42)\end{aligned}$$

  Pertaining to the newly implemented electric field, the Landau potential P is redefined accordingly,

  $$P = p - g - u + \Big(\frac{\delta g}{\delta \boldsymbol{c}} + \frac{\delta u}{\delta \boldsymbol{c}} \Big) \boldsymbol{c} + \frac{\delta u}{\delta \rho^e} \rho^e = p - \big(g + u - \boldsymbol{\mu} \boldsymbol{c} - \Psi \rho^e \big). \qquad (2.43)$$

  Substituting Eq. (2.43) into Eq. (2.42), the kinetic energy dissipation follows

  $$\frac{d\mathcal{K}}{dt} = \int_\Omega \nabla \cdot \Big[- \frac{\partial g}{\partial \nabla \boldsymbol{c}} \otimes \nabla \boldsymbol{c} + \frac{\partial u}{\partial \nabla \Psi} \otimes \nabla \Psi + \eta \big(\nabla \boldsymbol{u} + \nabla \boldsymbol{u}^T \big) \Big] \cdot \boldsymbol{u}\, d\Omega. \qquad (2.44)$$

  Noteworthily, the opposite sign before the term $(\partial g/\partial \nabla \boldsymbol{c}) \otimes \nabla \boldsymbol{c}$ and $(\partial u/\partial \nabla \Psi) \otimes \nabla \Psi$ strongly indicates that the surface tension and electric field have the opposite effect on the system. Phenomenologically, the increase in Ψ can drop the surface tension which is in accordance with experiments.
- (iii) The electric potential energy dissipation is twofold.
  1. For the leaky dielectric material, it reads

     $$\begin{aligned}\frac{d\mathcal{U}}{dt} &= \int_\Omega \frac{d}{dt} \Big[\rho^e \Psi - \frac{\varepsilon}{2} (\nabla \Psi)^2 \Big] d\Omega \\ &= \int_\Omega \Big[\Psi \frac{d\rho^e}{dt} + \rho^e \frac{d\Psi}{dt} - \frac{\mathbf{E}^2}{2} \frac{\partial \varepsilon}{\partial \boldsymbol{c}} \frac{d\boldsymbol{c}}{dt} - \nabla \cdot \big(\varepsilon \mathbf{E} \big) \frac{d\Psi}{dt} - \nabla \cdot (\varepsilon \mathbf{E} \otimes \mathbf{E}) \cdot \boldsymbol{u} \Big] d\Omega \qquad (2.45) \\ &= \int_\Omega \Big[\frac{\delta u}{\delta \rho^e} \frac{d\rho^e}{dt} + \frac{\delta u}{\delta \boldsymbol{c}} \frac{d\boldsymbol{c}}{dt} - \nabla \cdot (\frac{\partial u}{\partial \nabla \Psi} \otimes \nabla \Psi) \cdot \boldsymbol{u} \Big] d\Omega. \qquad (2.46)\end{aligned}$$

     Here, the electrical field strength is defined by $\mathbf{E} = -\nabla \Psi$. Gauss' law is used to cancel the second term with the fourth term in Eq. (2.45).
  2. For the perfect dielectric material, I have

     $$\begin{aligned}\frac{d\mathcal{U}}{dt} &= \int_\Omega \frac{d}{dt} \Big[- \frac{\varepsilon}{2} (\nabla \Psi)^2 \Big] d\Omega \\ &= \int_\Omega \Big[\frac{\delta u}{\delta \boldsymbol{c}} \frac{d\boldsymbol{c}}{dt} - \nabla \cdot (\frac{\partial u}{\partial \nabla \Psi} \otimes \nabla \Psi) \cdot \boldsymbol{u} \Big] d\Omega \qquad (2.47)\end{aligned}$$

  Note that both Eq. (2.46) and Eq. (2.47) lead to a term $\sim \nabla \Psi \otimes \nabla \Psi$ if $u \sim (\nabla \Psi)^2$ is applied. This new term is consistent with the Maxwell stress tensor. As the effect of the chemical term $\nabla c_i \otimes \nabla c_i$, the stress tensor $\nabla \Psi \otimes \nabla \Psi$ is responsible for the transformation of the electrostatic energy into the kinetic energy.

- (iv) Finally, combining Eqs. (2.26) (2.44) and (2.46), the energy law for the leaky dielectric system yields,

  $$\frac{d\mathcal{L}}{dt} = -\int_{\Omega}\left[\eta\nabla\boldsymbol{u}:\nabla\boldsymbol{u}+\sigma\left(\nabla\Psi\right)^2\right]d\Omega-\int_{\Omega^*}\sum_{i=1}^{N}\mathbf{M}_{ii}\left(\nabla^*\mu_i\right)^2 d\,\Omega^* \leq 0.$$

  Meanwhile, for the perfect dielectric system with Eqs (2.26) (2.44) and (2.47),

  $$\frac{d\mathcal{L}}{dt} = -\int_{\Omega}\eta\nabla\boldsymbol{u}:\nabla\boldsymbol{u}\,d\Omega-\int_{\Omega^*}\sum_{i=1}^{N}\mathbf{M}_{ii}\left(\nabla^*\mu_i\right)^2 d\,\Omega^* \leq 0.$$

2.3.5. Young-Laplace pressure and interfacial tension

Then, I show the way to recover the Young-Laplace pressure and the interfacial tension for the CHNSG model. For a droplet with a radius R, the electrochemical potential in the entire domain reaches the equilibrium $\boldsymbol{\mu}^e$ which is expressed in d-dimensional polar coordinate ($d = 2,\ 3$) as

$$\boldsymbol{\mu}^e = \frac{\delta g}{\delta \boldsymbol{c}}+\frac{\delta u}{\delta \boldsymbol{c}} = \frac{\partial f}{\partial \boldsymbol{c}}-2\,\boldsymbol{\kappa}\,\epsilon\left(\frac{\partial^2\boldsymbol{c}}{\partial r^2}+\frac{d-1}{r}\frac{\partial\boldsymbol{c}}{\partial r}\right)-\frac{1}{2}\frac{\partial\varepsilon}{\partial\boldsymbol{c}}\left(\nabla\Psi\right)^2.$$

Multiplying by $\partial\boldsymbol{c}/\partial r$ and integrating from 0 (droplet center) to ∞, and summing the equations for different components yield

$$\int_0^\infty \boldsymbol{\mu}^e\frac{\partial\boldsymbol{c}}{\partial r}\,dr = \int_0^\infty\left[\frac{\partial f}{\partial\boldsymbol{c}}-2\,\boldsymbol{\kappa}\,\epsilon\left(\frac{\partial^2\boldsymbol{c}}{\partial r^2}+\frac{d-1}{r}\frac{\partial\boldsymbol{c}}{\partial r}\right)\right]\frac{\partial\boldsymbol{c}}{\partial r}dr-\int_0^\infty\frac{1}{2}\frac{\partial\varepsilon}{\partial r}\left(\nabla\Psi\right)^2 dr. \tag{2.48}$$

By applying the integration by parts, I rewrite the last integral in Eq. (2.48)

$$\begin{aligned}\int_0^\infty\frac{1}{2}\frac{\partial\varepsilon}{\partial r}\left(\nabla\Psi\right)^2 dr &= \frac{\varepsilon}{2}\left(\nabla\Psi\right)^2\Big|_0^\infty-\int_0^\infty\frac{\partial\varepsilon}{\partial r}\frac{\partial\Psi}{\partial r}\nabla^2\Psi dr\\ &= \frac{\varepsilon}{2}\left(\nabla\Psi\right)^2\Big|_0^\infty-\int_0^\infty\frac{d-1}{r}\frac{\partial\varepsilon}{\partial r}\left(\frac{\partial\Psi}{\partial r}\right)^2 dr.\end{aligned} \tag{2.49}$$

Substituting Eq. (2.49) into Eq. (2.48), I have

$$\begin{aligned}\int_0^\infty \boldsymbol{\mu}^e\frac{\partial\boldsymbol{c}}{\partial r}\,dr &= \left(g+u-\rho_e\Psi\right)\Big|_0^\infty-\int_0^\infty(d-1)\left[\frac{2\,\boldsymbol{\kappa}\,\epsilon}{r}\left(\frac{\partial\boldsymbol{c}}{\partial r}\right)^2-\frac{1}{r}\frac{\partial\varepsilon}{\partial r}\left(\frac{\partial\Psi}{\partial r}\right)^2\right]dr\\ &= \left(\boldsymbol{\mu}^e\boldsymbol{c}\right)\Big|_0^\infty\end{aligned}$$

At equilibrium, with the formulation of the grand pressure P in Eq. (2.43), the curvature effect on the Young-Laplace pressure ΔP with the first-order approximation is replicated as

$$\begin{aligned}\Delta P = P(0)-P(\infty) &= \left(g+u-\rho_e\Psi-\boldsymbol{\mu}^e\boldsymbol{c}\right)\Big|_0^\infty\\ &= \int_0^\infty(d-1)\left[\frac{2\,\boldsymbol{\kappa}\,\epsilon}{r}\left(\frac{\partial\boldsymbol{c}}{\partial r}\right)^2-\frac{1}{r}\frac{\partial\varepsilon}{\partial r}\left(\frac{\partial\Psi}{\partial r}\right)^2\right]dr\\ &= \frac{(d-1)\,\gamma}{R}+\mathcal{O}\left(\frac{1}{R^2}\right),\end{aligned}$$

in which R represents the droplet radius and the surface tension γ inside the electric field reads

$$\gamma = \int_0^\infty \left[2\,\boldsymbol{\kappa}\,\epsilon \left(\frac{\partial \boldsymbol{c}}{\partial r} \right)^2 - \frac{\partial \varepsilon}{\partial r} \left(\frac{\partial \Psi}{\partial r} \right)^2 \right] dr. \tag{2.50}$$

2.4. Non-dimensionalization of the models

Parameters	Description	Calculation
x^*	Length	-
γ^*	Interfacial tension	-
D^*	Diffusivity	-
E^*	Electric strength	-
η^*	Dynamic viscosity	$x^*\gamma^*/D^*$
U^*	Electric potential	E^*x^*
t^*	Time	x^{*2}/D^*
f^*	Free energy density	γ^*/x^*
P^*	Pressure	γ^*/x^*
ρ^*	Density	$x^*\gamma^*/D^{*2}$
u^*	Velocity	D^*/x^*
σ^*	Conductivity	$x^*\gamma^*/(D^*E^{*2})$
ε^*	Permittivity	$\gamma^*/(E^{*2}x^*)$
ρ^{e*}	Charge density	$\gamma^*/(E^*x^{*2})$

Table 2.1.: Scaling factors for physical parameters of the Cahn-Hilliard-Navier-Stokes-Gauss model.

All the physical parameters are non-dimensionalized by the characteristic length x^*, reference surface tension γ^*, diffusivity D^*, and electric field strength E^*. I have the following scaling factors for the physical parameters, as shown in Table 2.1. Based on the scaling factors, the non-dimensionalized evolution equations for all phase-field models are documented in Appendix. A.1.

2.5. Discretization and staggered mesh

In this section, I discuss the discretization of all phase-field models. As demonstrated in Fig. 2.1, the domain Ω is discretized into an equidistant uniform mesh with $\Delta x = \Delta y = \Delta z = 1$. The index i, j, and k represent the grid of mesh in x, y, and z direction, respectively.

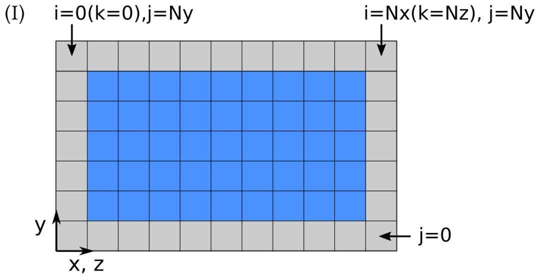

Figure 2.1.: (a) The blue area denotes the bulk region updated by Eqs. (2.34) (2.35) (2.36) (2.37) (2.38) and (2.39), and the grey cells stand for the boundary where corresponding boundary conditions are adopted. (b) The staggered mesh for the numerical discretization. Four neighboring cells with solid point: scalar variable position in the bulk, hollow point: scalar variable position on the boundary. The vectors, such as the velocity $\boldsymbol{u}$, the electric field strength $\nabla\Psi$, the diffusion flux $\nabla\mu_i$, and the noise term $\boldsymbol{\xi}_i$ in the x (or z), y dimensions are described by the triangle and the square, respectively (dark grey for the boundary, light blue for the bulk).

2.5.1. Bulk region

In the first part, I show the discretization process inside the bulk region which corresponds to the blue-colored cells in Fig. 2.1. Here, the Cahn-Hilliard-Navier-Stokes-Gauss model is demonstrated as the most complex system which contains all four variables, namely, the composition $\boldsymbol{c}$, the velocity $\boldsymbol{u}$, the electric field Ψ, and the charge density ρ^e which are iterated during the simulation. Initially, I define the following distinct difference operators applied on an arbitrary variable X at grid position (i, j, k) as

- (i) Forward difference scheme

$$\nabla_+ X = \left[\frac{X_{i+1,j,k} - X_{i,j,k}}{\Delta x}, \frac{X_{i,j+1,k} - X_{i,j,k}}{\Delta y}, \frac{X_{i,j,k+1} - X_{i,j,k}}{\Delta z}\right].$$

- (ii) Central difference scheme

$$\nabla_\circ X = \left[\frac{X_{i+1,j,k} - X_{i-1,j,k}}{2\Delta x}, \frac{X_{i,j+1,k} - X_{i,j-1,k}}{2\Delta y}, \frac{X_{i,j,k+1} - X_{i,j,k-1}}{2\Delta z}\right].$$

- (iii) Backward difference scheme

$$\nabla_- X = \left[\frac{X_{i,j,k} - X_{i-1,j,k}}{\Delta x}, \frac{X_{i,j,k} - X_{i,j-1,k}}{\Delta y}, \frac{X_{i,j,k} - X_{i,j,k-1}}{\Delta z}\right].$$

- (iv) When $\boldsymbol{A}$ is a vector, its divergence is computed with

$$\nabla_- \cdot \boldsymbol{A} = \left[\frac{\boldsymbol{A}_{i,j,k} - \boldsymbol{A}_{i-1,j,k}}{\Delta x} + \frac{\boldsymbol{A}_{i,j,k} - \boldsymbol{A}_{i,j-1,k}}{\Delta y} + \frac{\boldsymbol{A}_{i,j,k} - \boldsymbol{A}_{i,j,k-1}}{\Delta z}\right].$$

- (iv) The forward scheme calculates the mean average of X as

$$X_{1/2} = \mathbf{diag}\left\{\frac{X_{i+1,j,k} + X_{i,j,k}}{2}, \frac{X_{i,j+1,k} + X_{i,j,k}}{2}, \frac{X_{i,j,k+1} + X_{i,j,k}}{2}\right\}.$$

2.5.1.1. Concentration evolution

The time and space-dependent c_i in the grid (i, j, k) at time t is updated by the Cahn-Hilliard equation discretized as

$$\frac{c_{i,j,k}^{t+\Delta t} - c_{i,j,k}^{t}}{\Delta t} = \nabla_- \cdot (-c_{1/2}\boldsymbol{u}^t + \mathcal{M}\nabla_+\mu_{i,j,k} + \xi_c).$$

The chemical potential is discretized as

$$\mu_{i,j,k} = \left(\partial f/\partial c\right)_{i,j,k} - \kappa\,\epsilon\left(\nabla_- \cdot \nabla_+ c_{i,j,k}\right) - \left(\partial \varepsilon/\partial c\right)_{i,j,k}\left(\nabla_\circ \Psi\right)^2/2.$$

2.5.1.2. Velocity evolution

For the velocity field in 3 dimensions, the position of the velocity vector lies on the grid boundary as shown in Fig. 2.1(b). The incompressible Navier-Stokes equation is solved with Chorin's projection method [42] as:

- (i) Calculating the intermediate velocity u^* by ignoring the pressure term

$$\frac{\boldsymbol{u}^* - \boldsymbol{u}^t}{\Delta t} = -\boldsymbol{u}^t \cdot \nabla_+\boldsymbol{u}^t + \frac{\boldsymbol{f}_c + \boldsymbol{f}_e + \boldsymbol{f}_v}{\rho}.$$

For the three force terms, namely, the thermodynamic force $\boldsymbol{f}_c$, the Coulomb's force $\boldsymbol{f}_e$, and the viscous force $\boldsymbol{f}_v$, I have the following discretization

$$\begin{aligned}\boldsymbol{f}_c &= -c_{1/2}(\nabla_+\mu)^T,\\ \boldsymbol{f}_e &= -\rho^e_{1/2}(\nabla_+\Psi)^T,\\ \boldsymbol{f}_v &= \nabla_- \cdot \left[\eta_{1/2}(\nabla_+\boldsymbol{u} + \nabla_+\boldsymbol{u}^T)\right].\end{aligned}$$

- (ii) The velocity $u^{t+\Delta t}$ is calculated with

$$\boldsymbol{u}^{t+\Delta t} = \boldsymbol{u}^* - \frac{\Delta t}{\rho}\nabla_+ p_{i,j,k}^{t+\Delta t},$$

which is constraint by the incompressibility assumption with $\nabla \cdot \boldsymbol{u}^{t+\Delta t} = 0$. Therefore, the pressure term is solved by the following Poisson equation as

$$\nabla_- \cdot \left(\nabla_+ p_{i,j,k}^{t+\Delta t}\right) = \frac{\rho}{\Delta t}\nabla_- \cdot \boldsymbol{u}^*.$$

2.5.1.3. Electric field evolution

The calculation of the electric potential Ψ is achieved by the solution of the Poisson equation guided by the Gaussian law which defines two different scenarios:

- (i) The leaky dielectric system with net charges,

$$\nabla_- \cdot (\varepsilon_{1/2} \nabla_+ \Psi_{i,j,k}) = -\rho^e_{i,j,k}.$$

- (ii) The perfect dielectrics,

$$\nabla_- \cdot (\varepsilon_{1/2} \nabla_+ \Psi_{i,j,k}) = 0.$$

2.5.1.4. Charge density evolution

The charge density only exists when the system is not perfect dielectrics. Considering the fluid flow and charge migration, ρ^e should follow the continuity equation (2.35) which can be reckoned by

$$\frac{\rho^{e,t+\Delta t}_{i,j,k} - \rho^{e,t}_{i,j,k}}{\Delta t} = -\nabla_+ \rho^e \cdot \boldsymbol{u}^t + \nabla_- \cdot (\sigma \nabla_+ \Psi_{i,j,k}).$$

2.5.2. Boundary condition

In the second part, the discretization process inside the boundary S is demonstrated The boundary cell denotes the grid position whose index (i, j, k) fulfills $(i-1)(j-1)(k-1)(i-N_x)(j-N_y)(k-N_z) = 0$, as illustrated by the grey-colored cells in Fig. 2.1.

2.5.2.1. Concentration boundary condition

The composition c in the boundary S is restricted with two Boundary condition (BC) of the Cahn-Hilliard equation which is a second order partial differential equation. Due to the material conservation, the first BC is adopted for the chemical potential $\boldsymbol{\mu}$ with

$$\nabla_+ \boldsymbol{\mu}_{i,j,k} \cdot \boldsymbol{n} = 0,$$

in which n is the normal vector of the domain boundary. The second BC is twofold.

- (i) For the isolate composition BC, the Neumann BC is applied as

$$\nabla_+ \boldsymbol{c}_{i,j,k} \cdot \boldsymbol{n} = 0.$$

- (ii) Whereas, for the periodic composition BC, it yields

$$\boldsymbol{c}_{1,j,k} = \boldsymbol{c}_{N_x,j,k}, \quad \boldsymbol{c}_{i,1,k} = \boldsymbol{c}_{i,N_y,k}, \quad \boldsymbol{c}_{i,j,1} = \boldsymbol{c}_{i,j,N_z}.$$

2.5.2.2. Velocity boundary condition

If Navier-Stokes equation is solved, the following velocity BC can be used in the Pace3d.

- (i) No-slip boundary condition

$$\boldsymbol{u}_{i,j,k} = \boldsymbol{0}.$$

- (ii) Periodic boundary condition

$$\boldsymbol{u}_{1,j,k} = \boldsymbol{u}_{N_x,j,k}, \quad \boldsymbol{u}_{i,1,k} = \boldsymbol{u}_{i,N_y,k}, \quad \boldsymbol{u}_{i,j,1} = \boldsymbol{u}_{i,j,N_z}.$$

2.5.2.3. Electrical boundary condition

If electric field is coupled and solved inside the domain, the BCs for the electric field Ψ are defined as follows.

- (i) At the anode or cathode, the Dirichlet BC is adopted to assign a constant electric potential Ψ_0 on the boundary as

$$\Psi_{i,j,k} = \Psi_0.$$

- (ii) Ψ can also be constraint by the natural boundary condition with

$$\nabla_+ \Psi_{i,j,k} \cdot \boldsymbol{n} = 0.$$

- or with the periodic BC as

$$\Psi_{1,j,k} = \Psi_{N_x,j,k}, \quad \Psi_{i,1,k} = \Psi_{i,N_y,k}, \quad \Psi_{i,j,1} = \Psi_{i,j,N_z}.$$

For the leaky materials with induced charges, the BC for the charge density ρ^e reads,

$$\nabla_+ \rho^e_{i,j,k} \cdot \boldsymbol{n} = 0.$$

3. Thermal noise for triggering the phase separation [1]

Phase separations (PS) always start from the everlasting thermal noises which bring the high-energy metastable fluid mixtures into the low-energy stable phases and result in a variety of microstructural morphologies. In previous investigations [20], thermal noise terms are simply treated as a trigger for PS by adding some spatial-temporal dependent random numbers into the composition field, as well as the flow field. The mathematical model for the randomness still copies the fluctuation-dissipation theorem (FDT) which has been developed by studying the rigid body Brownian motion (BM).

3.1. System definition

In this chapter, the stochastic behavior of the standard Cahn-Hilliard model and the Cahn-Hilliard-Navier-Stokes model is revisited by studying the BM of the deformable droplet. Distinct from the rigid body scenario, the droplet BM shows a magnificent difference which is not explainable by Einstein's theory. The following sections are based on Ref. [43].

3.2. Simulation setup

The finite difference method is implemented on a staggered mesh with a size of $Nx \times Ny \times Nz$ and equidistant Cartesian spacing $\Delta x = \Delta y = \Delta z$ to solve the evolution equations, the Cahn-Hilliard equation, as illustrated in Fig. 3.1. The Navier-Stokes equations are updated with the explicit Euler scheme. The concentration c, and the fluid velocity $\boldsymbol{u}$ are subjected to the periodic boundary conditions. Parallelization of the numerical algorithm is achieved with Message Passing Interface (MPI) techniques.

3.3. Model validation

3.3.1. Brownian coefficient measurement

In previous experiments [44], the Brownian coefficient D^* is normally fitted with the mean square displacement $\langle \Delta X^2 \rangle$. To eliminate the observational error for the precise value, huge amounts of displacement data are measured for a long experimental time. However, in the simulations with the diffuse interface CH and CHNS models, fitting D^* by $\Delta \boldsymbol{X}^2$ for the long time period turns out to be inefficient. While in the simulations with the diffuse interface models, the particle centroid position at each time t, $\boldsymbol{X}(t)$, is computed by integrating all the phase-field variable ϕ or composition c over the entire domain Ω as

---

[1] Copyright notice: With the exception of the section 3.4, all other sections of this section are reused with permission from Zhang H., Wang F., Ratke L., Nestler B. Brownian motion of droplets induced by thermal noise[J]. Physical Review E, 2024, 109(2): 024208. Copyright 2024 by the American Physical Society.

$$\boldsymbol{X}(t) = \int_\Omega c(t)\, \boldsymbol{x}\, d\boldsymbol{x} \bigg/ \int_\Omega c(t)\, d\boldsymbol{x}, \quad \text{if } c(t) > 0.5.$$

Here, I postulate an alternative way to measure the Brownian coefficient D^* in which the particle velocity $\boldsymbol{v}$ is defined by the particle centroid changes for each short simulation time span Δt as

$$\boldsymbol{v} = \frac{\Delta \boldsymbol{X}}{\Delta t} = \frac{\boldsymbol{X}(t + \Delta t) - \boldsymbol{X}(t)}{\Delta t}.$$

According to statistical mechanics, the particle velocity follows the specific distributions when the thermodynamic equilibrium is reached. In the 1D case, the velocity $\mathbf{v}$ obeys the half-normal distribution as

$$f_v(\boldsymbol{v}, D^*) = \sqrt{\frac{2}{\pi}} \frac{1}{D^*} \exp\left(- \frac{\boldsymbol{v}^2}{2D^{*2}} \right), \tag{3.1}$$

while in 2D case, theoretically [45], the velocity can be described by the Rayleigh distribution as

$$f_v(\boldsymbol{v}, D^*) = \frac{|\boldsymbol{v}|}{D^{*2}} \exp\left(- \frac{\boldsymbol{v}^2}{2D^{*2}} \right), \tag{3.2}$$

and in 3D, the Maxwell distribution restricts the particle velocity as

$$f_v(\boldsymbol{v}, D^*) = \sqrt{\frac{2}{\pi}} \frac{\boldsymbol{v}^2}{D^{*3}} \exp\left(- \frac{\boldsymbol{v}^2}{2D^{*2}} \right). \tag{3.3}$$

Moreover, the displacement $\Delta \boldsymbol{X}$ of the Brownian particle in each dimension should abide by the normal distribution as

$$f_x(\Delta \boldsymbol{X}, D^*) = \frac{1}{\sqrt{2\pi D^{*2}}} \exp\left(- \frac{\Delta \boldsymbol{X}^2}{2D^{*2}} \right). \tag{3.4}$$

An advantage of this approach is that fitting the Brownian coefficient by the velocity distribution converges with only 1×10^4 velocity data. In contrast to this, with the conventional method, to get the smooth $\langle \Delta \boldsymbol{X}^2 \rangle$ mean squared displacement curve with time, it needs 20 times more data quantity than the approach based on the distribution of the velocity. Therefore, in this work, the Brownian coefficient D^* is fitted with the droplet velocity distribution via Eq. (3.1) in 1D, Eq. (3.2) in 2D, and via Eq. (3.3) in 3D. In some showcases, the displacement distribution Eq. (3.4) is also used to fit D^* and serves as the supplement for the velocity distribution.

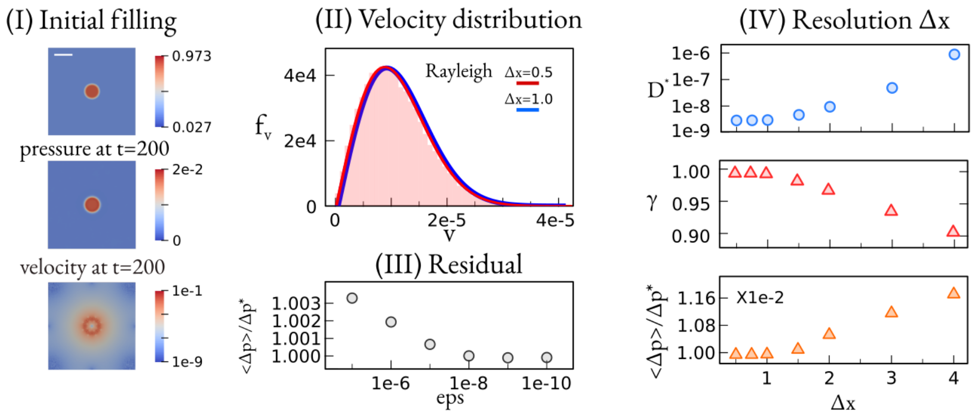

Figure 3.1.: The numerical convergence of the stochastic Cahn-Hilliard-Navier-Stokes model with composition noise $\xi_i = 0.001$ for a droplet with $r_0 = 20$. (I) The initial filling. The color bar denotes the droplet concentration c_P. (II) and (III) show the pressure distribution and the velocity field, respectively, for $\Delta x = 1.0$ at $t = 1 \times 10^4$. The color bars beneath the figure scale the corresponding values. (IV) The Brownian coefficient D^* and the interfacial tension γ with respect to Δx. (V) and (VI) The normalized Young-Laplace pressure $\langle \Delta \mathrm{p} \rangle / \Delta \mathrm{p}^*$ averaged over 1×10^4 frames with Δx and eps, respectively.

3.3.2. Numerical convergence

In the following part, the numerical convergence of the Cahn-Hilliard-Navier-Stokes model is presented. I place a droplet with an initial radius of $r_0 = 20/\Delta x$ amid the $12 r_0 \times 12 r_0$ squared matrix, as depicted in Fig. 3.1(I). The initial composition is chosen to be the bulk equilibrium value with $c_P = 0.973$ in the droplet and $c_M = 1 - c_P = 0.027$ in the matrix, respectively. For all mesh fineness Δx, the composition noise with amplitude $\xi_i = 0.001$ is applied. The densities for both droplet and matrix are set to be 0.01. The viscosity is set to be 0.001 and the random body force is neglected.

After proceeding with the simulations for different mesh resolution Δx in 2D, I measure the droplet centroid velocities for a time period of 5×10^3 and fit the Brownian coefficient D^* with the Rayleigh distribution according to Eq. (3.2). As shown in Fig. 3.1(IV), D^* converges gradually with the reduction in the resolution, and approaches to 5.18×10^{-9} as $\Delta x \leq 1.0$. The same tendency is observed for the droplet surface tension γ, which is calculated with the radial droplet concentration c profile as

$$\gamma = \int_0^{120/\Delta x} 2\,\kappa\,\epsilon \left(\frac{\partial c}{\partial r} \right)^2 dr. \tag{3.5}$$

For better statistical integrity, γ is normalized by the reference interfacial tension value at $\Delta x = 1.0$ which is averaged over the time period of 5×10^3. Moreover, the numerical accuracy of the Navier-Stokes equations is tested for different Δx and residual parameter eps and the results are demonstrated in Fig. 3.1(V) and (VI). The normalized Young-Laplace pressure possesses higher accuracy with a finer resolution and a smaller eps. Considering a compromise between the simulation accuracy and the time expense of computing, I set $\Delta x = 1.0$ and eps$= 1e - 8$ for all the CHNS simulations in the following sections.

3.3.3. Capillary wave theory

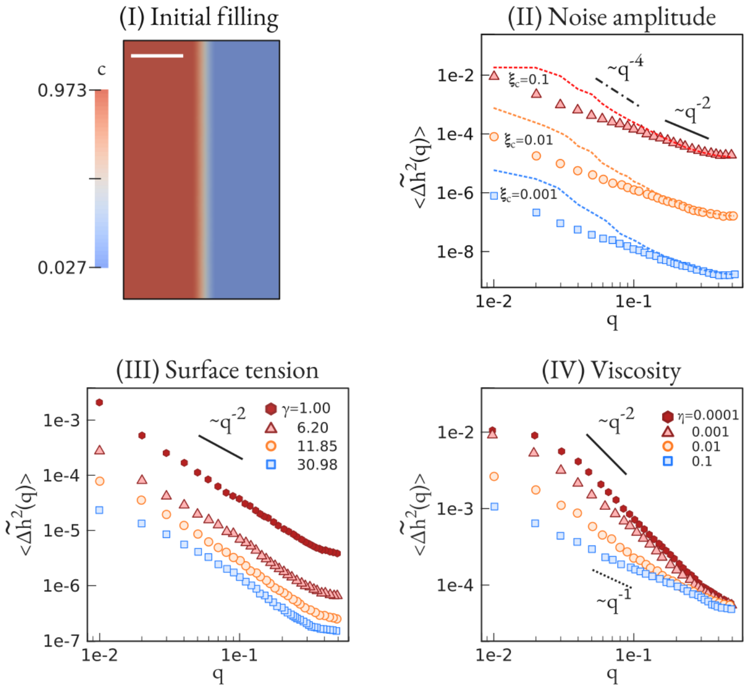

Figure 3.2.: Validation of the stochastic CHNS model with the capillary wave theory. Open colored symbols: with hydrodynamics; dashed color lines: without hydrodynamics. (a) The initial unperturbed flat interface. (b) The capillary wave amplitudes $\langle\Delta\tilde{h}^2(q)\rangle$ according to Eq. (3.7) in the reciprocal space for the perturbed interface with different composition noise amplitudes ξ_i. (c) $\langle\Delta\tilde{h}^2(q)\rangle$ versus q for different interfacial tensions, γ at noise amplitude $\xi_i = 0.05$. (d) $\langle\Delta\tilde{h}^2(q)\rangle$ versus q for different viscosities η with noise amplitude $\xi_i = 0.1$. The black solid lines guide the capillary wave theory relationship of $\langle\Delta\tilde{h}^2(q)\rangle \sim q^{-2}$. The dotted, solid, and dot-dashed lines show different scaling laws, $\langle\Delta\tilde{h}^2(q)\rangle \sim q^{-1}$, $\sim q^{-2}$, and $\sim q^{-4}$, respectively.

For liquid surfaces with small thermal noise, the capillary wave theory (CWT) is regarded as a decent way to describe its behavior which has been proven by several experiments [46, 47] and simulations [48]. Perturbed by the noise, the surface energy increase ΔE of a planar fluid interface is proportional to the surface area change as

$$\Delta E \approx \frac{\gamma}{2} \int (\nabla h)^2 \, dxdy, \tag{3.6}$$

where the interface position h is defined by the location with composition $c = 0.5$. The liquid-matrix interfacial tension is represented by γ. After Fourier transformation, Eq. (3.6) is expressed in the reciprocal space as

$$\Delta E(q) = \frac{\gamma}{2} \int q^2 \left|\Delta\tilde{h}(q)\right|^2 dq,$$

where q symbolizes the wave number, and $\widetilde{h}(q)$ represents the capillary wave amplitude in the wavenumber domain. In statistical mechanics, each wave mode of the fluctuation has the identical energy $k_B T$, so that

$$\left\langle \Delta \widetilde{h}^2(q) \right\rangle = \frac{k_B T}{4\pi^2 q^2 \gamma}, \tag{3.7}$$

where $\left\langle \Delta \widetilde{h}^2(q) \right\rangle$ is named as the structure factor of the fluid interface. According to the noise formulations stated by FDT, I have $\left\langle \Delta \widetilde{h}^2(q) \right\rangle \propto \xi_i^2$ for CHNS model.

To validate the energy dissipation behaviors of the CHNS models with the capillary wave theory (CWT), an initial setup with a flat liquid-matrix interface is demonstrated in Fig. 3.2(I)(a). The density $\rho = 0.01$, the interfacial tension $\gamma = 1.0$ are adopted. Here, the structure factor $\left\langle \Delta \widetilde{h}^2(q) \right\rangle$ is measured for two scenarios: i) with hydrodynamics (open dots) and ii) without hydrodynamics (dashed lines). The mobility $\mathcal{M}_0$ set to be 1.0 and the viscosity is $\eta = 0.001$. In good consistency with previous researches [47], at large wave number q, $\left\langle \Delta \widetilde{h}^2(q) \right\rangle$ shows the q^{-2} tendency with the wave number q for both scenarios, as guided by the black solid line in Fig. 3.2(II)(a). With the growth of the noise amplitude ξ_i by 10 times, $\left\langle \Delta \widetilde{h}^2(q) \right\rangle$ increases accordingly by 10^2 times, showing good consistence with Eq. (3.7). For the short wavelength perturbations with $q < 0.1$, the Cahn-Hilliard model without hydrodynamics (dashed colored lines) shows an apparent deviation from the CWT scaling law. It indicates that hydrodynamics is a crucial mechanism for the surface energy dissipation of the fluid interface, especially for the noise with short wavelengths. Then, in Fig. 3.2(II)(b), I fix the constant noise amplitude $\xi_i = 0.05$, and observe the reduction in capillary wave amplitudes with the increase in the surface tension γ which is in good accordance with the CWT. In Fig. 3.2(II)(c), the viscosity effect on the scaling law of $\left\langle \Delta \widetilde{h}^2(q) \right\rangle$ versus q is illustrated. By setting a larger η, the viscous stress $\eta \nabla^2 \boldsymbol{u}$ in the Navier-Stokes equation is magnified, giving rise to a stronger energy dissipation via frictional forces between fluids. But the deduction of Eq. (3.7) only considers the surface energy dissipation and does not take the viscosity effect on the kinetic energy into account. This observation in turn indicates that for the composition noise dominated Brownian motion of sub-micro droplets, the viscous effect is of subtle importance. In this way, I set low viscosity $\eta = 0.001$ in the following parts to eliminate the viscous dissipation mechanism, which is in line with the CWT and experiments.

3.3.4. Dispersion relation

To have a better understanding of the CWT for CHNS models, I scrutinize the energy dissipation by investigating the dispersion relation which explains the distinct scaling laws between the capillary wave amplitude $\langle \Delta^2 h \rangle$ with the wavenumber q by considering the interplay of diffusion and convection.

3.3.4.1. Diffusion dominated regime

For the CHNS model, the fluctuation energy-gaining rate reads

$$\frac{\partial \mathcal{F}^{+}}{\partial t} = \int_{\Omega} f^{*} \mathcal{M}\, \xi_i^2 \, d\Omega = f^{*} \mathcal{M}_0 \, \xi_i^2 \, \mathrm{S}.$$

Meanwhile, the energy dissipates as

$$\begin{aligned} \frac{\partial \mathcal{F}^{-}}{\partial t} &= \int_{\Omega} \frac{\delta F}{\delta c}\frac{dc}{dt} d\Omega = -\int_{\Omega} \mathcal{M} (\nabla \mu)^2 d\Omega \\ &= \mathrm{S} \int_{-\infty}^{\infty} \mathcal{M}\, f^{*2}\, \bar{\epsilon}^{\,2} \left(q^2 \chi^2 + 2\epsilon^2 q^4 \chi + \epsilon^4 q^6\right) \bar{c}^{\,2}\, dx \\ &= \mathcal{M}_0\, f^{*2}\, \bar{\epsilon}^{\,2}\, \mathrm{S} \left(q^2 \chi^2 + 2\epsilon^2 q^4 \chi + \epsilon^4 q^6\right) \Delta^2 h, \end{aligned}$$

in which the integrated term is expanded at the interface position with $c = 0.5 + \bar{\epsilon}\, \bar{c}$. The composition perturbation $\bar{c}$ is analogized with the wave function $e^{\zeta t - iqy}$. At equilibrium, I obtain

$$\Delta^2 h \propto \frac{\xi_i^2}{\gamma \left(\chi^2 q^2 + 2\chi\, \epsilon^2 q^4 + \epsilon^4 q^6\right)}. \tag{3.8}$$

Both q^{-2} and q^{-4} scaling laws are captured in the simulated CWT of the Cahn-Hilliard model without hydrodynamics; see dashed lines in Fig. 3.2(b). It reflects the prominent difference between the Cahn-Hilliard equation and the diffusion equation (Fick's second law), since CH is a fourth-order partial differential equation expressed with composition perturbation $\bar{c}$ as

$$\frac{d\bar{c}}{dt} = \nabla \cdot (\mathcal{M} \frac{\gamma}{\epsilon} \chi \nabla \bar{c}) - \nabla \cdot (\mathcal{M} \gamma \epsilon\, \nabla^3 \bar{c}).$$

Hence, the energy dissipation for small wavelength noises (large q) behaves similarly to the standard diffusion process. While for the large wavelength (small q), its dissipation is dominated by the fourth-order term $\sigma \nabla^4 \bar{c}$.

3.3.4.2. Convection dominated regime

The energy law behaves entirely differently when convection overwhelms diffusion, and I have another energy law for the CHNS model

$$\begin{aligned} \frac{\partial \mathcal{F}^{-}}{\partial t} &= \int_{\Omega} \boldsymbol{u} \cdot \rho \frac{d\boldsymbol{u}}{dt}\, d\Omega = \int_{\Omega} \boldsymbol{u} \cdot \left(\mu \nabla c\right) d\Omega \\ &= \mathrm{S} \int_{-\infty}^{\infty} \nabla \Psi \cdot \big(\frac{\gamma \chi}{\epsilon} \bar{c} - \gamma \epsilon\, \nabla^2 \bar{c}\big) \big(\bar{\epsilon}\, \nabla \bar{c}\big) dx \\ &= \frac{\gamma\, \mathrm{S}\, \bar{\epsilon}}{\epsilon} q' \Psi \left(\chi\, q + \pi^2 \epsilon^2 q^3\right) \Delta^2 h. \end{aligned}$$

Here, I assume the velocity $\boldsymbol{u}$ as the gradient of the tiny perturbed stream function $\Psi = e^{\zeta' t - iq' x}$ with the different phase parameter q' from the composition noise. Under this circumstance, the energy law for the convection-dominated CHNS model is deduced as

$$\Delta^2 h \propto \frac{\mathcal{M}_0\, \xi_i^2\, \epsilon}{\gamma\,(\chi\, q + \epsilon^2\, q^3)}, \tag{3.9}$$

which is also in line with the CWT simulation results shown in Fig. 3.2. These dispersion relations are dealing with the composition noise dissipated via convection, and has never been considered in previous FDT and CWT theories. I stress that this energy dissipation mechanism is entirely different from the one in the Langevin mechanics, where the random body force gets smoothed by the viscous stress. Testified in previous simulations [49, 50], the random body force perturbed interface still follows the CWT scaling law with $\langle \Delta \widetilde{h^2} \rangle \sim q^{-2}$.

3.4. Stochastic Cahn-Hilliard model

In this section, I present the stochastic Cahn-Hilliard model is investigated with the droplet Brownian motion (BM) simulations. Here, only the diffusion and composition noises are considered for sub-micro droplets for which the hydrodynamics is neglected.

3.4.1. Anomaly of the Brownian motion with dimensions

The droplet with radius $r_0 = 40$ in placed inside the domain with $N_x = 12r_0$ for 1D, $N_x \times N_y = 12r_0 \times 12r_0$ for 2D, and $N_x \times N_y \times N_z = 12r_0 \times 12r_0 \times 12r_0$ for 3D, respectively. The mobility is set to be 1.0 and the composition noise amplitude $\xi_i = 0.001$ are considered for all components. As shown in Fig. 3.3(I), the droplet trajectories in (a)-1D, (b)-2D, and (c)-3D present the stochastic motion. Notably, in the velocity distributions; see Fig. 3.3(II), all simulated droplet velocity (histograms) obeys the corresponding theoretical distributions (solid lines) Eqs. 3.1, 3.2, and (3.3), which indicates that the droplet motions reach the thermal equilibrium. In addition, the Gaussian distributed droplet displacements by each dimension in Fig. 3.3(III) also strongly prove of the conformity between simulation and statistical mechanics. However, the mean squared displacement in Fig. 3.3(IV) tell an entirely different story from the BM theories. According to Einstein's theory based on the rigid body assumption, the linear relation between MSD and time is

$$\langle \Delta \mathbf{X}^2 \rangle = n\, D^* t, \tag{3.10}$$

scaled by the dimension number n and the Brownian coefficient D^*. In other words, the rigid body BM in 3 dimension space has the largest diffusion rate which is 1.5 times in 2D, and 3 times in 1D. But for the Brownian droplet with composition fluctuations, although the linear relationship of $\langle \Delta \mathbf{X}^2 \rangle \sim t$ is observed (see the black solid line), the simulated MSD in Fig. 3.3(IV) expresses the totally reversed tendency, where the BM has the largest D^* in 1D and smallest in 3D.

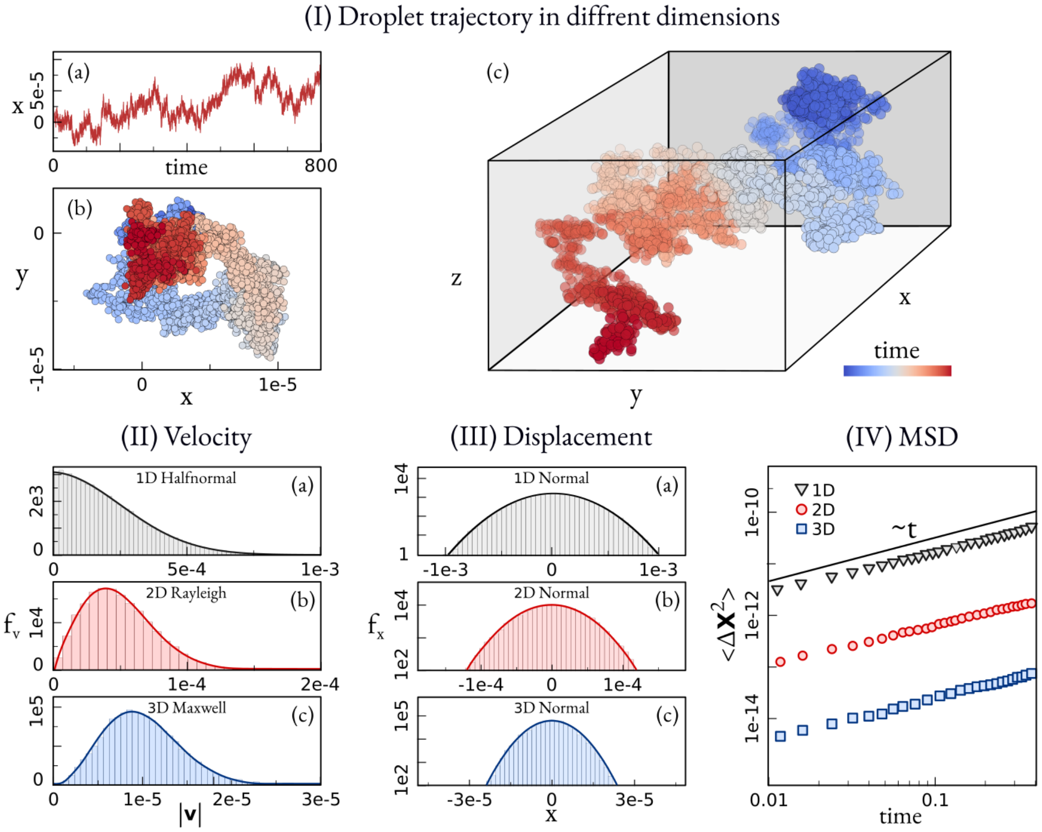

Figure 3.3.: n-dimensional Brownian motion induced by composition noises. (I) Trajectories of the droplet with radius $r_0 = 40$ in (a) 1D, (b) 2D, and (c) 3D. The color bar measures the time sequence. (II) The simulated velocity histograms in (a) 1D, (b) 2D, and (c) 3D, each fitted by half-normal (black line), Rayleigh (red line), and Maxwell (blue line) distributions, respectively. (III) The simulated displacement histograms in x direction, (a) 1D, (b) 2D, and (c) 3D, fitted by normal distributions (solid colored lines). (IV) The mean squared displacement (MSD) $\langle \Delta \mathbf{X}^2 \rangle$ decreases with the dimension n, which disobeys the Einstein-Stokes relation $\langle \Delta \mathbf{X}^2 \rangle \sim nD^* t$. The solid line guides the $\sim t$ tendency.

3.4.2. Equipartition theorem

To explain the anomaly relationship between the Brownian coefficient D^* with the dimension number n, I performed simulation for various droplet radii ranging from $r_0 = 10$ to 100 by different n. The Brownian coefficient D^* is fitted by the droplet velocity distributions and is depicted in Fig. 3.4(I). Clearly can be noticed, D^* presents absolutely distinct relations with r_0 for different dimensions. In 1D, D^* stays almost constant which is solely decided by the noise amplitude ξ_i (equivalent to the temperature T). While, in 2D cases, the Einstein inverse relation $D^* \sim r_0^{-1}$ is observed, as guided by the red dot-dashed line in Fig. 3.4(I). Most interestingly, in 3D cases, $D^* \sim r_0^{-2}$ tendency indicates the different fluctuation-dissipation mechanism from the rigid body BM.

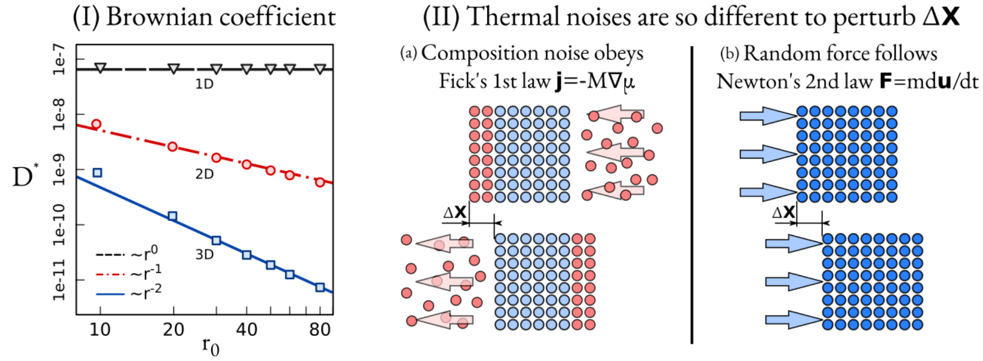

Figure 3.4.: Equipartition theorem for the composition noise. (I) Droplet Brownian coefficient D^* in different dimensions following distinct scaling laws with the radius r_0, which are guided by the colored lines. Only 2D BM follows the Einstein-Stokes relation $D^* \sim r_0^{-1}$. (II) Contrived example of two types of noise-induced droplet motions based on the lattice model. (a) Composition noise propels only the interface obeying Fick's first law; (b) Random body force displaces the whole droplet following Newton's second law.

To elucidate the anomaly size effect on the Brownian coefficient D^*, in Fig. 3.4(II), I show two schemes that would help to understand the underlying mechanisms of two types of BM, namely, (a) the droplet BM perturbed by composition noises, and (b) the rigid body BM propelled by random body forces. The composition noises ξ_i only have pronounced effect on the molecules at the interface region, due to the definition of noise amplitude ξ_i by FDT with

$$\langle \xi_i, \xi_i' \rangle \sim 2\mathcal{M}_0\, c_i(1-c_i)\, k_B T,$$

where $c_i(1-c_i)$ approaching 0 inside the bulk droplet and matrix leads to negligible composition fluctuations. Hence, to diffuse the droplet rightwards by a random distance ΔX, the thermal composition noises dissolve the droplet molecules on the left interface into the matrix with a width ΔX, while condensing the same amount on the right side, as schematically shown in Fig. 3.4(II)(a). In fact, the light blue-colored molecules inside the droplet bulk actually do not need to move at all. In this way, I can explain the reason why the Brownian coefficient D^* in the 1D case has no size effect. Because the stochastic motion obeys Fick's 1st law, the material flux at the interface has hardly any connection with the bulk region. In contrast to this in Fig. 3.4(II)(b), the random body forces $\boldsymbol{f}_i$ act on the whole particle,

$$\langle \boldsymbol{f}_i, \boldsymbol{f}_i' \rangle \sim 2\,\eta\, k_B\, T,$$

where the viscosity η is always nonzero inside the rigid body. To shift rightwards by $\Delta \boldsymbol{X}$, the particle follows Newton's second law. It implies that the random body forces are allocated on every molecule inside the droplet by the density ρ, so that all molecules moves the same distance $\Delta \boldsymbol{X}$. Therefore, the random motion in n-dimension is simply the summation of the BM in each dimension, which is the exact idea of Einstein's deduction. However, for the droplet BM, the deduction of the mean squared displacement is as follows.

$$\frac{d\boldsymbol{X}}{d\,t} = \frac{1}{\mathrm{S}} \int_S \frac{d\,h}{d\,t}\, dS = \frac{1}{\mathrm{S}} \int_S \frac{\partial h}{\partial c} \frac{d\,c}{d\,t}\, dS = \frac{1}{\mathrm{S}\,|\nabla c|} \int_S \frac{d\,c}{d\,t}\, dS = \frac{1}{\mathrm{S}\,|\nabla c|} \int_S \xi_i\, dS.$$

Here, $|\nabla c|$ denote the equilibrium composition gradient at the interface position h. The surface integral of composition noises on S can be treated with the definition of the noise amplitude by FDT,

$$\int_S \xi_i\, dS \int_S' \xi_i'\, dS' = \int_S \langle \xi_i, \xi_i' \rangle\, dS = \frac{\mathcal{M}_0\, k_B\, T\, \mathrm{S}}{2\, v_m\, \Delta t},$$

where the delta function $\delta_K(\boldsymbol{x} - \boldsymbol{x}')$ removes one space integration. Applying the temporal delta function $\delta_K(t - t')$ to cancel one timestep term dt, I obtain the Brownian coefficient,

$$D^* = \frac{\langle d\boldsymbol{X}, d\boldsymbol{X}' \rangle}{d\,t} = \frac{\mathcal{M}_0\, k_B\, T}{\alpha\, \mathrm{S}}, \text{ with the unit of } \left[\frac{\mathrm{m}^2}{\mathrm{s}}\right], \tag{3.11}$$

in which the parameter $\alpha = 2\, v_m\, (\nabla c)^2$. For the 1D droplet, $\mathrm{S} = 2$ results in $D^* \sim \mathcal{M}_0\, k_B\, T$ with no radius dependency. Similarly, the anomalous tendencies $D^* \sim r_0^{-1}$ in 2D and $D^* \sim r_0^{-2}$ in 3D are derived and show well accordance with our simulations in Fig. 3.4(I). Our analysis also indicates two differences between the chemical free energy fluctuations and the kinetic energy perturbations.

- (i) The equipartition of thermal fluctuation energy. For composition noises, the molecules at the interface are entitled to share the majority parts of the thermal energy. Actually, I can say that the thermal fluctuation energy is transformed into the surface energy changes of the system. For random body force, thermal energy is expressed by the kinetic energy perturbations which are partitioned onto all molecules by their density.

- The energy dissipation mechanism. The composition noises get dissipated by the surface energy minimization which is related to the interface area S. Therefore, the composition fluctuation shows a stronger dissipation effect at higher dimensions. Whereas, the random body force is smoothed by the Stokes drag force which is always proportional to the droplet radius r_0. Thus, the dissipation effect is simply the summation of all the n dimensions.

3.4.3. Noise reduction mechanism

In previous parts, I discussed the properties of the composition noise which differ from the random body force. Notably, the thermal energy dissipation mechanism via interface tension shows a strong dependency on the dimension number n, so the noises are reduced more severely in 3D than in 2D. In this part, I present other two dimension-related composition noise reduction mechanisms with the help of the capillary wave theory (CWT). More details about CWT are found in Sec. 3.3.3.

3.4.3.1. Non-linearity of the Cahn-Hilliard equation

The greatest progress the Cahn-Hilliard equation made is that the driving force for the diffusion process is attributed to the unbalanced chemical potential, rather than the concentration gradient. So the equilibrium interface can be established and the interfacial tension effect can be studied. By taking the infinitesimal composition fluctuation $\bar{c}$ at the interface with $c = 0.5 + \bar{\epsilon}\,\bar{c}$ and neglecting the higher order of $\bar{c}$, the CH equation yields,

$$\frac{\partial c}{\partial t} = \mathcal{M}\nabla^2\mu = \mathcal{M}\nabla^2\Big(-\frac{\gamma}{\epsilon}\,\bar{\epsilon}\,\bar{c} - 2\gamma\,\epsilon\,\bar{\epsilon}\,\nabla^2\bar{c}\Big). \tag{3.12}$$

Whereas the standard mass conservation equation follows Fick's law as

$$\frac{\partial c}{\partial t} = D\nabla^2 c. \tag{3.13}$$

Apparently, the Laplace operator ∇^2 is linear with the dimension number n, which is defined in the Cartesian coordinate system $\mathbb{R}^n$ with coordinates basic vector $\boldsymbol{x} = (x_1, x_2, ..., x_n)$ as

$$\nabla^2 := \frac{\partial^2}{\partial \boldsymbol{x}^2} = \sum_{i=1}^{n} \frac{\partial^2}{\partial x_i^2}.$$

Thus, for the standard diffusion equation Eq. (3.13) and the momentum conservation Navier-Stokes equation, the expression in each dimension is addable which reflects the fact that there is no interaction between different dimensions, so as the identical-independent-distributed noise terms. I highlight that the interfacial term in CH equation Eq. (3.12) is totally different and is defined by a fourth-order operator

$$\nabla^2(\nabla^2 c) := \frac{\partial^2}{\partial \boldsymbol{x}^2}\left(\frac{\partial^2 c}{\partial \boldsymbol{x}^2}\right) = \sum_{i=1}^{n} \frac{\partial^4 c}{\partial x_i^4} + 2\sum_{i>j=1}^{n,n} \frac{\partial^4 c}{\partial x_i^2 \partial x_j^2},$$

where the last summation term is non-linear to dimension number n. Thus, the CH equation cannot be treated as the add-up of all expressions in each dimension together, distinct from the diffusion equation and NS equation. Moreover, with the increase in dimension, the number of non-linear terms increases accordingly. Since the terms $\partial^4/(\partial x_i^2 \partial x_j^2)$ represent the interfacial effect which smooths the composition noise, the noise amplitude is smaller by larger dimension number n, even though the noise amplitude ξ_i are set equally.

In Fig. 3.5(I), the perturbed fluid interfaces at 2D (a) and 3D (b) are shown at time $t = 1000$. Weak noise reduction can be noticed in the CWT Fig. 3.5(II). At the short wavevector

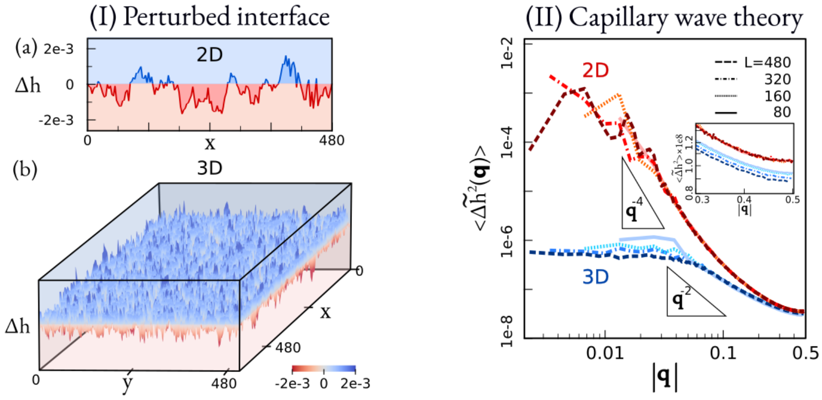

Figure 3.5.: Energy dissipation of composition noise perturbed interface. (I) Interface height changes Δh at $t = 100$. (a) 2D, and (b) 3D (the color bar scales Δh). (II) Dispersion relation with different dimensions shows stronger damping for long wave perturbations (small wavevector $\mathbf{q}$). The capillary wave amplitude $\langle \Delta\widetilde{h}^2(\mathbf{q})\rangle$ for 2D (red lines) and 3D (blue lines) cases with different interface scale L.

$|\boldsymbol{q}| = 0.5$, the capillary wave (CW) amplitude $\langle \Delta\widetilde{h}^2(\mathbf{q})\rangle$ is equivalent to the variance of the composition noise. The tiny difference between the red-circled 2D and the blue-squared 3D variances are noticeable in the inset of Fig. 3.5(II). Most importantly, I observe the second noise reduction mechanism at the long wavelength region in the CWT.

3.4.3.2. Long range constrain

In 2D scenario, the CW amplitudes follows the scaling law with $\langle \Delta\widetilde{h}^2(\mathbf{q})\rangle \sim |\boldsymbol{q}|^{-4}$ in the long-wavelength region with $|\boldsymbol{q}| < 0.1$ which indicates the equipartition of thermal fluctuation energy on the interface and in good agreement with the theory Eq. (3.8). In the 3D case, the CW amplitudes behave entirely different from the scaling law of CWT with $\langle \Delta\widetilde{h}^2(\mathbf{q})\rangle < |\boldsymbol{q}|^{-2}$ in the mid-wavevector region with $0.02 < |\boldsymbol{q}| < 0.1$. The energy dissipation at interface is much stronger in 3D than in 2D, especially, in the long wavevector region with $|\boldsymbol{q}| < 0.01$. Although identical parameters are adopted for 2D and 3D simulations in Fig. 3.5(II), the CW amplitude in 3D falls on the plateau and shows great derivation from the 2D case, indicating the noise reduction by the long-range constraint. This observation strongly resembles the Mermin–Wagner theorem pointing out that the 2D and 3D fluid systems are different. Intuitively, it means that at finite temperatures, the long-range interface fluctuations can be easily created and maintained by tiny composition fluctuations in 2D, but can be deeply damped in 3D which is highly associated with the interfacial term in the CH equation. The breakdown of the equipartition theorem in 3D should be heeded in future works.

3.5. Stochastic Cahn-Hilliard-Navier-Stokes model

3.5.1. Equilibrium

3.5.1.1. The Einstein's relation

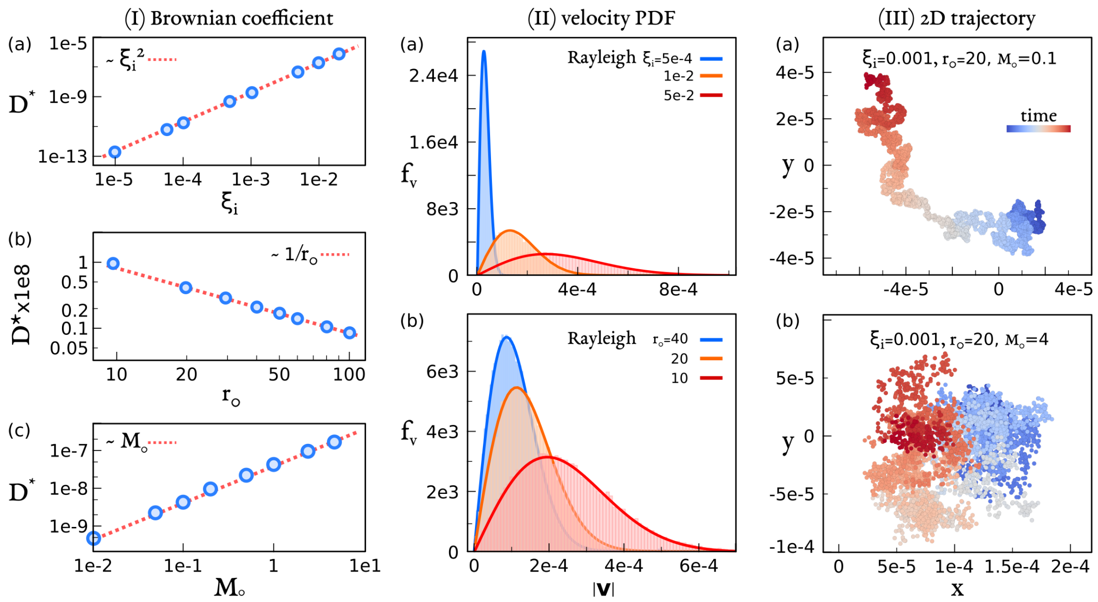

Figure 3.6.: 2D Brownian motion of droplets by CHNS model. (a) The Brownian motion coefficient D^*, upper: with noise amplitude ξ_i; mid: with initial radius r_0; lower: with kinetic parameter τ, the dashed red lines guide the $D^* \propto \xi_i^2$, $1/r_0$, and $\mathcal{M}$ relations, respectively. (b) The probability density function (PDF) of particle velocity follows the Rayleigh distribution. Upper: with ξ_i; lower: with r_0. (c) The particle trajectory. The color bar scales the time sequence.

I present a simple proof of the Einstein relation replicated with the phase-field model. The total fluctuation energy normalized by the characteristic free energy density f^* on the 2-dimensional particle with radius r_0 reads

$$\begin{aligned}\langle E\rangle / f^* &= \int_\Omega \langle \sqrt{\mathcal{M}}\,\xi_i, \sqrt{\mathcal{M}}\,\xi_i' \rangle \, d\Omega = \int_\Omega \mathcal{M}_0\, \xi_i^2\, \phi\,(1-\phi)\, d\Omega \\ &= \mathcal{M}_0\, \xi_i^2 \int_0^\infty c\,(1-c)\, 2\pi r\, dr \\ &= \mathcal{M}_0\, \xi_i^2\, \mathrm{S},\end{aligned}$$

where $\mathrm{S} = \int_0^\infty c\,(1-c)\, 2\pi\, r dr = 2\pi r_0$ represents the surface area of the perfect spherical droplet with the interface width approaching the sharp interface limit [51]. The characteristic free energy f^* equates to 1.0 after non-dimensionalization. Consequently, with the property of the Rayleigh distribution, the root mean square droplet velocity in 2D reads

$$v_{rms} = \sqrt{\langle \boldsymbol{v}^2 \rangle} = \sqrt{\frac{2\langle E \rangle}{m}} = \sqrt{\frac{4\,\mathcal{M}_0\,\xi_i^2}{r_0}} = \sqrt{2D^*},$$

from which the Brownian coefficient D^* follows

$$D^* = \frac{2\,\mathcal{M}_0\,\xi_i^2}{r_0}. \tag{3.14}$$

To testify the Einstein's relation, I perform 2D Brownian motion simulations. A droplet with an initial radius of $r_0 = 20$ is placed amid the domain with a size of $12r_0 \times 12r_0$ which can eliminate the influence of boundary on the droplet motion [45]. The surface tension parameter is set to be $\gamma = 1.0$ With an increase in the noise amplitude ξ_i, the Brownian coefficient D^* shows a parabolic relation with ξ_i, as guided by the red dashed line in Fig. 3.6(I)(a). According to FDT, the linear dependency of D^* on k_BT is confirmed. Here, D^* is fitted with the Rayleigh distribution based on the droplet velocity distributions for 10^6 time steps, as sketched in Fig. 3.6(b). For stronger noise (or higher temperatures), the probability distribution function (PDF) of velocity becomes broad and shifts to the high-velocity side, indicating enhanced droplet motion by the composition noise.

Next, I alter the droplet radius r_0 for a constant noise amplitude $\xi_i = 0.001$. The inverse relationship of $D^* \sim 1/r_0$ is clearly demonstrated in the mid row of Fig. 3.6(a), as guided by the red dashed line. By increasing the droplet radius, I observe that the peak of the velocity PDF moves to the low-velocity in Fig. 3.6(b). It implies that the Brownian droplet approaching its equilibrium is influenced by the size effect. Moreover, I observe another linear relationship between D^* and the mobility $\mathcal{M}$ which is shown in the lower row of Fig. 3.6(a). Compared to the 2D droplet trajectories in Fig. 3.6(c), the larger molecular mobility not only enhances the macroscopic diffusion of the whole Brownian droplet but also modifies the motion behavior which is discussed later in Sec. 3.5.2.1.

3.5.1.2. Fluctuation-dissipation theorem

In the standard CHNS model (Model H), two types of noises are implemented which give rise to the Brownian motion, namely composition noise ξ_i and random body force $\boldsymbol{f}_i$. Therefore, the momentum is written as

$$\int_\Omega \frac{d(\boldsymbol{u}\,c)}{dt}\,d\Omega = \int_\Omega \left(\boldsymbol{u}\frac{dc}{dt} + c\,\frac{d\boldsymbol{u}}{dt}\right) d\Omega, \tag{3.15}$$

$$\frac{dc}{dt} = \nabla \cdot (\mathcal{M}\nabla\mu + \sqrt{\mathcal{M}}\,\xi_i). \tag{3.16}$$

$$\frac{d\boldsymbol{u}}{dt} = -\nabla P - c\nabla\mu + (\eta\nabla^2\boldsymbol{u} + \sqrt{\eta}\,\boldsymbol{f}_i). \tag{3.17}$$

Here, two noises are dissipated by individual diffusion-type equations synchronously, one in the mass conservation equation Eq. (3.16), another one for the momentum conservation equation Eq. (3.17). Previous studies [52, 53] show that the random body force gives rise to the Stokes-Einstein-Sutherland relation (SES) with

$$D_H^* = \frac{k_B T}{a\pi\eta\, r_0} = k_B T \zeta,$$

where the constant a is decided by the geometry of the motion and the so-called hydrodynamic mobility $\zeta = (a\pi\eta\, r_0)^{-1}$. And Eq. (3.14), as well as the simulation results, tell the linear relationship between D^* and the thermodynamic mobility M as

$$D^* = \frac{4\mathcal{M}_0 k_B T}{r_0} = k_B T M.$$

Here, I categorize the Brownian motion into two subgroups, namely i) the composition noise dominated BM for droplets at higher temperatures and large inter-molecular diffusivity, and ii) the random body force dominated BM for the rigid body, each type has its individual Brownian coefficient as

$$D^* = \begin{cases} k_B T\,\zeta \propto \eta^{-1}, & \text{for rigid body;} \\ k_B T M \propto \mathcal{M}_0, & \text{for droplets.} \end{cases} \tag{3.18}$$

Moreover, both Eqs. (3.16) and (3.17) are diffusion-type equations, with the composition c diffused by the term $\mathcal{M}\nabla^2\mu$ and the velocity $\boldsymbol{u}$ by $\eta\nabla^2\boldsymbol{u}$, which results in the exponential decay of c and $\boldsymbol{u}$ with time toward the equilibrium state. But the results show entirely opposite scaling laws. I argue that this phenomenon can be understood as follows. For a 0.1μm droplet with the diffusivity by the order of 10^{-9}m^2/s, its characteristic time scale $t = x^{*2}/D = 10^{-5}$s is 1000 times larger than the characteristic time scale of Brownian motion and hydrodynamics $t = 10^{-8}$s. Therefore, the huge composition fluctuation can never be dissipated to equilibrium by the slow diffusion in the hydrodynamic time scale. In this way, Eq. (3.16) is underdamped, and results in the droplet Brownian coefficient $D^* \sim \mathcal{M}_0$ which is not fulfilled with the FDT. This conclusion is in line with the dispersion relation, Eq. (3.9). The fluctuation energy dissipation rate is not only proportional to $k_B T$, but also scaled by the prefactor, not coincidentally, $\mathcal{M}_0$. For the droplet with larger length scales or the rigid body, the composition noise is so weak to be smoothed by diffusion, and the stochastic droplet motion is mainly attributed to the random body force $\mathbf{F}$ which recovers the SES relation.

3.5.2. Non-equilibrium

3.5.2.1. Marangoni effect

In the deduction of the Brownian coefficient by Einstein, the particle is assumed to be a perfectly rigid body, and the energy is dissipated via the viscous stress by the surrounding matrix. In this derivation, the surface tension of the particle is overlooked, because its characteristic time scale is several orders shorter than the BM. Highly contrasted to this, for the Brownian droplet with finite surface tension, the time scale of the surface tension becomes comparable with BM. The composition noise engenders the interfacial tension

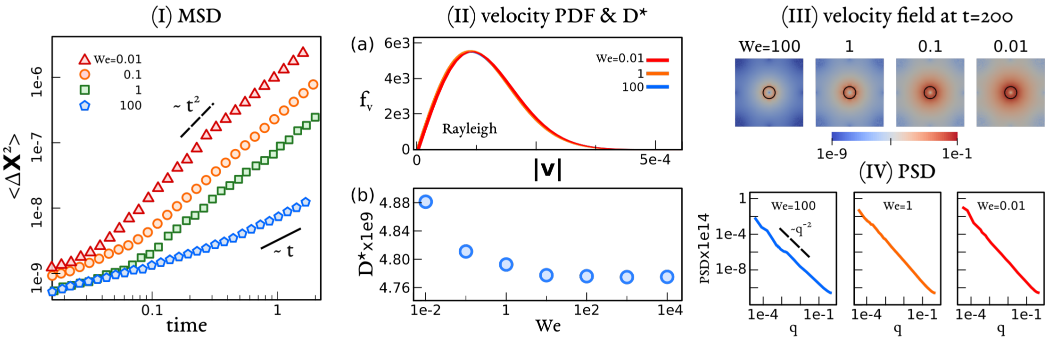

Figure 3.7.: 2D Brownian motion of a droplet for increasing hydrodynamics (Weber number We) with an initial radius $r_0 = 20$ with the composition noise amplitude $\xi_i = 0.001$: (a) Mean squared displacement with time. (b) Upper: the probability density function (PDF) of the velocity; lower: Brownian coefficient D^* with We. (c) Velocity field at $t = 200$. The black circles mark the particle-matrix interface with $\phi = 0.5$. The color bar (log) scales the velocity magnitude. (d) Power spectral density (PSD) of the particle displacement with the wavenumber q shows Brownian relationship $PSD \propto q^{-2}$.

gradient which induces the so-called Marangoni flow and propels the droplet Brownian motion. In simulations, I alter the Weber number We to control the surface tension force in the Navier-Stokes equation. As shown in the velocity-field snapshots in Fig. 3.7(c), a reduction in We intensifies the surface tension force which enhances the Marangoni flow around droplets. Due to the low viscosity, the droplet motion cannot be efficiently damped by the viscous stress $\eta\nabla^2\boldsymbol{u}$. Consequently, the stronger Marangoni flow results in the droplet motion transition from Brownian motion (large We) to ballistic motion (small We). This transition can be seen in the mean squared displacement (MSD) of Fig. 3.7(a), where the tendency of $\langle \Delta \boldsymbol{X}^2 \rangle \sim t^2$ is guided by the dashed lines. Meanwhile, the Weber number has a minor influence on the droplet velocity distribution $|\boldsymbol{v}|$. For instance, the Brownian coefficient D^* is increased by 5% when We number decreases from 100 to 0.01; but the droplet MSD presents a completely different scaling law with time. Moreover, I compute the power spectral density of the droplet displacement (PSD) and observe PSD following the -2 scaling law with the wavenumber q in Fig. 3.7(d). It indicates that both ballistic and Brownian motions of the droplet motion are emanated from the same origin - the compositional Gaussian white noise. After testing the droplet motion behaviours for various Pé and We, I categorize the droplet motion into three scenarios distinguished by the droplet trajectory and MSD. (I) Standard Brownian motion with sub-diffusive drift: the mean squared displacement $\langle \Delta \boldsymbol{X}^2 \rangle < 2D^* t$. The weak composition fluctuation is dissipated via inter-molecular diffusion, while the convection can be neglected. This scenario with large Péclect number and large Weber number corresponds to the dark-blue region in the motion phase diagram of Fig. 3.8(a). Here, I highlight the difference between rigid particles and soft Brownian droplets with the CHNS model. For the composition noise-dominated

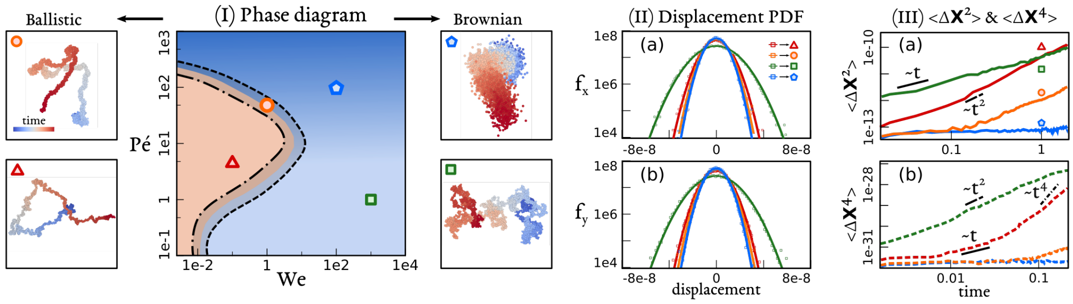

Figure 3.8.: The phase diagram of Brownian motion with various Weber number We and Péclet number Pé. The initial radius is $r_0 = 20$. CHNS model with the noise amplitude $\xi_i = 0.01$ is studied. (a) The motion phase diagram. The dot-dashed line and the dashed line separate the ballistic motion region (orange) from the standard Brownian motion region (blue) and the geometric Brownian motion region (light blue). The light grey region in between the dashed and dot-dashed lines show the transition area. Some exemplary motion trajectories are shown around: pentagon-standard Brownian motion; square-geometrical Brownian motion; triangle-ballistic motion; circle-transition region. (b) The probability density function (PDF) of the droplet displacement. Simulation: colored dots; normal distribution fitting: solid lines. Upper: x direction; lower: y direction. (c) The MSD $\langle \Delta X^2 \rangle$ and fourth cumulant $\langle \Delta X^4 \rangle$ of the example simulations with time.

scenario, the droplet drift displacement is

$$\begin{aligned}\Delta \boldsymbol{X} &= \int_\Omega dc\, \boldsymbol{x}\, d\Omega = \int_\Omega \nabla \cdot (\mathcal{M} \nabla \mu\, dt + \sqrt{\mathcal{M}}\, \boldsymbol{\xi}_i)\, \boldsymbol{x}\, d\Omega \\ &= \int_\Gamma (\mathcal{M} \nabla \mu\, dt + \sqrt{\mathcal{M}}\, \boldsymbol{\xi}_i) \cdot \boldsymbol{n}\, \boldsymbol{x}\, d\Gamma \\ &= \begin{cases} \quad 0, & \text{for rigid body;} \\ \neq \; 0, & \text{for droplets,} \end{cases}\end{aligned}$$

where the droplet centroid position $\boldsymbol{X}$ is static for the rigid body, due to the no-flux boundary condition $\nabla \mu \cdot \boldsymbol{n}$ and zero composition noise $\boldsymbol{\xi}_i = \boldsymbol{0}$ applied on the particle boundary Γ. But for droplets, there is a material flux across the interface which results in non-zero displacement, if and only if the composition fluctuation cannot fully dissipate at each time sequence. Because of the composition noise mean $\langle \boldsymbol{\xi}_i \rangle = \boldsymbol{0}$, the droplet will always go back to its origin with $\langle \Delta \boldsymbol{X} \rangle = 0$. As demonstrated by the blue pentagons in the MSD Fig. 3.8(b), the simulation presents the MSD with the sub-diffusion tendency lower than the $\langle \Delta \boldsymbol{X}^2 \rangle \sim t$ guided by the solid line. Meanwhile, the fourth cumulant $\langle \Delta \boldsymbol{X}^4 \rangle$ lies at around 10^{-32} with no time dependency which implies that the droplet displacement follows the standard Gaussian distribution.

(II) Geometric Brownian motion with diffusive drift: the convection comes into play. This scenario with small Pé and large We number corresponds to the light-blue regions in the motion phase diagram of Fig. 3.8. Only partially dissipated by the inter-molecular diffusion, the noise increases with the reduction in Pé and emerges the Marangoni flow propelling the droplet drift motion which gets gradually damped by the viscous stress. The droplet trajectory for both models shows the self-similar fractal structure and finally reaches the equilibrium with MSD $\langle \Delta X^2 \rangle \sim 2D^* t$. The fourth cumulant $\langle \Delta X^4 \rangle$ gradually increases with time t. At long time period, wefind $\langle \Delta X^4 \rangle \sim t^2$ similar to the observation in Ref. [54] as

$$\langle \Delta X^4 \rangle \approx 12\,\mathrm{Var}(D^*)\, t^2,$$

where $\mathrm{Var}(D^*)$ is the variance of D^*. The displacement distribution in the simulations still follows the Gaussian but without an exponential tail; see Fig. 3.8(b). It indicates that the non-constant Brownian coefficient D^* changing with time is produced by a mechanism differing from the diffusing-diffusivity models [55]. Understanding this phenomenon reveals that the deformable droplet deviates from its original perfect spherical shape. Hence, the perturbed surface energy results in the random droplet surface area S in Eq. 3.14 and thereby denotes the non-zero variance of the Brownian coefficient. Meanwhile, since every molecule inside the droplet is perturbed by random noises at every time point, the Brownian coefficient of the whole droplet becomes a time sequence that follows the Gaussian distribution with $\mathrm{Var}(D^*) > 0$, according to the central limit theorem. On the contrary, every molecule of the rigid body shares the same noise each time, which results in the zero variance of D^*.

(III) Underdamped ballistic motion: with a further reduction in We, the composition fluctuation induced Marangoni flow dominates. Once accelerated, the droplet can be slowed down neither by the diffusion nor by the viscous stress, resulting in the ballistic motion which deviates from the equilibrium as

$$\begin{aligned}
\langle \Delta X \rangle &= \bar{v}\, t \sim \sqrt{\mathcal{M}_0}\, \xi_i\, t, \\
\langle \Delta X^2 \rangle &= \langle \bar{v}\, t, \bar{v}' t' \rangle \sim \mathcal{M}_0\, \xi_i^2\, t^2, \\
\langle \Delta X^4 \rangle &\sim \ \mathrm{Var}(\mathcal{M}_0\, \xi_i^2)\, t^4 = \mathrm{Var}(D^*)\, t^4.
\end{aligned}$$

I observe that the short-time MSD ($t < 0.1$) shows the diffusion or sub-diffusion relation with time. The droplet motion range reduces with the increase in Pé, as illustrated by the y-intercept of MSD in Fig. 3.8(c). The later long-time behavior is vastly influenced by the composition noise induced Marangoni flow which is noticed by the steepening slope of MSD with a decrease in We. I notice that the dissipation mechanism for this Marangoni flow is lacking in the conventional stochastic models. Based on the FDT, only the composition perturbation $\sqrt{\mathcal{M}}\, \xi_i$ emanated from the free energy fluctuation is dissipated by the diffusion $\mathcal{M}\nabla^2\mu$, and the random body force $\sqrt{\eta}\,\mathbf{F}$ arising from the kinetic energy gets smoothed out by the viscous term $\eta\nabla^2\mathbf{u}$. Both noises are assumed as independent Gaussian with no covariance. However, in fact, their interaction has been observed and discussed in the capillary wave theory simulation and the dispersion relation analysis of Sec. 3.3.3. In fact, two types of noises are intertwined with each other by the surface stress tensor which is expressed mathematically by the stochastic surface tension force term $-c\nabla\mu$ in the Navier-Stokes equation and is not considered in the FDT. More investigations are needed to elucidate this problem in future work.

3.6. Conclusion

In conclusion, I have postulated and validated two types of stochastic phase-field models coupling with hydrodynamics to simulate the Brownian motion of particles and droplets. Propelled by the composition fluctuations with weak Marangoni effect, the particle/droplet proceeds the Brownian motion, depending on the amplitude of the random noise and the particle size, and the microscopic kinetic parameter. Moreover, by altering the parameters in the Navier-Stokes equations, the stochastic phase-field models go beyond the limitation of the Langevin equation only for the rigid body, and can also be utilized for soft deformable droplets. After testifying the results with the Einstein relationship within the equilibrium condition, I extend the model further into two off-equilibrium scenarios. i) When the composition noise-induced fluid flow becomes pronounced, the transition from Brownian motion to ballistic motion is observed which indicates the noise-induced fluid flow underdamped by the viscous stress. ii) The double particle simulation shows a stochastic-induced deterministic droplet motion, which plays a vital role in the coalescence of the multi-particle system and is hardly considered in the Langevin dynamics. Nevertheless, in the previous Cahn-Hilliard type phase-field models [56, 57], the stochastic noise terms are totally overwhelmed by the pronounced diffusion and Ostwald ripening, and simply applied as a trigger for the phase separation. Here, I reevaluate the importance of the noise term and focus on the stochastic droplet motions during the coalescence process, while the subordinate Ostwald ripening effect can be neglected. Thus, the missing linkage between the coarsening droplet and the randomly drifting rigid particle is connected. The model is also fully implemented in 3D. Weanticipate performing large-scale 3-dimensional multi-droplet simulations in forthcoming research to understand the underlying mechanisms of the micro-droplet motions, especially for the gelation process of soft matter materials.

4. Multi-component phase separation induced multi-layer emulsion[1]

4.1. System definition

In this chapter, I apply Cahn-Hilliard model to simulate the high-order multiple emulsion which is engendered by the liquid-liquid phase separation for the diethyl phthalate (DEP)-water-ethanol ternary system. This chapter is based on Ref. [28].

Spontaneous formation of 'onion-like' multiple emulsions [58, 59, 60] via liquid-liquid phase separation in ternary polymer solutions [15, 61, 62, 63] is widely utilised to design complex droplets consisting of sequentially encapsulated oil and water layers. The compositions of DEP (or oil), water, and ethanol are space ($\mathbf{x}$) and time (t) dependent, which are denominated as $c_1(\mathbf{x}, t)$, $c_2(\mathbf{x}, t)$ and $c_3(\mathbf{x}, t)$, respectively. In the following, I will utilise the composition vector $\mathbf{c} = (c_1, c_2, c_3)$ to describe the emulsion state. Concerning the constraint $\sum_{i=1}^{3} c_i = 1$, there are two independent compositions: c_1 and c_2. The space and time dependent composition of polymer A, polymer B, and solvent is defined as $c_1(\mathbf{x}, t)$, $c_2(\mathbf{x}, t)$, and $c_3(\mathbf{x}, t)$, respectively, and subjected to the constraint of the incompressible condition $\sum_{i=1}^{3} c_i = 1$.

To reproduce the phase diagram of DEP-water-ethanol, following parameters are adopted for its free energy density. Concerning the repulsive interaction of DEP with water, I assume a positive $\chi_{12} = 3.0$. On the contrary, because of the good miscibility of oil and water in ethanol, the interaction parameters χ_{13}, χ_{23}, and χ_{123} can be qualitatively described as 0.5, 0.5, and -3.0, respectively. Since the molar mass of DEP is 10 times larger than water, N is chosen to be 5. Taking the given parameters, the free energy density of the oil-water-ethanol system is demonstrated by the heat map in Fig. 4.1(I). The binodal and spinodal lines are indicated by red solid line and dashed line, respectively. The obtained phase diagram is in good accordance with the one reconstructed from the experiments in Fig. 4.1(II)[15]. The surface tension values for DEP and ethanol utilised in eq. (2.4) are normalized by the surface tension of pure water ($\sigma_2^0 = 7.28 \times 10^{-2}\mathrm{N/m}$), namely $\sigma_1 = 0.5\sigma_2^0$ and $\sigma_3 = 0.3\sigma_2^0$. Moreover, as reported in previous researches, the surfactant into water is a crucial ingredient for the multiple emulsion [64, 65, 66]. Owing to its low content ($\simeq$ 0.1 $wt.\%$) and negligible influence on the phase diagram, as well as for the sake of simplicity, the surfactant is not treated as a single component in our model. The effect of the surfactant is considered by altering the surface tension of water σ_2, depending on which type of the surfactant is adopted.

---

[1] Copyright notice: This chapter is reprinted (adapted) with permission from Zhang H., Wu Y., Wang F., Britta N. Phase-field modeling of multiple emulsions via spinodal decomposition[J]. Langmuir, 2021, 37(17): 5275-5281. Copyright 2021 American Chemical Society.

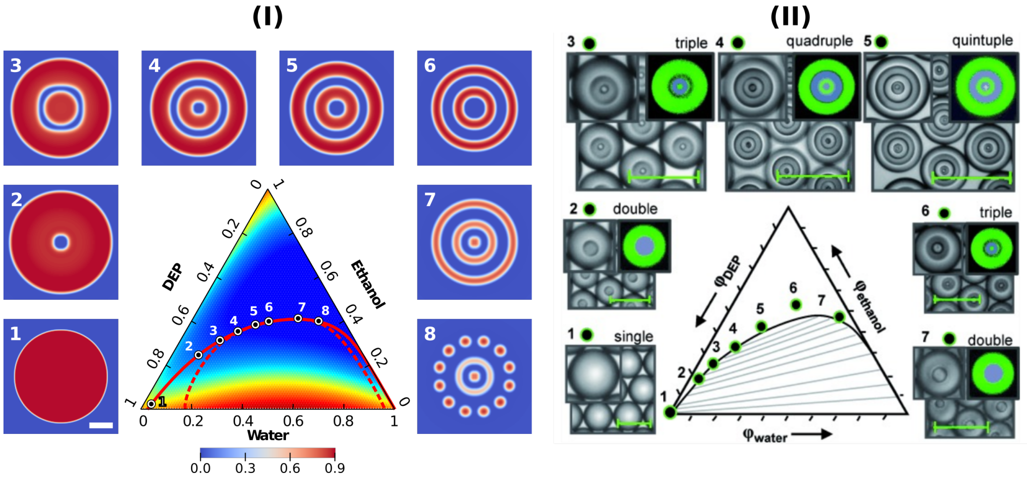

Figure 4.1.: (I) Middle: the phase diagram of the DEP-water-ethanol system. The magnitude of the free energy density is described by the heat map (red: high; blue: low). The binodal and spinodal compositions are depicted by the red solid line and dashed line, respectively. The white-black dots indicate the initial compositions for the emulsion droplets considered in the simulation with the initial water content $c_2^0 = 0.029, 0.10, 0.15, 0.20, 0.25, 0.30, 0.40, 0.50$. Surrounding: snapshots (1)-(8) depict the simulated morphologies of droplets at the simulation time $t = 2500$. The corresponding initial setups are sequentially numbered in the phase diagram. The scalar bar denotes 20. The color bar beneath illustrates the oil (DEP) composition for all the simulation snapshots in this work. (II) The experiment morphologies of the emulsions with the reconstructed phase diagram based on the experimental results. Reproduced with permission [15]. Copyright 2014, WILEY-VCH Verlag.

4.2. Simulation setup

In this work, the finite difference method and the explicit Euler scheme are implemented to solve the Cahn-Hilliard equation with the equidistant Cartesian mesh, which is subject to the Neumann boundary conditions. All the physical parameters are non-dimensionalized by the characteristic length $x^* = 2 \times 10^{-6}$m, surface tension of pure water ($\sigma_2^0 = 7.28 \times 10^{-2}$N/m), and self-diffusivity of pure water ($D_w = 2.29 \times 10^{-9}\text{m}^2/\text{s}$).

4.3. Model validation

In this section, I present the validation of our simulation model by changing the Flory parameter χ to recover the feasible phase diagram which is in line with the experiments. The numerical stability is also examined by changing the resolution Δx and the theoretical surface tension is recovered with our model.

4.3.1. Resolution

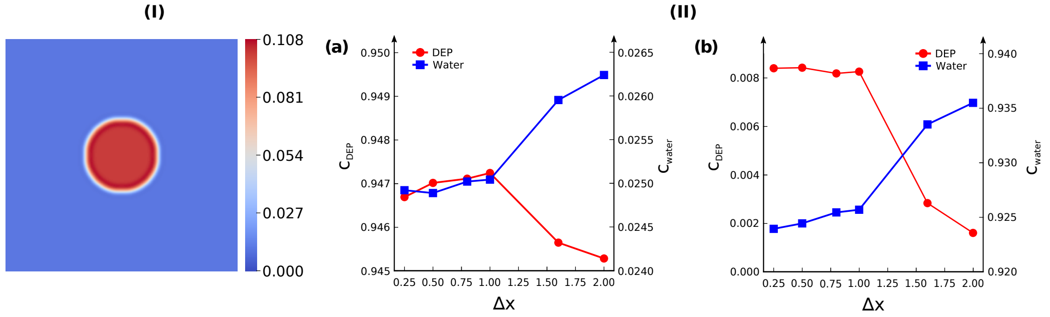

Figure 4.2.: (I) The emulsion droplet with an initial composition $\mathbf{c}^0 = (0.101453, 0.5, 0.398547)$ and radius $r^0 = 16$. (II) Mesh resolution study. (a) The equilibrium composition of DEP and water inside the droplet as a function of mesh size. (b) The equilibrium composition of DEP and water outside the droplet as a function of mesh size. The color bar scales the oil (DEP) concentrations.

Firstly, the mesh fineness validation is preformed to testify the numerical calculation convergence. Here, I simulate a droplet amid the matrix with various resolutions by reducing the mesh fineness $\Delta x (= \Delta y)$ from 2.0 to 0.25. As demonstrated in Fig. 4.2(I), the droplet with an initial composition $\mathbf{c}^0 = (0.101453, 0.5, 0.398547)$ and radius $r^0 = 16$ is placed in the center of a 200×200 domain. The composition in the matrix is initially set as $\mathbf{c}^0 = (0.01, 0.95, 0.04)$. The convergence of the model is characterized by measuring the equilibrium composition of DEP and water inside (outside) the droplet with increasing Δx, as shown in Fig. 4.2(II). With an increase in the mesh fineness, the equilibrium compositions converge gradually. Thence, $\Delta x = 0.5$ is a an acceptable compromise to trade-off between the simulation precision and computational efforts.

4.3.2. Interfacial tension of DEP and water

Secondly, the interfacial tension between DEP and water is numerically calculated with the total excess free energy at the interface, which reads

$$\sigma = \int_0^\infty \left[f(c_1, c_2, c_3) - f_{eq} + \sum_{i=1}^{3} \sigma_i \epsilon (\nabla c_i)^2 \right] d\mathbf{x}. \tag{4.1}$$

Here, f_{eq} denotes the equilibrium free energy density and $\mathbf{x}$ is the normal direction of the interface. According to the Flory-Huggins theory [32], the following free energy density formulation is applied

$$f = \frac{\sigma_2^0}{\epsilon} \left[T \left(\frac{c_1 \ln c_1}{N} + c_2 \ln c_2 + c_3 \ln c_3 \right) + \sum_{\substack{i,j=1,2,3 \\ i<j}} \chi_{ij} c_i c_j + \chi_{123} c_1 c_2 c_3 \right]. \tag{4.2}$$

Here, T is the temperature and N indicates the polymerization degree of DEP. The interaction between component i and j is characterized by χ_{ij}. The last term in eq. (4.2) describes the interaction between all three components. For simplicity, I perform 1D simulation (domain size: 200×1) with an initial composition $\mathbf{c}^0 = (0.97300, 0.02679, 0.00021)$ ($\mathbf{c}^0 = (0.0000149, 0.999624, 0.0003611)$) in the DEP (water)-riched phase. In this case, $\mathbf{x}$ manifests the x-direction. From the simulated composition distributions along the interface, the interfacial tension between DEP and water is computed by eq. (4.1) as $0.526\sigma_0$ (38.34N/m), which is in well accordance with the experiments.

4.3.3. Selection of Flory-Huggins parameters

Thirdly, the criterion of the Flory-Huggins parameter between DEP and water χ_{12} is the most important factor. A) The Flory parameter χ_{12} scales the interfacial tension of the DEP-water interface. At the given temperature and composition, the interfacial tension can be determined by experiments. When the concentration of ethanol is so small that it can be neglected, the interfacial tension of the DEP-water interface is proportional to $\sqrt{\chi_{12}}$. B) The driving force of the phase separation can be written as $\partial_{cc} f$ which is proportional to χ_{12}. More suffice to say, χ_{12} can also influence the equilibrium compositions. In a word, the Flory-Huggins parameter χ_{12} is the most crucial parameter that controls both the phase separation and interfacial tension of the system and cannot be changed arbitrarily.

Contrarily, the selection of χ_{13}, χ_{23}, and χ_{123} are not so constraint as χ_{12}. The only criterion is the phase diagram, for which the miscible gap appears when these values are large enough. As presented in Fig. 4.3, with increasing χ_{13} and χ_{23} from -2 to 2 (T⟶M⟶B), the phase separation between DEP and ethanol begins to appear. Compared (T) with (M), I could conclude that the minus χ_{13} and χ_{23} has little impact on the phase diagram, which also proofs the good robustness of the system. Meanwhile, with the growth of χ_{123} from -6 to 3 (L⟶M⟶R), the repulsive interaction between three species increases, which leads to the extension of phase separation in the middle of the phase diagram into the ethanol riched region.

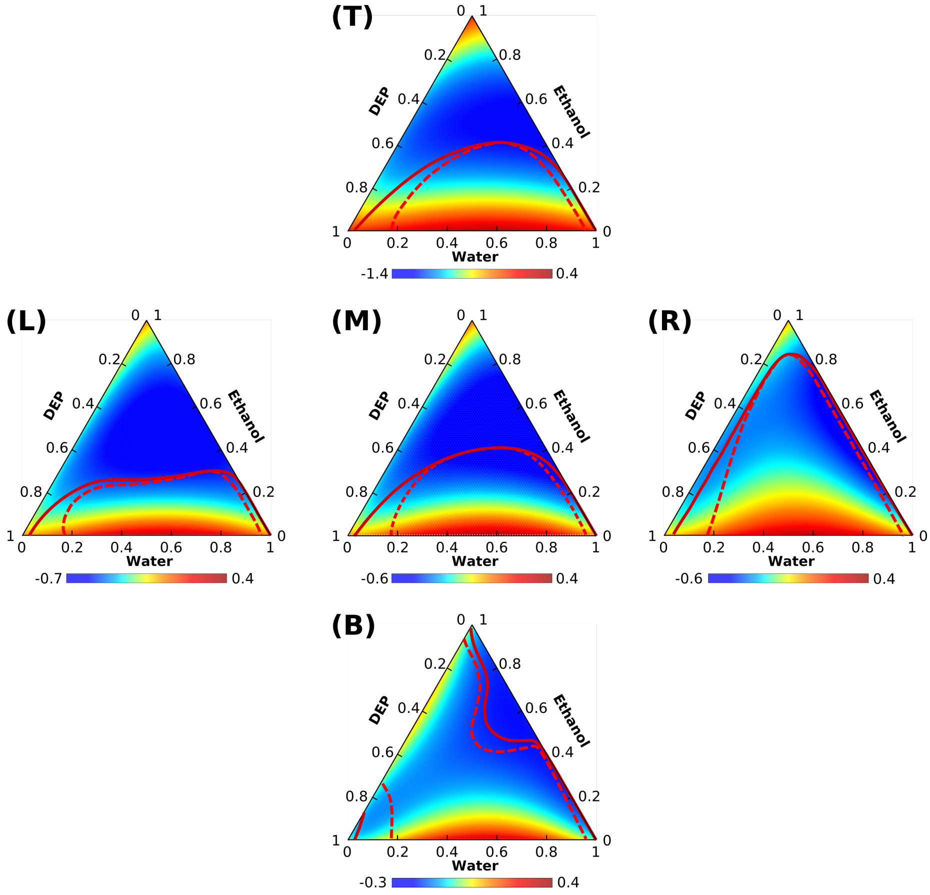

Figure 4.3.: Phase diagrams of DEP-water-ethanol system with different Flory-Huggins parameters. Solid dark red lines: binodal; dashed red lines: spinodal. (M) the phase diagram in the main text with $\chi_{12} = 3.0$, $\chi_{13} = \chi_{23} = 0.5$, $\chi_{123} = -3.0$; (T) top: $\chi_{13} = \chi_{23} = -2.0$; (B) bottom: $\chi_{13} = \chi_{23} = 2.0$; (L) left: $\chi_{123} = -6.0$; (R) right: $\chi_{123} = 3.0$. Color bar labels the magnitude of the free energy density f.

4.3.4. Validation of the phase diagram

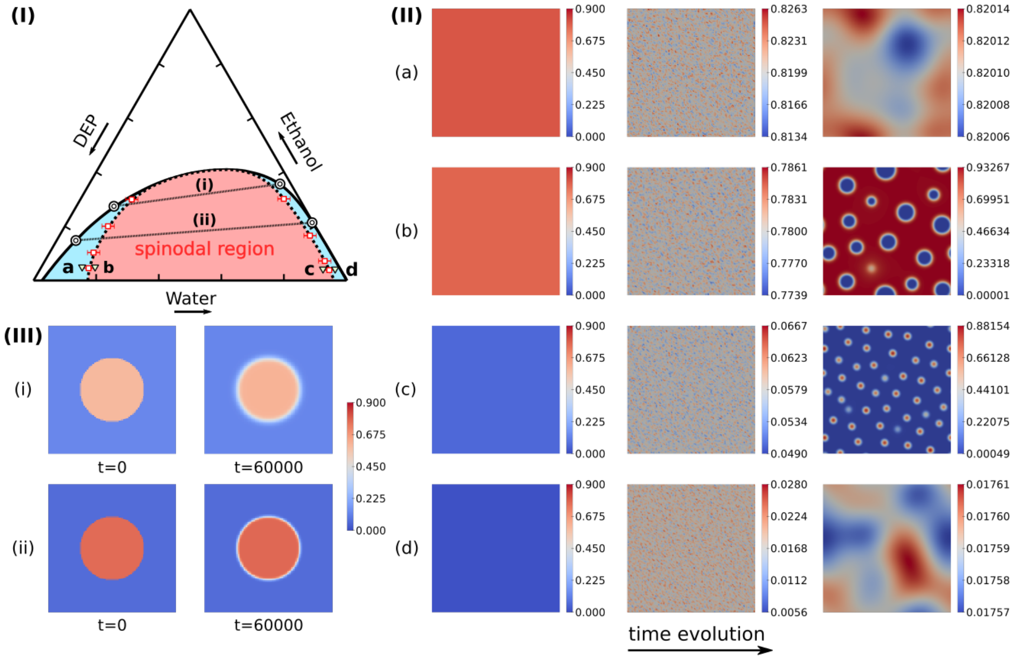

Figure 4.4.: (I) The phase diagram of the DEP-water-ethanol system. The binodal and spinodal compositions are plotted with the solid line and dashed line, respectively. The white-red square with error bars depict the simulated spinodal line. The triangles *a*, *b*, *c*, *d* label four initial compositions to valid the spinodal decomposition with simulation snapshots shown in (II). Two pairs of white-black dots linked with tie lines point the binodal compositions. (III) depicts the validation of the binodal compositions. The color bar scales the oil (DEP) concentrations.

Finally, I verify the capability of the multi-component phase-field method to model the emulsion behaviours. As shown in Fig. 4.4(I), I plot the binodal and spinodal lines in the DEP-water-ethanol phase diagram with solid and dashed lines, respectively. The spinodal region is highlighted with rose color. The white-red square denotes the simulated spinodal compositions. The error bars are measured with the binary search algorithm. I choose four typical initial compositions *a*, *b*, *c*, and *d* from the phase diagram and disturb the whole domain with the Gaussian white noise (variance $\delta^2 = 0.01$). It is noteworthy that *a* and *d* are out of the spinodal region, while *b* and *c* are within it. As can be seen from Fig. 4.4(II), the spinodal decomposition occurs in the initial compositions *b* and *c*, while no obvious phase separation happens for the initial compositions *a* and *d*. This result is in good consistent with the calculated spinodal line in the phase diagram.

The blue colored area highlights the binodal region of the system. The tie lines (i) and (ii) connect two pairs of binodal compositions (the white-black dots) which correspond to two pairs of equilibrium compositions. The left white-black dots mark the compositions of the oil-rich droplet and the right dots label the contents of the water-rich surrounding. To valid the binodal compositions, I fill the domain with a oil-rich (red) droplet surrounded by oil-poor environment (blue), by which the initial compositions are selected from the tie lines (i) and (ii) in Fig. 4.4(I). After a long time simulation (t=60000), the compositions are stable and stay in well accordance with the calculated binodal compositions in the phase diagram.

4.4. Results and discussion

In this section, I apply the CH model to investigate the morphological evolution of the multiple emulsion propelled by liquid-liquid phase separation. The influences of initial emulsion compositions, surface tension, and emulsion droplet size upon the number of the multi-layer are focused on.

4.4.1. Emulsion composition

In first part, 8 homogeneous emulsion droplets with an initial radius $r^0 = 40$ are surrounded by the identical water over-saturated environment with the composition $\mathbf{c} = (0.01, 0.95, 0.04)$. The initial droplet compositions $\mathbf{c} = (c_1^0, c_2^0, c_3^0)$ are picked from the binodal line of the system with water content rising from 0.029 to 0.50, as sequentially numbered by the white-black dots $(1) - (8)$ on the phase diagram in Fig. 4.1(I). Due to the surfactant, the surface tension of water is significantly reduced and can be represented by setting $\sigma_2 = 0.1\sigma_2^0$ [15]. The simulation snapshots $(1) - (8)$ aside demonstrate the morphologies of the corresponding emulsions at $t = 2500$.

It is noteworthy that the multiplicity of the droplets is highly correlated with the initial composition which shows an excellent accordance with the experimental observations in Fig. 4.1(II). From the perspective of thermodynamics, this phenomenon can be explained with the help of the phase diagram. For composition (1), the emulsion builds no extra layer. Since this composition stays far away from the spinodal region, the phase separation is impossible to be propelled by the water diffusing from the outside. Hence, the droplet quickly equilibrates itself by releasing water into the surrounding without entering the spinodal region. Contrarily, by adding the water content from composition (2) to (7), the simulated oil-water interface begins to add up from 2 to 5 layers. This tendency is also confirmed in the experiment results, as demonstrated in Fig. 4.1(II). The reason for the distinct morphological evolution can be elucidated as follows. With the additional water content in the initial emulsion, the binodal compositions approach the spinodal line, by which the stable region of the droplet shrinks (see Fig. 4.1(I)). Hence, as a tiny amount of excessive water diffuses gradually inwards the interior of the droplet, the local composition inside the droplet enters the spinodal region. Once the phase separation is triggered, the excessive thermodynamic energy quickly transfers into the surface energy of the emulsion and thus the multiple layers are produced.

Another observation is that from composition (1) to (8), the thickness of the DEP-rich layer (red colored areas in the snapshots of Fig. 4.1(I)) decreases significantly with the reduction of the initial composition c_1^0 in the mixture. According to the lever rule, when the initial composition c_1^0 of the droplet decreases, the volume fraction (V_f) of the oil-rich layers also decreases; the volume fraction of the water-rich layers increases. Consequently, the thickness of the DEP-rich layers is positively correlated with its V_f and decreases with the drop of the initial composition c_1^0 inside the emulsion.

Under extreme circumstance, the volume fraction of the oil-rich layers is so small that a morphological instability is observed. For the composition (8), the thin DEP-rich layer breaks up into tiny droplets. In this scenario, the surface energy minimization dominates over the spinodal decomposition and the oil layer becomes unstable breaking up into droplets to minimize the surface energy. This observation implies the great importance of the surface tension. During the evolution of the emulsion, its excess thermodynamic energy for the phase separation declines, while the total surface energy surges. The formation of the multi-layers is, then, the consequence of these two vying energies. Hence, for a better understanding of the physical mechanisms for the multiple emulsion, the interplay of both phase separation and surface tension should be heedfully investigated.

4.4.2. Surface tension

In this part, one droplet with composition $\mathbf{c} = (0.1909, 0.40, 0.4091)$ (composition (7) in Fig. 4.1(I)) and an initial radius $r^0 = 40$ is set in the homogeneous surrounding with $\mathbf{c} = (0.01, 0.95, 0.04)$, as shown by the snapshot (I) in Fig. 4.5(I)(a). To peer the effect of the surface tension on the formation of multi-layer, I alter σ_2 to analyse the transient states by considering the evolving competition between phase separation and surface energy minimization.

The kinetic pathways for $\sigma_2/\sigma_2^0 = 10, 5.0, 1.0$ are plotted in the ternary phase diagram, as illustrated in Fig. 4.5(I)(a), (b), and (c), respectively. Here, three representative compositions inside the droplet are traced, namely, the compositions with a maximal (red line) and minimal value (blue line) for c_1, and the composition at the droplet center (gold line). All simulations start with the identical setup labelled as I, except different values of σ_2. The green arrows with the letter M point out a crucial mid-point, and E denotes the terminal of the simulation. The simulation snapshots at these three points are pictured beneath the corresponding kinetic trajectories. At the beginning, the red and blue lines separate from each other which indicates the start of the spinodal decomposition. This process is achieved via the penetration of the over-saturated water into the droplet. As the location with maximal c_1 (red line) moves leftwards on the phase diagram and forms the oil-rich/water-poor layer, the position with minimal c_1 (blue line) shifts rightwards for the oil-poor/water-rich region. Therefore, the oil-water interface is being established in between.

Due to the relatively large surface tension of water by setting $\sigma_2/\sigma_2^0 = 10$ in Fig. 4.5(I)(a), the demanding energy for one stable oil-water interface cannot be supplied by the thermodynamic energy of the system. Thus, after an abrupt turnover at point M in the trajectory diagram, the oil content difference between the red and blue lines starts to decline which implies that the phase separation is suppressed by the effect of the surface area minimization. Under this circumstance, the dominant surface tension pushes the emulsion to form a small oil-rich sphere which possesses the lowest surface area of all shapes. Consequently, the indistinct internal oil-water interface vanishes from the snapshots M to E.

With a smaller $\sigma_2/\sigma_2^0 = 5.0$ (Fig. 4.5(I)(b)), the proceeding spinodal decomposition continuously makes its contribution to build the inner oil-water interface. As shown by

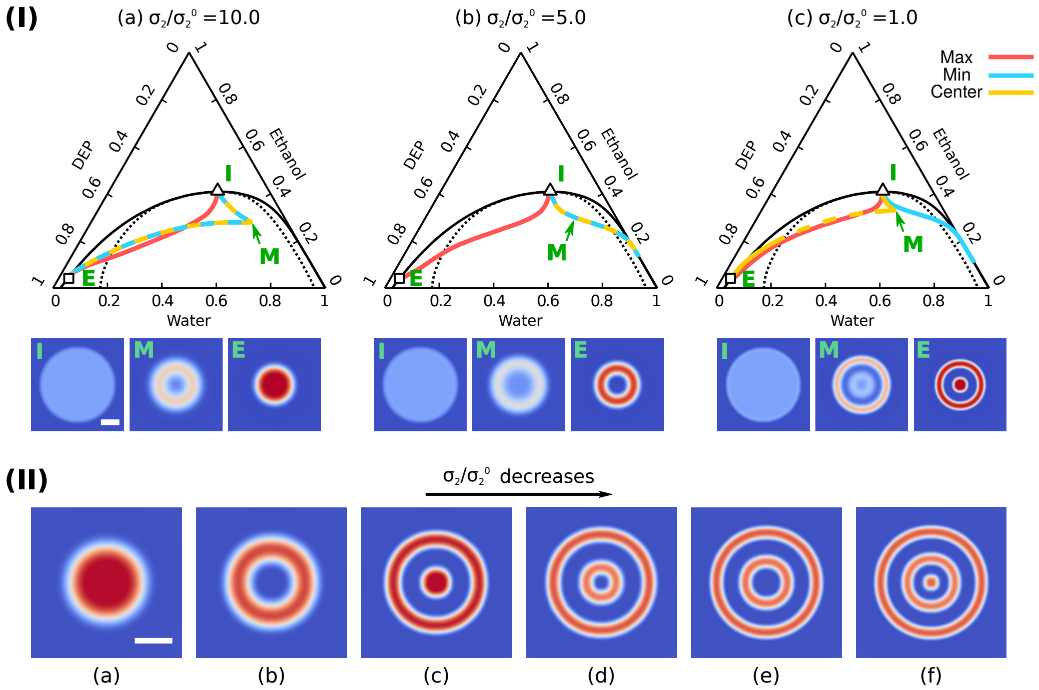

Figure 4.5.: The morphological evolution of the emulsion with respect to the surface tension σ_2. (I) Trajectory diagrams with the kinetic pathways of 3 specific compositions. The red/blue lines trace the compositions with the max/min oil content (c_1) amidst the droplets, while the gold line guides the evolving composition at the droplet center. (a) $\sigma_2/\sigma_2^0 = 10.0$, (b) $\sigma_2/\sigma_2^0 = 5.0$, and (c) $\sigma_2/\sigma_2^0 = 1.0$. All initial setups are consistent with the composition (7) in Fig. 4.1(I). The snapshots beneath the trajectory diagrams picturize the oil distributions at three crucial moments: *I* (initial), *M* (mid), and *E* (end), which are labeled in the respective trajectory diagrams as well. (II) Emulsion morphologies with decreasing σ_2 at an intermediate state ($t = 1250$). From (a) to (f), σ_2/σ_2^0 declines from 10 to 0.1. The scale bar denotes 20.

the trajectory diagram in Fig. 4.5(I)(b) and the corresponding snapshots *I*, *M*, and *E*, the DEP content gap between maximal and minimal c_1 grows ceaselessly and the blurred second interface becomes more and more stable and clear. This process is achieved by phase separation overcoming the surface area minimization. In the end, one double emulsion is engendered.

For an even lower $\sigma_2/\sigma_2^0 = 1.0$ (Fig. 4.5(I)(c)), the morphological evolution is vastly controlled by the phase separation, rather than the surface energy minimization. This is strongly proofed by the formation of one tiny oil-rich droplet in the emulsion center, as pictured in the snapshot *E*. Despite of the relatively large curvature of the tiny droplet, it survives with time, which leads to the formation of a triple oil-water layers emulsion.

Next, I further reduce σ_2 till $0.1\sigma_2^0$ and the corresponding emulsion morphologies are illustrated in Fig. 4.5(II). More extra layers (up to 5 with $\sigma_2/\sigma_2^0 = 0.1$ in (f)) are generated and the size of the multi-layer emulsion also increases. This result suggests that the subordinate roll of the surface tension is gradually overwhelmed by the phase separation which decides the morphological evolution of the emulsions magnificently.

4.4.3. Size effect

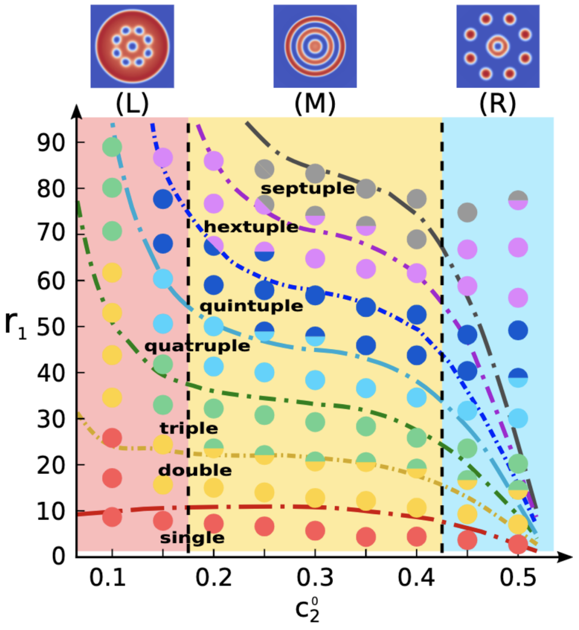

Figure 4.6.: Morphology diagram with respect to the initial water content c_2^0 and droplet outermost radius r_1. The diagram is divided into three areas: (L), (M), and (R). Typical emulsion morphologies in each area are shown at the top of the figure: (L) Emulsion encapsulating water droplets; (M) onion-like oil-water layers; (R) breakup of oil-rich layers into satellites. The colored circles from red to gray present the number of emulsion layers (from single to septuple), which is in good agreement with the prediction of the dot dashed iso-multiplicity lines fitted with the simulation results.

As aforementioned, the multiplicity of the emulsion is also highly related to the initial size of the droplet. In this part, I will study the relationship between the layer multiplicity and the droplet size by altering the initial radius r^0 from 10 to 100 with a constant $\sigma_2/\sigma_2^0 = 1.0$. To reveal the combined impact of size and composition (especially c_2) on the final morphology, a series of initial compositions on the binodal line of the phase diagram in Fig. 4.1(I) with initial water content c_2^0 adding from 0.10 to 0.50 are taken into consideration. The resulting morphology diagram in Fig. 4.6 illustrates the layer multiplicity varying with the droplet size and initial c_2^0. Here, owing to the shrinkage of the droplet, the droplet size is represented by the outermost radius r_1 measured at the specific transient moment with the maximal multiplicity of oil-water interfaces. The growing emulsion multiplicities are distinguished by distinct circles with the rainbow order colors and separated into iso-multiplicity zones by the sequence of dot-dashed curves which are mathematically modelled based on the simulation results and will be introduced later. The Janus circles depict the transition between two neighboring regions where the midmost oil-water interface is so blurred that vanishes due to the surface energy minimization. Moreover, the obtained morphology diagram is divided into three regions with respective simulation snapshots: (L) emulsion confining water droplets (rose red area); (M) the continuous DEP-rich multiple layers (golden region); (R) emergence of the tiny oil satellites (blue section). Typical emulsion morphologies in the three regions, (M), (L), and (R) are demonstrated in Fig. 4.7.

In the middle area (M), the emulsions of the droplet with compositions (3)-(7) increase their multiplicities with the droplet size. The iso-multiplicity zones which are demarcated by the dot-dashed lines show an excellent consistency with previous experiments [15]. For clarity, as depicted in the lower inset of Fig. 4.7(I)(b), I number the outermost oil-water interface of the droplet as the 1st layer, with the increasing number indicating its internal interfaces sequentially. Then, as exemplified in Fig. 4.7(I) with composition (5), the radius of the i-th layer r_i increases linearly with the initial size r^0 (see the upper inset of Fig. 4.7(I)(b)). Consequently, for every layer in emulsion (5), its radius r_i with respect to the radius of its inner successor r_{i+1} falls onto the identical linear scaling curve, namely $r_{i+1} = ar_i + b$. Apparently, by applying recursion, the function for r_i is expressed as $r_i = b(1 - a^i)/(1 - a)$. Moreover, because the phase separation plays a vital role during the whole process, the fitting parameters a and b can be both related with the magnitude of the phase separation, which is qualitatively represented by c_2^0. Thus, the radii of ith layer for each setup are written as the function of the c_2^0 and depicted as the dot-dashed lines in Fig. 4.6. The detailed fitting method for the multiplicity is demonstrated as follows.

4.4.4. Fitting of emulsion multiplicities

In this part, I show the functional relationships for the radius of the initial water composition c_2^0. Here, the rainbow ordered colors are selected to represent the sequence of the layers, as the red color denotes the outermost 1st oil-water interface of the droplet and yellow for the inner 2nd layer; green-3rd; cyan-4th; blue-5th; violet-6th. Firstly, as demonstrated in the column (a) of Fig. 4.8(I)-(V), I measure the simulated radii of the ith oil-water interface with varying initial compositions (3)-(7) marked in the Fig. 4.1 of the main text, by which the initial water composition c_2^0 ranging from 0.2 to 0.4. The radii for

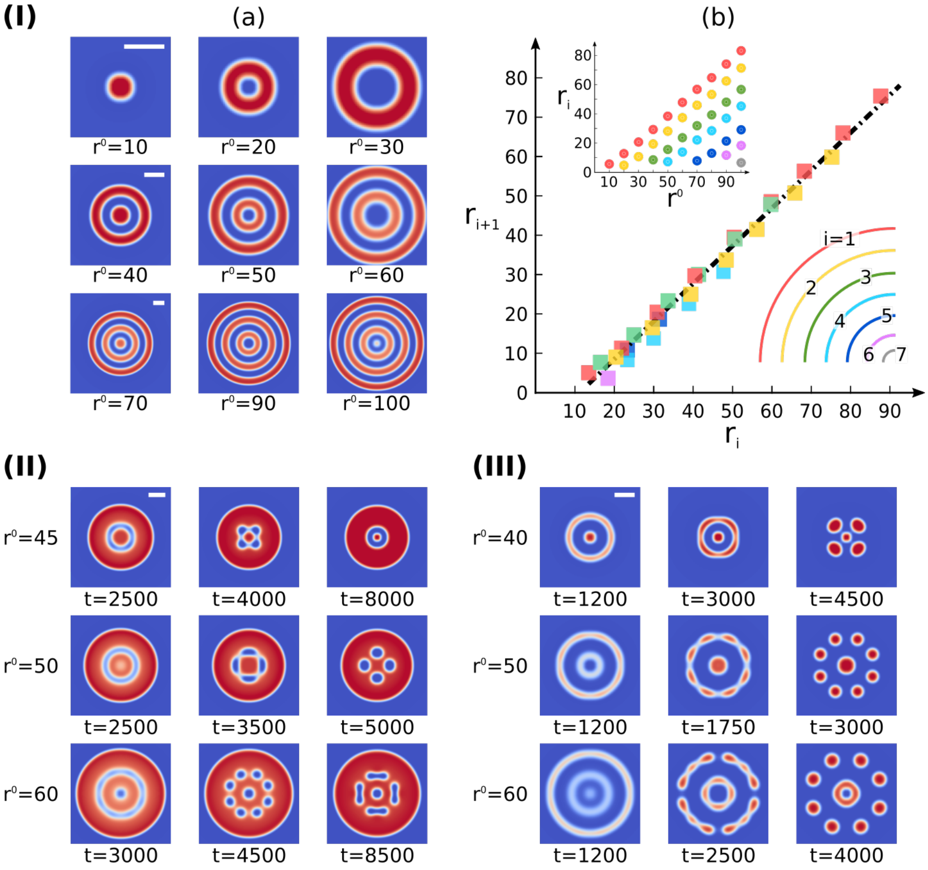

Figure 4.7.: (I) (a) The emulsion morphology for composition (5) in Fig. 4.1 with the initial radius varying from 10 to 100. The snapshots are taken at the time with maximal multiplicity. (b) The linear scaling law for composition (5) between the radius of ith and $(i+1)$th layers as $r_{i+1} = ar_i + b$. The inset: upper: the dependence of r_i on the initial radius r^0. Lower: the rainbow order colors from red to violet represent the numbers of the oil-water interfaces adding from 1 to 7. (II) and (III) The morphology evolution of the emulsion for the initial compositions (2) and (8) in Fig. 4.1, respectively. All scale bars denote 20.

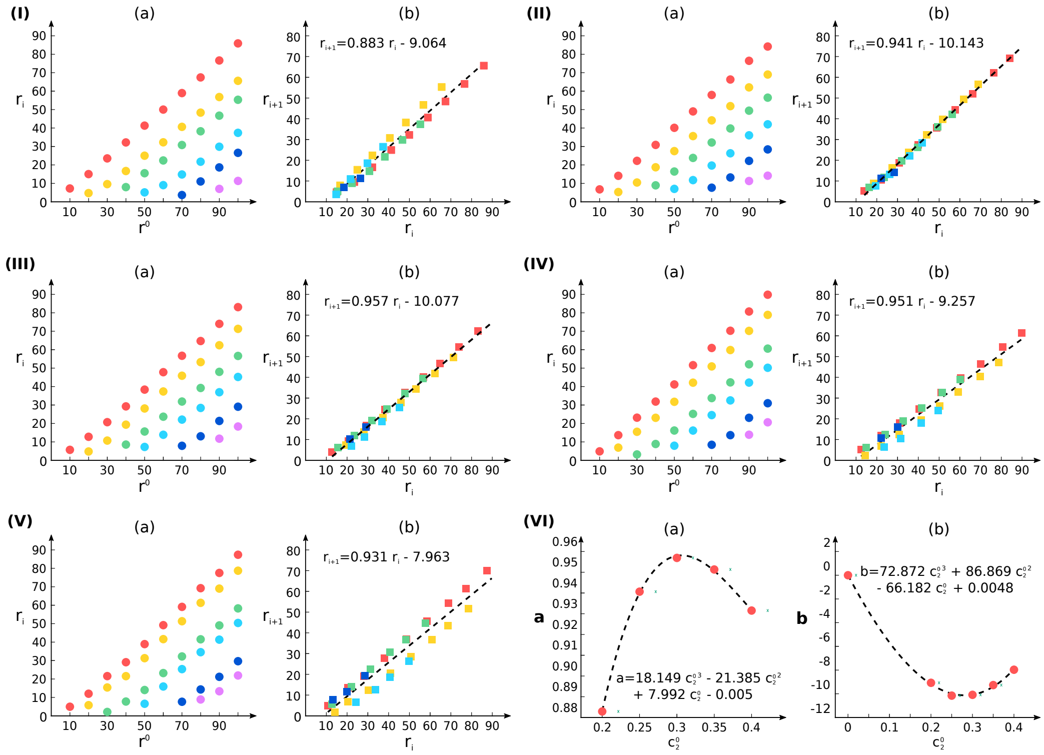

Figure 4.8.: (I)-(V) The linear scaling law for (a) the radius of the ith layer r_i vs. the radius of initial droplet r^0 and (b) the radius of $(i+1)$th layer r_{i+1} vs. the radius of its inner successor layer (ith) r_i. (I)-(V) stand for compositions (3)-(7) with initial water composition c_2^0 ranging from 0.2 to 0.4 marked in the Fig. (1) of the main text. The linear relationship between the radius of ith and $(i+1)$th layers is fitted as $r_{i+1} = ar_i + b$. (VI) The functional relationship for the parameter a vs. initial water composition c_2^0 and b vs. c_2^0.

each layer show a good linear correlation with the initial droplet radius r^0 ranging from 10 to 100. Secondly, for each initial composition, the relationship between the radius of ith layer r_i vs. the radius of its outer layer r_{i+1} are displayed in the column (b) of Fig. 4.8(I)-(V). Clearly, for every initial composition, the relationships between the radius of ith and $(i+1)$th layers fall on to the respective linear scaling law which are fitted as $r_{i+1} = ar_i + b$. In this way, the radius of the ith layer can be recursively computed with the following arithmetic sequence,

$$r_{i+1} = ar_i + b = a^2 r_{i-1} + ab + b = a^3 r_{i-2} + a^2 b + ab + b \cdots . \tag{4.3}$$

By assuming the 0th layer has the zero radius. The radius of the ith layer is expressed as

$$r_i = b\,\frac{1-a^i}{1-a}. \tag{4.4}$$

Since the parameters a and b vary with the initial composition, I fit a and b as the cubic polynomial functions of c_2^0 in Fig. 4.8(VI) with the fitting equations indicated in the corresponding figures. For each initial setup, the emulsion droplet can form n oil-water interfaces, when its radius is larger than the r_n fitted with Eq. (4.4). With the same fitting method, the iso-multiplicity lines in Fig. (3) in the main text are also calculated.

At the regions of (L) and (R), fitting curves deviate largely from the simulation results. The misfitting is attributed to the prevalent effect of the surface energy minimization. In the left area (L) where $c_2^0 < 0.20$, at the beginning of the evolution (see Fig. 4.7(II) first column), indistinct multi-layers are produced by the phase separation. When the oil-water interfaces are gradually being established, the surface energy of the system rises and dominates the process vastly. For the sake of the surface energy minimization, the thinner water-rich layers prefer to break up into droplets, rather than the thicker oil-rich rings (see Fig. 4.7(II) second column). Moreover, due to the large curvature, as well as the shrinkage of the whole emulsion, these tiny droplets may also contact and merge with each other. Particularly in the third column of Fig. 4.7(II), several multi-chambered droplets with distinct patterns are observed which can be widely used as biodegradable polymer shells for the drug delivery. Similarly, the scenario of the right region (R) is controlled by the same physical picture. Here, the component oil (DEP) forms thin layers during the spinodal decomposition, which break up into micro satellites. As shown in Fig. 4.7(III), more oil-rich satellites with radius $r < 10$ are born by a bigger initial emulsion. These transient morphologies are seldom reported and should be further confirmed by experiments.

4.5. Conclusion

In summary, I present a multi-component Cahn-Hilliard model to simulate the formation of the multi-layer polymeric emulsion via liquid-liquid phase separation. By tracing the local composition inside the droplets during the emulsion, I elucidate the kinetics for the establishment of the ’onion-like’ multi-layers. The simulation results suggest that the surface energy minimization is a crucial mechanism that competes with the spinodal decomposition. The joint effect of these two mechanisms decides the transient morphologies of the emulsion droplets. By altering the surface tension, size, and composition of the mixture, distinct intermediate microstructures are observed, ranging from multi-chambered droplets to micro satellite particles. Additionally, the morphology of the emulsion should also show its higher complexity in 3D simulations, in which the curvature of the interfaces can magnificently influence the intermediate microstructures of the droplet and shall be investigated in the future. Moreover, another important issue remaining to be resolved is the morphological stability of the multi-layers under the impact of fluid flow. A possible exploitation in this direction might be coupling the Navier-Stokes equations with the present model. It should be noticed that the present model only considers the diffusion mechanism for the emulsion. The timescale of the emulsion from the present model overall shows a fair agreement with the experiments [67] (see Fig. S5 in the supplementary document of Ref. [28]), although there are minor discrepancies. The small discrepancies of the timescale between simulations and experiments may be attributed to the fact that fluid flow, e.g. Marangoni flow, may occur during the emulsion process in reality. The hydrodynamic effect has been overlooked in the current model and will be discussed in a forthcoming work. Additionally, the hydrodynamics also has an impact on the timescale of the structure evolution, since the surface tensions may be altered by the Marangoni flow, which will be discussed in the next Chapter. I believe that the present research involving multiple emulsion formation based on kinetics analysis will shed new light on multi-phase microfluidic manipulation technology for wide applications.

5. Multi-component phase separation producing Janus droplet with hydrodynamics[1]

5.1. System definition and simulation setup

In this work, I apply the Cahn-Hilliard-Navier-Stokes model to simulate the formation process of Janus droplets via phase separation. This chapter is based on Ref. [68].

Janus droplets have been experimentally observed in polymer solutions consisting of polymer species A and B, and a solvent species (like water) with molecular weight much less than A and B [60]. A Janus particle usually has two distinct faces which are immiscible with each other as well as with the solvent-rich matrix. Each face of the Janus particle is composed of distinct polymer species [24]. The space and time dependent composition of polymer A, polymer B, and solvent is defined as $c_1(\mathbf{x},t)$, $c_2(\mathbf{x},t)$, and $c_3(\mathbf{x},t)$, respectively, and subjected to the constraint of the incompressible condition $\sum_{i=1}^{3} c_i = 1$. The Flory parameters χ_{ij} and χ_{ijk} are supposed to be temperature dependent as [69, 70]

$$\begin{aligned} \chi_{ij} &= a_{ij} + \frac{b_{ij}}{T}, \quad i < j, \\ \chi_{ijk} &= a_{ijk} + \frac{b_{ijk}}{T}, \quad i < j < k. \end{aligned} \tag{5.1}$$

The degree of polymerization N_i, the temperature coefficients for the Flory parameters a_{ij}, a_{ijk}, b_{ij}, b_{ijk} are chosen to be consistent with the following experimental observations: (i) When the temperature is greater than the critical temperature T_c, i.e., $T > T_c$, the polymer A and B are well miscible with each other and form a homogeneous droplet. The homogeneous droplet consisting of polymer A and B is immiscible with the solvent matrix, which is attributed to a relatively strong repulsive interaction between the solvent and the two polymer species. (ii) As $T < T_c$, the repulsive force between polymer A and B increases with a reduction in temperature. The enhanced repulsive force at low temperature leads to a miscibility gap involving polymer-A rich and polymer-B rich phases, which results in the phase separation inside the homogeneous droplets formed above the critical temperature. Such kind of features (i) and (ii) for the phase diagram can be found in the ternary system of hexane-perfluorohexane-water [60] and many other ternary polymer solutions. The parameters N_i, a_{ij}, b_{ij}, a_{ijk}, b_{ijk} for modeling the ternary phase diagram are tabulated in Table 5.1.

---

[1] Copyright notice: This chapter is licensed under a Creative Commons Attribution-Non Commercial 4.0 International License (CC BY-NC 4.0): https://creativecommons.org/licenses/by-nc/4.0/deed.en

Two typical phase diagrams at temperatures greater and less than T_c are shown in Fig. 5.1(I). The binodal and spinodal lines are depicted by the solid and dashed lines, respectively, in the contour plot for the bulk free energy density.

Parameters	Description	Value
N_1, N_2, N_3	Degree of polymerization	(5, 5, 1)
a_{12}, a_{13}, a_{23}, a_{123}	First Flory parameter coefficient	(−1.33, 0.0, 0.0, 5.0)
b_{12}, b_{13}, b_{23}, b_{123}	Second Flory parameter coefficient	(3.33, 4.2, 4.2, −8.0)

Table 5.1.: Free energy parameters of the ternary system for phase separations.

All the physical parameters are non-dimensionalized by the characteristic length $x^* = 2\times10^{-10}$ m, reference surface tension $\sigma^* = 1.0\times10^{-2}$ N/m, and diffusivity $D^* = 1\times10^{-9}$ m^2/s. The dimensionless quantities Re, We, and $P\acute{e}$ applied in the model are calculated as

$$Re = \frac{\rho^* u^* x^*}{\eta^*}, \quad We = \frac{\rho^* u^{*2} x^*}{\sigma^*}, \quad P\acute{e} = \frac{u^* x^*}{D^*}. \tag{5.2}$$

Since I am interested in phase separation coupled with fluid flow, the convection and diffusion processes become comparable. In other words, the relaxation time for thermodynamic process $(x^*)^2/D^*$ is in the same magnitude with hydrodynamics x^*/u^*, which gives rise to the Péclet number $P\acute{e} = u^* x^*/D^* = 1.0$. While Re and We vary respectively with the magnitude of the hydrodynamic effect.

In our work, the finite difference method and the explicit Euler scheme are implemented to solve the CHNS model with the equidistant Cartesian mesh. Periodic boundary conditions are applied for the composition and the fluid velocity.

5.2. Results and discussion

5.2.1. The formation of Janus droplet

In the following discussions, I consider the scenario where the phase separation via diffusion process dominates the Janus droplet formation and the weak convection can be neglected as reported [15]. Initially, at the temperature $T = 1.05T_c$, a homogeneous solution of polymer A and B is dissolved in the abundant solvent ($c_1 : c_2 : c_3 = 15 : 15 : 70$). The initial composition of the ternary polymer solution is marked by the triangle symbol in Fig. 5.1(I). As shown in the phase diagram, this initial composition locates between the black dashed lines, i.e., inside the spinodal region. A Gaussian white noise with amplitude $A_\xi = 0.1$ for the diffusion flux of all components, as depicted by Eq. (2.18), is used to model the composition fluctuation. Triggered by the composition fluctuation, phase separation begins and polymer-rich droplets (light green) start to form and grow from the solvent-rich matrix (dark purple), as illustrated in Fig. 5.1(II)(i). With time, these droplets coarsen with each other dominating by the Ostwald ripening effect due to their radius difference. Meanwhile, the coalescence of relatively large droplets is observed as highlighted by the dashed square. Consequently, dispersed droplets with various sizes are obtained. The

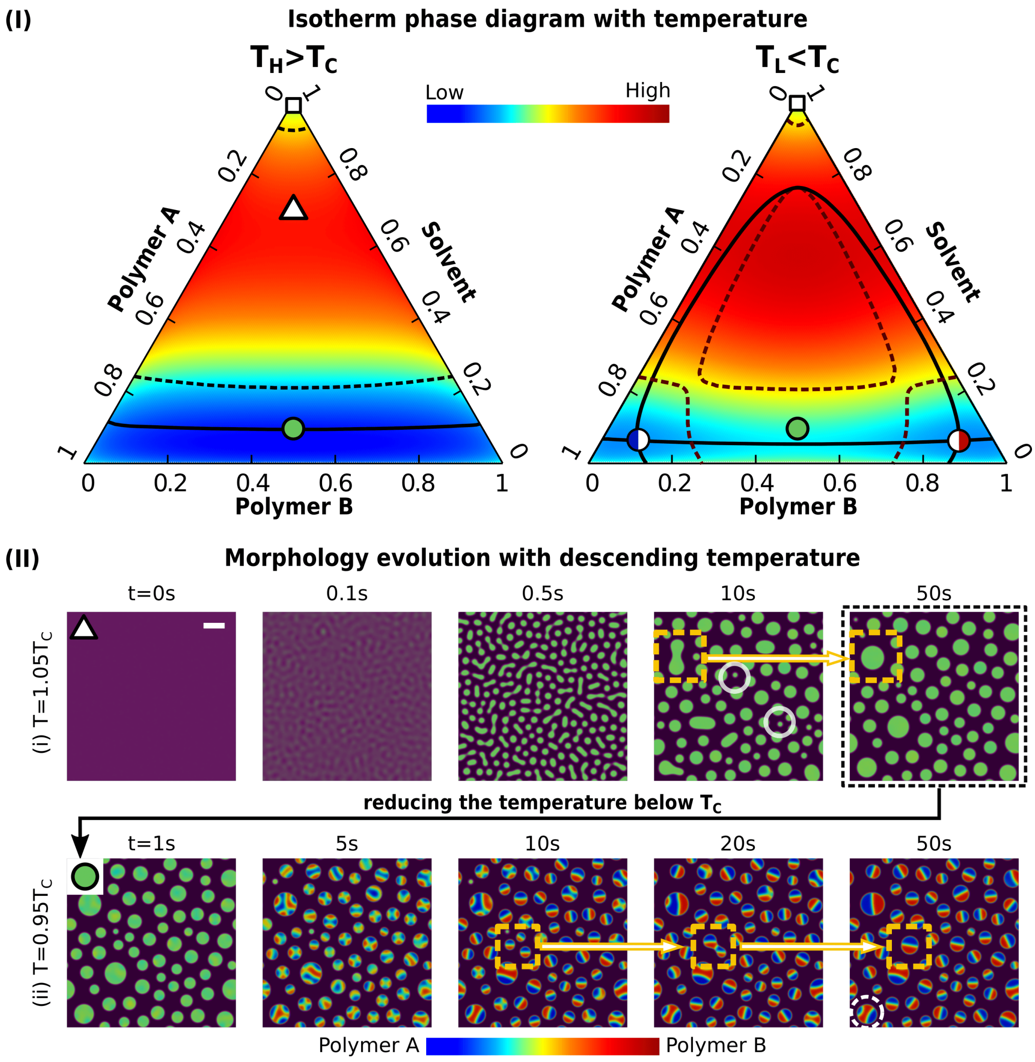

Figure 5.1.: (I) Left: the ternary phase diagram of the polymer A-polymer B-solvent system at $T = T_H$ ($T_H = 1.05T_c$). The magnitude of the free energy density is described by the heat map (red: high; blue: low). The binodal and spinodal compositions are depicted by the dark red solid lines and dashed lines, respectively. The white triangle indicates the initial compositions with $c_1 = c_2 = 0.15$. The equilibrium compositions of droplet and matrix are labelled with the green circle and the white square, respectively. Right: the phase diagram at $T = T_L$ ($T_L = 0.95\,T_c$). The green circle corresponds to the initial homogeneous composition in the droplet resulting from the phase separation at $T = T_H$. The Janus symbols mark the equilibrium compositions in each Janus hemispheres. (II) Upper row: the microstructure evolution for the production of homogeneous polymer droplets at $T = T_H$. Lower row: the formation of Janus particles via spinodal decomposition when reducing the temperature to $T = T_L$. The simulation domain size is 400 μm × 400 μm. In this work, all the white scale bars denote 50 μm and each color bar scales the polymer composition, if not specified.

equilibrium composition in the droplets is marked by the green circle on the binodal line in the left phase diagram. Since at $T > T_c$ polymer A and B are miscible with each other, Janus particle is not observed at this temperature. As demonstrated in the following section, the droplet with miscible polymer A and B formed at $T > T_c$ is the precursor for the formation of the Janus droplet.

Next, I reduce the temperature till $T = 0.95\,T_c$, where the miscibility gap between two polymer species begins to appear which results in the spinodal decomposition inside the precursor polymer droplet. To simulate the Janus droplet formation and to ensure a stable three phase region, I assign the following interfacial tension parameters $\sigma_1 = \sigma_2 = 0.64$, $\sigma_3 = 3.6$. As presented in the snapshots of Fig. 5.1(II)(ii), at $t = 5$ s, two polymer species get separated to form a polymer A-rich region (blue) and a polymer B-rich region (red). These two regions are divided by the light green interfaces. Accompanied by the proceeding spinodal decomposition, the interfaces between the blue and the red regions are stabilized (see the snapshot at $t = 10$ s). Decided by the wetting effect at the triple junction involving polymer A-rich phase, polymer B-rich phase, and the solvent-rich phase, Janus droplets with $r \lessapprox 15\,\mu$m are generated at $t = 10$ s. Afterwards, the phase separation subsides and the minimization of free energy functional is mainly manifested by the reduction in the interfacial energy. Then, the Ostwald ripening effect and coalescence come on to the stage. For instance, the tiny droplet in the white circle vanishes, because of its huge curvature difference from its surrounding large droplets. As highlighted by the orange dashed squares of Fig. 5.1(II)(ii), three tiny Janus droplets coalesce into a large one due to their relatively narrow distances. Moreover, a large Janus droplet with a transient hamburger structure [71, 72] is captured in the white-dashed circle at $t = 50$ s. This observation indicates that the size of the precursor polymer droplet plays an important role on the morphological evolution of the Janus droplet, which will be discussed in the following parts.

5.2.2. Radius and initial composition

In the manufacturing process of Janus particles, the final product with different sizes can be achieved by controlling the holding time at $T = 1.05\,T_c$ above the critical temperature. As shown in section 5.2.1, the Ostwald ripening effect together with the droplet coalescence results in precursor droplets with various sizes. However, with the descending temperature, the phase separation of polymer A and B cannot simultaneously engender perfect Janus droplet for different sized precursor droplets. In order to have a heedful look at this size effect, I place three precursor droplets with initial radius $r_0 = 20,\ 40,\ 80\,\mu$m in the solvent-rich matrix and reduce the temperature to $T = 0.95\,T_c$. As shown in Fig. 5.2, the smallest droplet with $r_0 = 20\,\mu$m forms a perfect Janus at 50 s, while the largest precursor droplet with $r_0 = 80\,\mu$m spends 20 times longer for the transformation into a perfect Janus particle. The reason for this size effect can be explained by viewing the intermediate stage of the Janus droplet development.

As depicted in Fig. 5.2, more complex bi-continuous structures are produced inside the relatively large droplets by phase separation. The final perfect Janus droplet is formed via the coalescence of the tortuous bi-continuous structure. As demonstrated in the third snapshot of Fig. 5.2, for all the three phases, namely, the blue-highlighted polymer

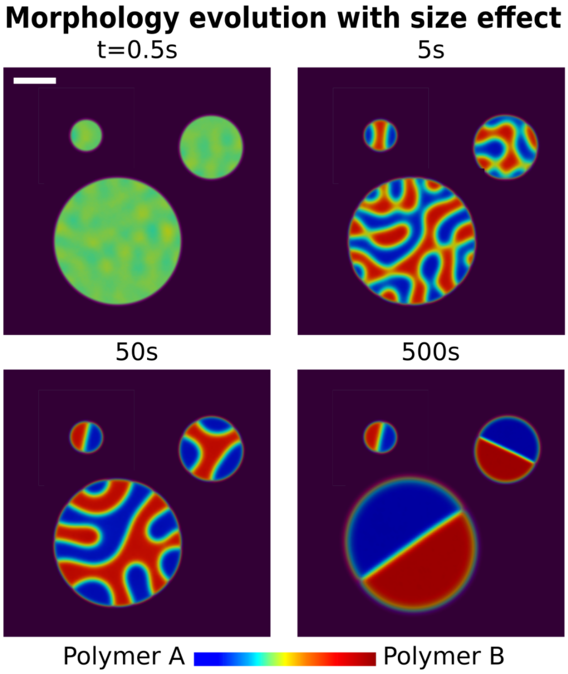

Figure 5.2.: The Janus droplet formation with 3 initial radii: 20, 40, and 80 μm. In simulations, all droplets are placed in their individual domains and are stitched in a domain for a better comparison.

A-rich phase, the red-colored polymer B dense phase, and the matrix, the equilibrium compositions are reached. Hence, at this stage, the phase separation plays hardly any role now and the Ostwald ripening is the main mechanism for the Janus droplet evolution. According to the classic theory of the Ostwald ripening [73, 74, 75], the mean average radius of the phase separation structure follows the quintessential LSW (Lifshitz-Slyozov-Wagner) power law $\bar{r} \sim t^{1/3}$. Therefore, the transformation of the droplet with $r_0 = 80\,\mu$m into a Janus shape takes about 4^3 times longer than the tiny one with $r_0 = 20\,\mu$m.

In some experiments [77, 63, 76, 78], non-equal compositions of polymer A and B are adopted to synthesize different droplet morphologies, e.g. vesicle, uneven Janus, etc. In Fig. 5.3(I), I perform simulations with unequal polymer compositions, namely $c_1 : c_2 = 3 : 7$ and $c_1 : c_2 = 7 : 3$, for a precursor droplet with $r_0 = 80\,\mu$m. Since the composition ratio between the two polymers is off $5 : 5$, in lieu of bi-continuous structures, sub-droplets are engendered inside the precursor droplet via the spinodal decomposition. To minimize the interfacial energy, those sub-droplets merge into a joint phase. This routine for the Janus droplet formation is in good agreement with the confocal microscopy images for the dextran-PEG-water system, as illustrated in Fig. 5.3(II). It is also noteworthy that the interface between Polymer A and B in our simulation ($7 : 3$ in Fig. 5.3(I)) has the different convexity from the experiment (PEG riched case in Fig. 5.3(II)). As the analyse in Ref. 33 , the Janus structure is extremely sensitive to the composition dependent interfacial tension parameters σ_i. Thus, the slight polymer composition changes can result in the huge difference in the interface convexity.

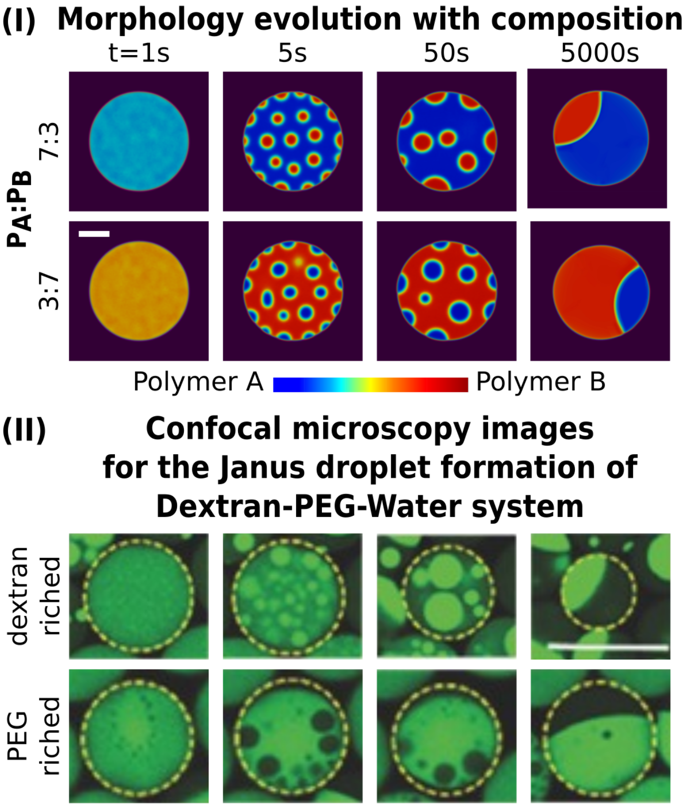
(I) Morphology evolution with composition
t=1s
5s
50s
5000s
PA:PB
7:3
3:7
Polymer A
Polymer B
(II) Confocal microscopy images for the Janus droplet formation of Dextran-PEG-Water system
dextran riched
PEG riched

Figure 5.3.: (I) The morphological evolution via sub-droplet coalescence by unequal initial polymer A & B composition ratios; upper panel: polymer A:B = 3:7; lower panel: polymer A:B = 7:3. The initial droplet size is 80 μm. (II) The confocal microscopy images of Janus particle formation by the sub-droplet coalescence in the dextran-PEG (green dyed)-Water system. Reproduced with permission from Ref. [76], copyright 2016 WILEY-VCH Verlag GmbH & Co. KGaA, Weinheim.

5.2.3. Interfacial tension

In the previous part, I elucidate the formation of Janus droplet via liquid-liquid phase separation which transforms the bulk free energy of mixture into the interfacial energy. The latter one determines the pattern of the microstructure around the triple junction. In this section, I address the microstructure pattern at the region of the triple junction by varying the interfacial tension. In experiments, the adjustment of interfacial tensions is achieved by adding various surfactant into the system [60]. As a rule of thumb, the surfactant quantity less than $0.1\%v/v$ has a minor effect on altering the ternary phase diagram [15]. In our simulations, the effect of specific surfactants can be mimicked by changing the interfacial tension parameter σ_i. To be consistent with the sharp interface model, the interfacial tension between the component A-rich phase and the component B-rich phase in the Cahn-Hilliard approach (see the right column of Fig. 5.4(I)) is calculated as

$$\sigma_{\alpha\beta} = \int \frac{\sigma^*}{\epsilon} \Delta f(c_1, c_2, c_3) + \sum_{i=1}^{3} \sigma_i \, \epsilon \, (\nabla c_i)^2 \, d\mathbf{s}, \tag{5.3}$$

where $\mathbf{s}$ delineates the integral routine which follows the energy minimum principle. As displayed by the solid arc with white open arrow in Fig. 5.4(I), the integration starts from the white open dot with one bulk equilibrium composition $(c_1^{eq}, c_2^{eq}, c_3^{eq})$ inside the phase α to the other bulk equilibrium composition $(c_1^{eq*}, c_2^{eq*}, c_3^{eq*})$ inside the phase β. The term Δf is defined as

$$\Delta f = f(c_1, c_2, c_3) - f(c_1^{eq}, c_2^{eq}, c_3^{eq}) - \sum_{i=1}^{3} \mu_i^{eq}(c_i - c_i^{eq}), \tag{5.4}$$

which measures the excess free energy density referring to the equilibrium state with the formulation as $f(c_1^{eq}, c_2^{eq}, c_3^{eq}) + \sum_{i=1}^{3} \mu_i^{eq} c_i^{eq}$. From this expression, the interfacial tension of the system is not only decided by the interfacial tension parameters σ_i, but also relies on the bulk free energy density of the mixture. Owing to adding the third component (C in this example), the integral routine at the equilibrium state does not take the dot-dashed straight line from α to β in the phase diagram, but follows the deterministic path which corresponds to the fundamental energy minimization principle as addressed by the Cahn-Hilliard equation, Eq. (2.4). In this way, the interfacial tensions in the ternary system can deviate largely from the one in the binary system, crucially depending on the Flory parameters χ_{ij} and χ_{123}. It appears that the addition of the third component dramatically increases the complexity for measuring and calculating the interfacial tension. In most cases, there is a paucity of experimental data for the interfacial tensions to validate the model. Here, I systematically discuss the effect of the interfacial tension on the pattern formation of the Janus particles.

Firstly, I analyse the interfacial tension parameters σ_i affecting the formation of the Janus droplet. The interface tension parameters σ_1 and σ_2 both vary from 0.2 to 4.2, while all other parameters are the same as that in section 5.2.2. This setup can be comprehended as introducing a tiny amount of surfactant which can drastically reduce the interfacial tension of the system, while the phase diagram is not altered. As displayed in Fig. 5.4(II), an increase in σ_1 and σ_2 results in different morphological evolution during the phase

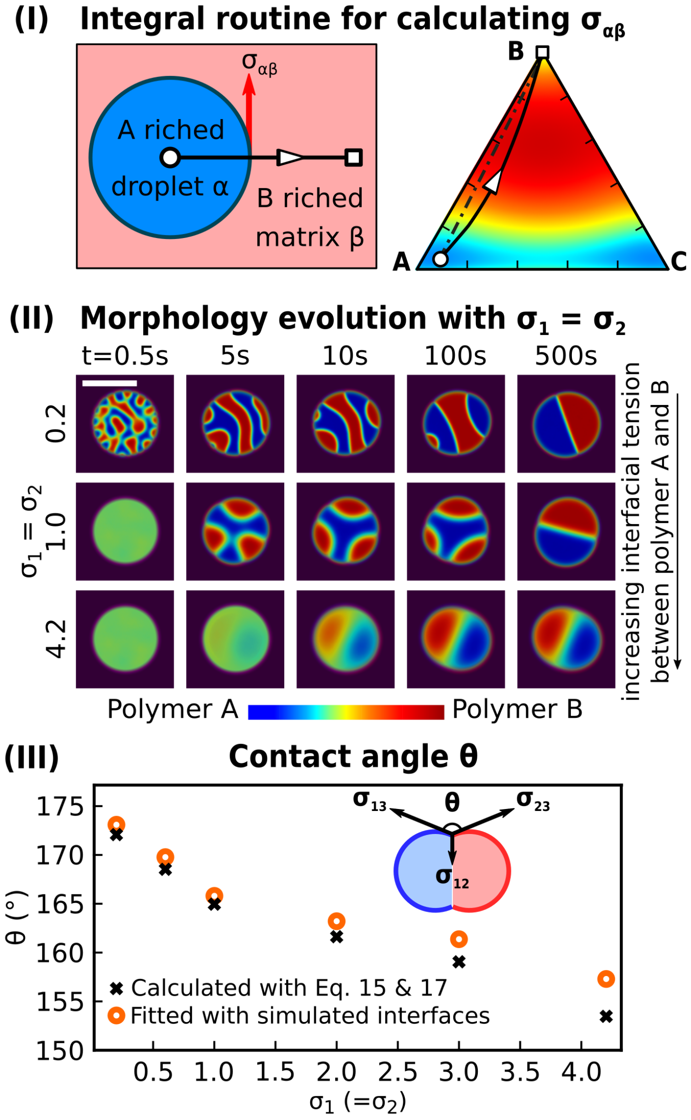

Figure 5.4.: (I) Left: the equilibrium interfacial tension $\sigma_{\alpha\beta}$ of the A-rich droplet α and B-rich matrix β with the sharp interface model. Right: the schematic integral routine with black open arrow on the phase diagram for the calculation of $\sigma_{\alpha\beta}$ in the Cahn-Hilliard model. (II) The formation of Janus particle via the spinodal decomposition with increasing interfacial tension parameters $\sigma_1 = \sigma_2$. The initial droplet sizes are 20 μm. (III) The contact angle θ between two hemispheres versus $\sigma_1 = \sigma_2$. Black cross: calculated with Eq. (5.5); orange open dot: fitted with simulation.

separation. For instance, the 3-fold symmetric droplet is observed in the setup with $\sigma_1 = \sigma_2 = 1.0$ which shows high similarities with the experimental observations for the patchy droplet structures of self-assembly materials [79]. With an increase in σ_1 and σ_2, the time expense for the formation of Janus droplet via the Ostwald ripening is sharply reduced and the final contour of the Janus droplet transforms from a joint sphere to a quasi-ellipse. In Fig. 5.4(III), the contact angles θ between two Janus hemispheres are measured with two different methods. 1) Orange open dots: the interfaces between the Janus hemispheres and the solvent matrix are extracted from the simulation by the criterion: $c_1 = 0.5$ for the polymer A hemisphere and $c_2 = 0.5$ for polymer B. As sketched by the inset in Fig. 5.4(III), I fit the interfaces between polymer A-rich hemisphere and solvent matrix and between polymer B-rich hemisphere and solvent matrix with circles. The interfaces intersect at the triple junction where the contact angle θ is computed by the included angle of the two tangent lines of the fitted circles. 2) Black crosses: with Eq. (5.3), the three interfacial tensions form the so-called Neumann triangle relation which constrains the θ at equilibrium as

$$\cos\theta = \frac{\sigma_{12}^2 - \sigma_{13}^2 - \sigma_{23}^2}{2\,\sigma_{13}\,\sigma_{23}}. \tag{5.5}$$

Showing good agreement in these two methods, the contact angle θ decreases with enlarging the interfacial tension parameters σ_1 ($= \sigma_2$). The comparison not only indicates the droplet contour changing from Janus ($\theta \sim 180°$) to quasi-dumbbell structure ($\theta \sim 155°$) controlled by the interfacial tension, but also validates the Cahn-Hilliard model for the Janus droplet system.

Secondly, I assign different Flory parameters χ_{12} with the same interfacial tension parameters $\sigma_1 = \sigma_2 = 1.0$ in the simulation. This setup may be achieved by applying different polymer species in the system. As demonstrated in the free energy landscapes in Fig. 5.5(I), an increase in χ_{12} not only modifies the interfacial tension between polymer A and B, but also broadens the miscibility gap as depicted by the light red shadow regions. Thence, more pronounced phase separation accelerating the production of polymer A/B interfaces is expected for a larger value of χ_{12}, as demonstrated in Fig. 5.5(II). Most interestingly, in the blue highlighted simulation snapshots of Fig.5.5(II), intermediate droplets with polygon and triangle shapes are observed. This observation implies that the thermally induced liquid-liquid phase separation may have the potential to synthesize droplets with some special morphologies, which shall be investigated in the future.

5.2.4. Asymmetric phase separation

In the previous sections, the Flory parameters χ_{13} and χ_{23} are assumed to be the same, so do the interfacial tension parameters $\sigma_1 = \sigma_2$. These setups usually give rise to symmetrical kinetics for the formation of the Janus droplet, i.e., different faces of the Janus droplet and the diffusion path of distinct polymer species following identical kinetics. Actually, in most real systems, the Flory parameters of polymer A and polymer B with the solvent are not equal, e.g., $\chi_{13} \neq \chi_{23}$, denoting different attractive/repulsive potential of the polymer species with the solvent molecules. In addition, the interfacial tensions between polymer

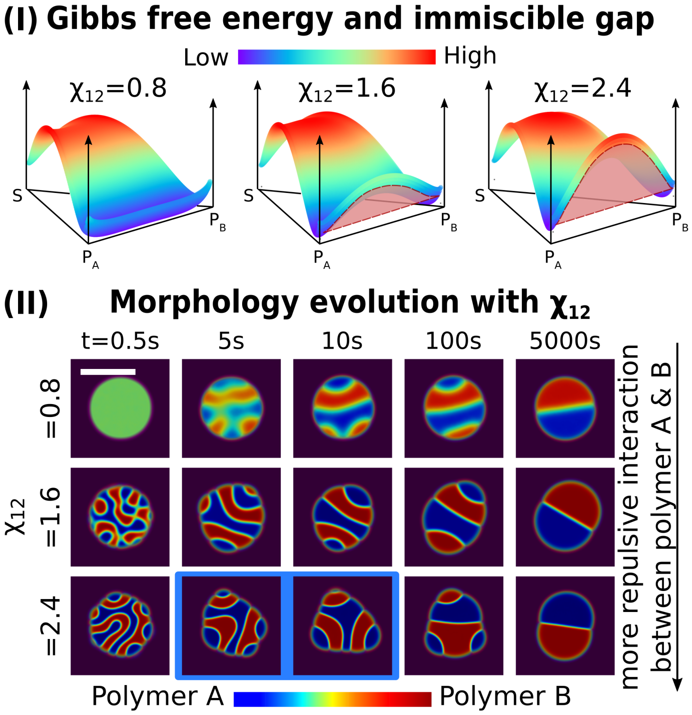

Figure 5.5.: (I) The free energy density at $T = 0.95\,T_c$ for different Flory parameters χ_{12} between polymer A and polymer B. The light red shadow regions mark the miscibility gaps. (II) The formation of the Janus droplet with the enhancing χ_{12}. The blue highlighted snapshots display the transient pentagon and triangle droplet shapes. The initial droplet sizes are 20 μm.

species and solvent should be distinct from each other, which may be caused by unequal interfacial tension parameters, $\sigma_1 \neq \sigma_2$. The Janus droplet formation is attributed to the interplay of both liquid-liquid phase separation and the interfacial energy minimization, the kinetics of which is both essentially affected by the Flory parameters as well as the interfacial tension parameters. Thus, the distinguishing properties of polymer A and B may lead to asymmetrical kinetics for the microstructure evolution of the Janus droplet formation as well as dissymmetric diffusion path, which will be discussed in this section.

To elucidate the symmetric kinetics, I place one homogeneous droplet with $r_0 = 30\ \mu$m and initial composition $c_1 = c_2 = 0.47$ inside the polymer lean matrix ($c_1 = c_2 = 0.00025$). In this setup, I adopt the same interfacial tension and Flory parameters for polymer A and B, i.e., $\sigma_1 = \sigma_2 = 0.6$ and $\chi_{13} = \chi_{23} = 4.2$. From Eq. (5.3), I have $\sigma_{13} = \sigma_{23}$. Triggered by the composition fluctuation, the phase separation generates a polymer A-rich region (blue colored) and a polymer B-rich region (red colored), which comprise of the bi-continuous structure resulting from the spinodal decomposition, as displayed in Fig. 5.6(I)(ii). The kinetics of the Janus droplet formation is characterized by tracing the maximal polymer A composition c_1 (turquoise line) and the maximal polymer B composition c_2 (red line) starting from the green circle on the phase diagram. As can be noticed in Fig. 5.6(I)(i), once the polymer A-rich blue region forms, the turquoise trajectory of the maximal c_1 falls exactly on the black solid binodal line. This overlap implies that there exist a series of transient pseudo-binary equilibrium states between the polymer A-dense blue region and the polymer lean solvent matrix (black open square). One typical exemplary pseudo-binary equilibrium is shown by the blue dot-dashed tie line. This kind of pseudo-binary equilibrium is unstable over time because of the presence of the adjacent polymer B-rich red region, which is not in equilibrium with the polymer A-dense region. Driven by the free energy minimization, the immiscible polymer A in the adjoining red region is rejected. For the low solubility of polymers in the solvent matrix, phase separation induced mass transformation via the surrounding matrix is in vain. The precipitated polymer A from the red region can only diffuse across the A-B interface, resulting in an enrichment of polymer A in the blue colored regions. Consequently, the maximal composition c_1 continuously moves leftwards along the binodal line, and finally reaches the ternary equilibrium composition labelled by the blue Janus symbol on the phase diagram in Fig. 5.6(I)(i). At this right stage, a perfect Janus droplet is completely formed. The same kinetics happens inside the polymer B region, because of the exactly equal interfacial tension and Flory parameters of polymer B and A. As depicted in Fig. 5.6(I)(iii), I observe the same tendencies of the maximal polymer A composition (blue solid line) and maximal polymer B composition (red solid line) changing with time. The small ups and downs are in line with the coarsening and coalescence of the phases which change the curvature and consequently the composition. In this way, I denominate this kind of kinetics as “symmetric” which denotes the identical kinetic pathways for polymer A and B.

In our second simulation, I set the interfacial tension parameters to be asymmetric for polymer A and B as $\sigma_1 = 1.0$, $\sigma_2 = 0.6$. The Flory parameters are $\chi_{13} = \chi_{23} = 4.2$, as the one in Fig. 5.6(I)(i). With Eq. (5.3), it can be shown that the interfacial tension between polymer B-rich phase and solvent-rich phase σ_{23} is smaller than that between polymer A-rich phase and solvent-rich phase σ_{13}. Hence, at the very beginning of the phase separation, in

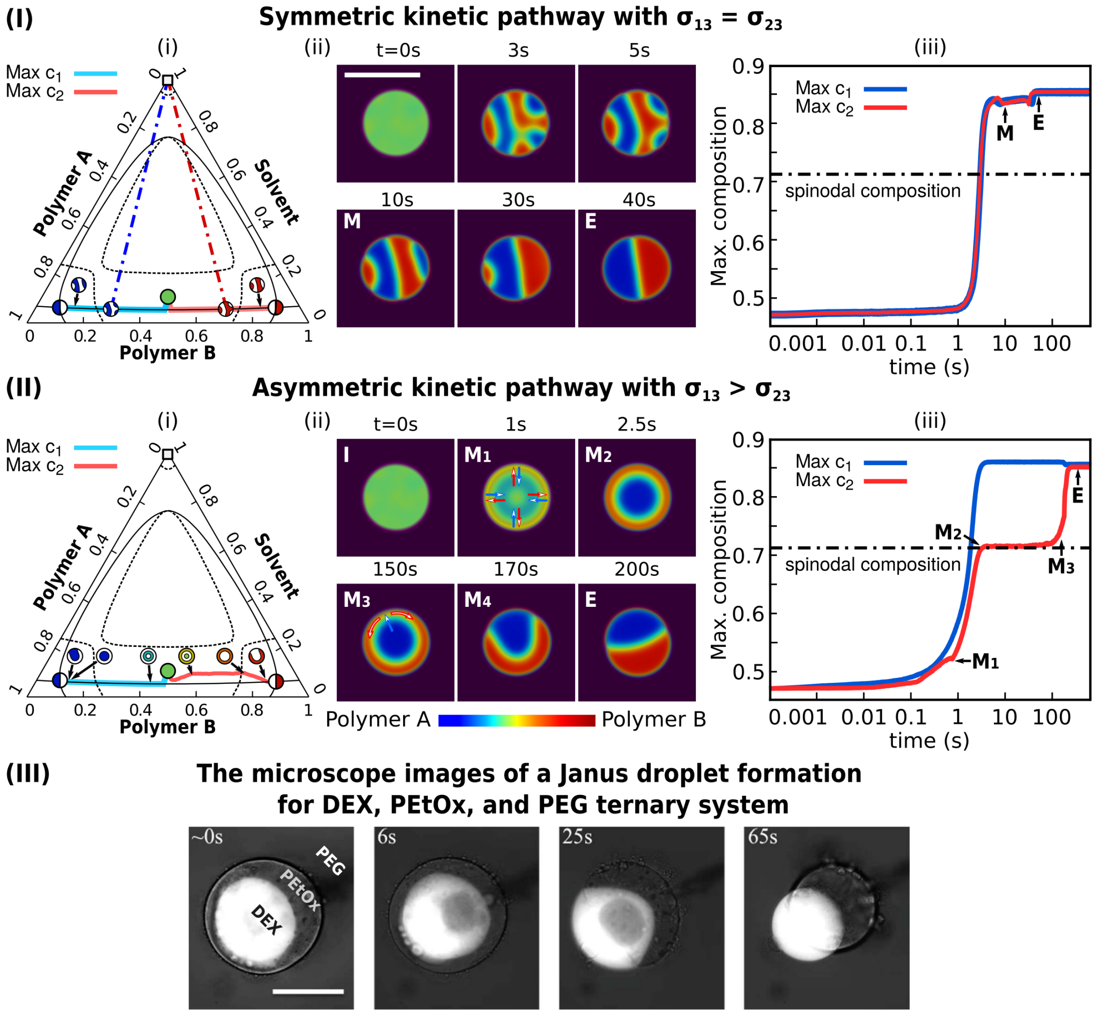

Figure 5.6.: (I) The symmetric kinetics of the Janus droplet formation with the same interfacial tensions $\sigma_{13} = \sigma_{23}$. (i) The kinetic pathway of the maximal polymer A rich region (turquoise solid line) and the maximal polymer B rich region (red solid line) on the phase diagram. The dot-dashed lines indicate the tie lines for the pseudo-binary equilibrium between polymer droplets and solvent matrix; (ii) the Janus droplet formation with initial droplet size $r_0 = 20\,\mu$m; (iii) the time sequence of the composition with maximal c_1/c_2 (blue/red solid line). The dot-dashed horizontal line indicates the spinodal composition. (II) The asymmetric kinetics of the Janus droplet formation with unequal interfacial tensions $\sigma_{13} > \sigma_{23}$. The initial droplet size is $20\,\mu$m. (III) The microscopy images of Janus particle formation via the asymmetric phase separation in a three phase system. Bright: dextran (DEX); grey: poly(2-ethyl-2-oxazoline) (PEtOx), and grey matrix: polyethylene glycol (PEG). Reproduced with permission from Ref. [78], copyright 2021, American Chemical Society.

order to reduce the interfacial energy, the polymer B prefers to contact with the solvent matrix and encircles polymer A to prevent the formation of the interface between polymer A and solvent matrix. Such a kinetic process leads to centrosymmetric diffusion fluxes of polymer A and B. Accordingly, an intermediate core-shell morphology is established, which has been observed in many micro-capsule systems [80, 81, 82, 62, 83]. As shown in Fig. 5.6(II)(i) for the kinetic pathway on the phase diagram, the core-shell morphology is accompanied by a deviation of the red trajectory (the maximal c_2) from the black solid binodal line. This deviation is explained as follows. From the intermediate state M_1 to M_2, due to spinodal decomposition, the blue polymer A-rich core forms and quickly reaches the equilibrium composition on the binodal line. But in the shell region, the kinetics is totally different. Since both polymer A-rich phase and the solvent matrix contact with the shell, there exist two interfaces, namely, the polymer A-B interface and the polymer B-solvent interface. The composition in the shell region evolves not only via the phase separation with respect to the polymer-A rich core but also the binodal decomposition pertaining to the solvent matrix. The non-equal diffusion fluxes at the core-shell interface via spinodal decomposition and at the shell-solvent interface via binodal decomposition give rise to the deviation of the maximal c_2 trajectory from the binodal line in the polymer B-rich region.

In Fig. 5.6(II) between the time points M_2 and M_3 , the maximal c_2 hardly increases with time and the core-shell structure stagnates. The reason for this utterly slow morphological transformation can be explained by the kinetic pathway on the phase diagram in Fig. 5.6(II)(i). At M_2, the red trajectory passes through the black dotted spinodal line and the composition in the shell falls outside the spinodal region. Thereafter, the microstructure evolution is dominated by the binodal decomposition instead of spinodal decomposition. Since the former one is much slower than the latter one, the composition c_2 in the shell region increases with time at a relatively slow rate, leading to a stagnation state from M_2 and M_3. Noteworthily, the core-shell structure is not the energy minimal state. In the shell region, the everlasting Gaussian composition fluctuation gives rise to small composition gradients and produces a circular diffusion for the polymer B component, leading to the breakup of the core-shell structure at M_4. When the core-shell structure collapses, the interfacial tension rapidly reshapes the polymer B-rich layer into a hemisphere (at E) which is the final equilibrium state of the system. I name the observation in this setup as “asymmetric kinetics” to make the distinction from the previous “symmetric” case, which has also been studied in many experiments [77, 63, 78], as the microscopic images shown in Fig. 5.6(III).

5.2.5. Fluid dynamics

In the previous sections 5.2.1-5.2.4, I considered the Janus droplet formation via diffusion controlled phase separation process and observed a stagnation stage for the intermediate core-shell microstructure in the formation process of the Janus droplet. In this section, I will shed light on the effect of hydrodynamics on the morphological evolution of the Janus particle as well as the core-shell microstructure. Considering the kinetics of the polymeric phase separation, the polymer diffusivity can vary from 10^{-9} m^2/s to 10^{-12} m^2/s which is decided by the degree of polymerization, temperature, solvent property, and so on. Thus, when the polymer system becomes semi-dilute, or even dense, the diffusivity of polymer chains decreases drastically. When D^* drops to the order of $10^{-12}\,\mathrm{m^2/s}$, the hydrodynamic effect plays a non negligible role compared with diffusion. As written in Eq. (2.20), the composition gradient ∇c_i in the inhomogeneous fluid system can propel the fluid flow via the capillary tensor term Θ in the Navier-Stokes (NS) equations Eq. (2.18). This mechanism is called the Marangoni effect. By adjusting the dimensionless numbers, 1) Weber number: We and 2) Reynolds number: Re, in the nondimensionalized NS equation Eq. (2.18), I will show distinct hydrodynamic behaviors for the microstructure evolution of the Janus droplet.

In a first setup, I perform a single droplet simulation with the asymmetric interfacial tension $\sigma_{13} > \sigma_{23}$ as the previous section 5.2.4. To couple the hydrodynamic effect with the phase separation, the Weber number We and Reynolds number Re are both set as 1. As can be noticed in both the morphological evolution and the kinetic pathway in Fig. 5.7, the transient core-shell structure survives 10 times shorter than the simulation without the hydrodynamics shown in Fig. 5.6. By viewing the pressure distribution around the droplet in Fig. 5.7(I)(ii), the pressure has its maximum (dark red colored) in the polymer B dense shell region, the minimum inside the solvent matrix, and the intermediate value (yellowish) in the polymer A-rich core. Here, the pressure is induced by the surface tension force subjected to the incompressible condition. In order to reduce the surface energy, the convection resulting from the pressure difference on both sides of the shell structure together with the diffusion leads to the breakup of the shell, which is faster than the morphological transformation solely via diffusion. The stagnation period of the core-shell structure around the spinodal composition only lasts several seconds in this case.

The Marangoni flow has two origins: i) phase separation driving force. During the phase separation process, the composition has not yet reached the equilibrium value, where excess free energy density of mixture results in the surface tension force $\nabla \cdot \Theta$ in the N-S equation. As demonstrated in Eq. (2.23), the term $\nabla \cdot \Theta$ is proportional to the chemical potential gradients which can not be balanced by the pressure p around the droplet. Consequently, the convection takes place. ii) The minimization of the interfacial energy. The phase separation leads to the creation of new interfaces. The non-uniform curvature along the interface as well as the surface tension force enforcing the Young's contact angle at the triple junction also gives rise to a convection. The former one occurs at the early stage of the phase separation. The latter one appears once new interfaces are established and dominates the evolution when the bulk composition reaches the equilibrium value. It is noteworthy that both mechanisms also exist when the Janus droplets are produced by the phase separation via solely diffusion (see Fig. 5.1). The main difference is the way how the energy is minimized, or more suffice to say, the energy dissipation associated with different kinetics. When the hydrodynamics is coupled, the excess free energy and surface energy can be transformed into the kinetic energy of the fluid flow. As displayed in Fig. 5.7(I)(iii), the fluid velocity around the droplet increases simultaneously with the proceeding spinodal decomposition. After reaching the equilibrium composition and the breakup, the non-uniform curvature and the free energy minimization at the triple junction lead to a further increase in the fluid velocity. When the curvature becomes uniform around the Janus droplet and the contact angle at the triple junction reaches the

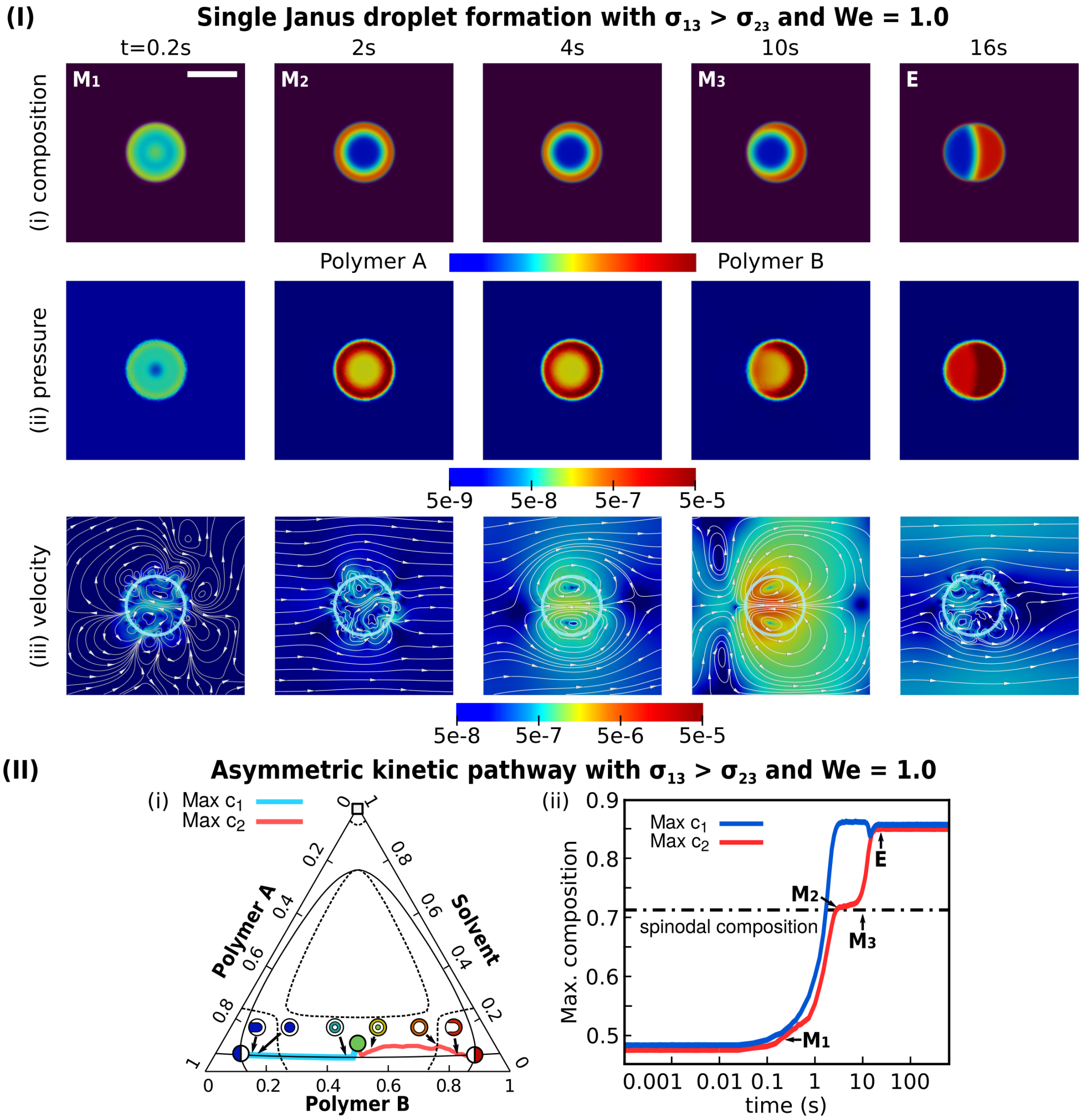

Figure 5.7.: (I) The single Janus droplet formation with asymmetric interfacial tensions $\sigma_{13} > \sigma_{23}$ and the hydrodynamic effect $We = 1.0$. The initial droplet size is 20 μm. (i) Composition field; (ii) pressure distribution; (iii) velocity field and the stream lines. The white translucent circles mark the Janus droplet interface with solvent composition $c_3 = 0.5$. Each color bar beneath shows the respective magnitude. (II) The asymmetric kinetics of the Janus droplet with the hydrodynamic effect ($We = 1.0$) and unequal interfacial tension $\sigma_{13} > \sigma_{23}$. (i) The kinetic pathway of the maximal polymer A/B dense region (turquoise/red solid line) on the phase diagram. (ii) The time sequence of the composition with maximal c_1/c_2 (blue/red solid line).

equilibrium value, the fluid flow dissipates and tends to vanish, as shown in Fig. 5.7(I) at $t = 16\,\mathrm{s}$.

Next, I simulate the Janus droplet formation via a two-step phase separation. At step (i), homogeneous polymer droplets are produced at $T = 1.05\ T_c$. At step (ii), the temperature is reduced to $T = 0.95\ T_c$, where Janus droplets are formed. Here, two magnitudes of the hydrodynamic effect are considered, namely, $We = 1$ and 0.01, to elucidate its influence on the multi-droplet system. By the definition of the Weber number, a large We indicates a strong capillary effect. By comparing the morphological evolution in Fig. 5.8 with the previous case only with diffusion (Fig. 5.1), the phase separation process is magnificently accelerated. For the phase separations at high temperature $T = 1.05\ T_c$, it always takes less time t_e for the droplet to reach its equilibrium concentration when the hydrodynamic effect becomes more pronounced. For $We = \infty$ (diffusion only), $t_e = 8.5\,\mathrm{s}$; $We = 1.0$, $t_e = 2.0\,\mathrm{s}$; $We = 0.01$, $t_e = 0.5\,\mathrm{s}$. As $T = 0.95\ T_c$, concerning the size effect discussed in section 5.2.2, droplets with similar sizes are compared. The Janus droplet production also becomes quicker with the stronger convection. For $We = \infty$, $t_e = 30.0\,\mathrm{s}$; $We = 1.0$, $t_e = 18.0\,\mathrm{s}$; $We = 0.01$, $t_e = 2.25\,\mathrm{s}$.

Also, the size distribution of the Janus droplet becomes more dispersed with the enhancing hydrodynamic effect. The underlying mechanism can be elucidated with the Tanaka-Golovin theory [20] that has two important contributions to the polydispersity of the Janus droplet. On the one hand, the hydrodynamic force is produced by the overlap of the diffusion potential and propels the droplet coalescence. Hence, the droplets with relatively small distances apart are prone to impinge with each other, forming a large droplet as illustrated in the gold dashed squares of Fig. 5.8. On the other hand, the hydrodynamics can act as a supporter for the tiny droplet and curtails the consumption of small droplet by its large peers because of the competitive fluxes of diffusion and convection (see the discussion in Ref. [26, 19]). The distinct life time of the mini-droplets circled in Fig. 5.1 and 5.8 confirms the supporting effect of hydrodynamics. The pronounced coalescence effect for large droplets and the shielding effect for the small droplets result in the polydispersity of Janus droplet. This observation is also consistent with the theoretical derivation [84]. In addition, since both the phase separation and the fluid mechanics are considered in our model, the Janus production via microfluidic process can also be simulated and will be discussed in future works.

Finally, I simulate the Janus droplet formation where the surface tensions of polymer A and B are identical. As shown in Fig. 5.9, the perfect Janus droplets with symmetric hemispheres of A and B are produced. Similar to the previous simulations with unequal surface tensions (Fig. 5.8), the Janus sizes increases with the increasing hydrodynamic effect. The size distribution also turns to be more dispersed with enhancing convection inside the system, which is attributed to the two reasons discussed in the previous paragraph: (i) the imbalanced surface tension force $\nabla \cdot \Theta$ induces convection which propels the droplet coalescence; (ii) the strong Marangoni flow also acts as a counter-force that curtails the diffusion process. Under this circumstance, the LSW mechanism plays only a subordinate role and the mean radius does not obey the $1/3$ scaling law anymore [20].

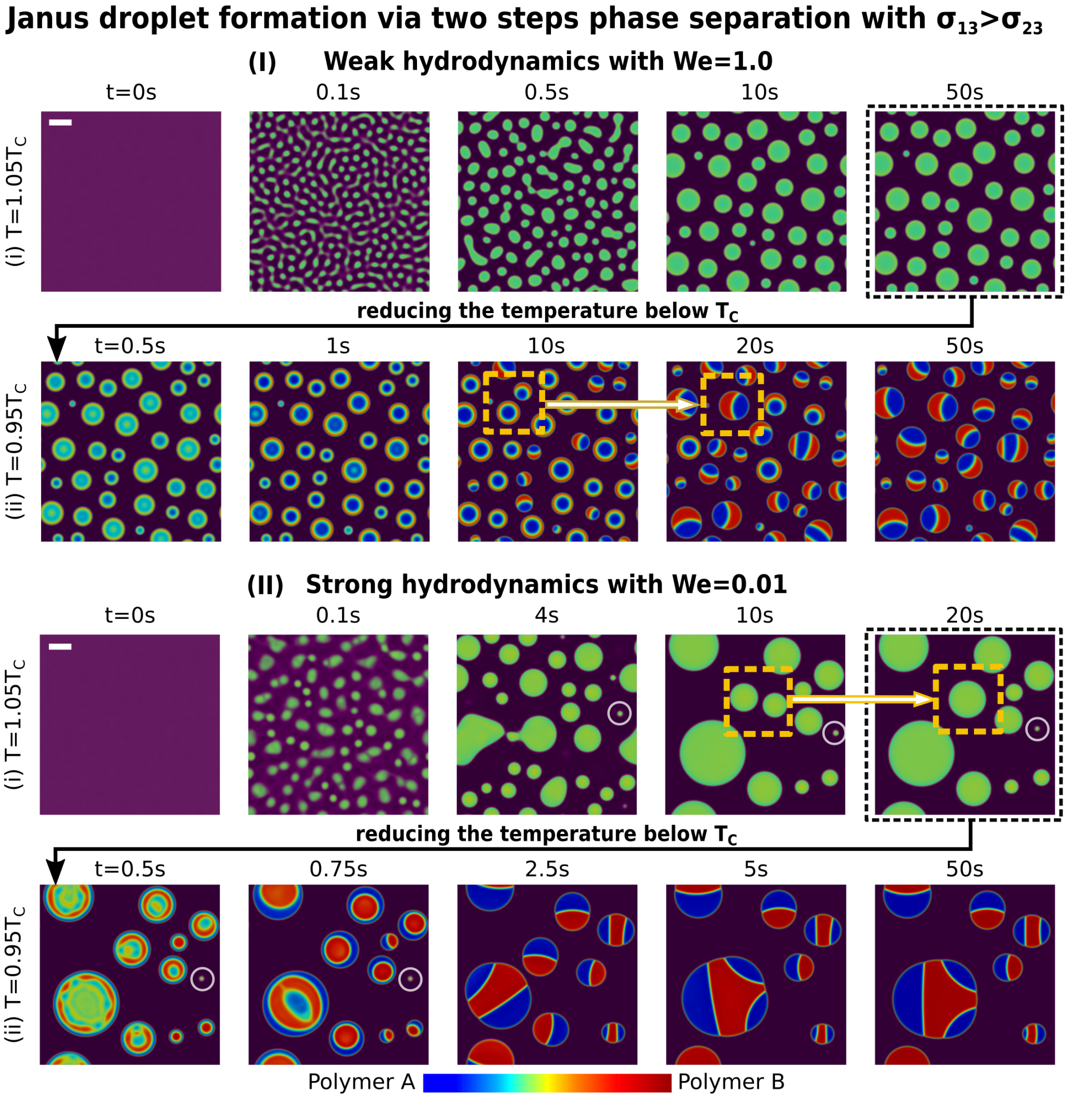

Figure 5.8.: Janus droplet formation via phase separation with the surface tension of polymer A (σ_{13}) larger than the surface tension of polymer B (σ_{23}). (I) The spinodal decomposition coupling with a weak capillary effect with $We = 1$. Step (i): at high temperature: $T = 1.05\,T_c$; step (ii): at low temperature: $T = 0.95\,T_c$. (II) The spinodal decomposition coupling with a weak capillary effect with $We = 0.01$. (i) High temperature: $T = 1.05\,T_c$; (ii) low temperature: $T = 0.95\,T_c$. The simulation domain size is 400 μm × 400 μm.

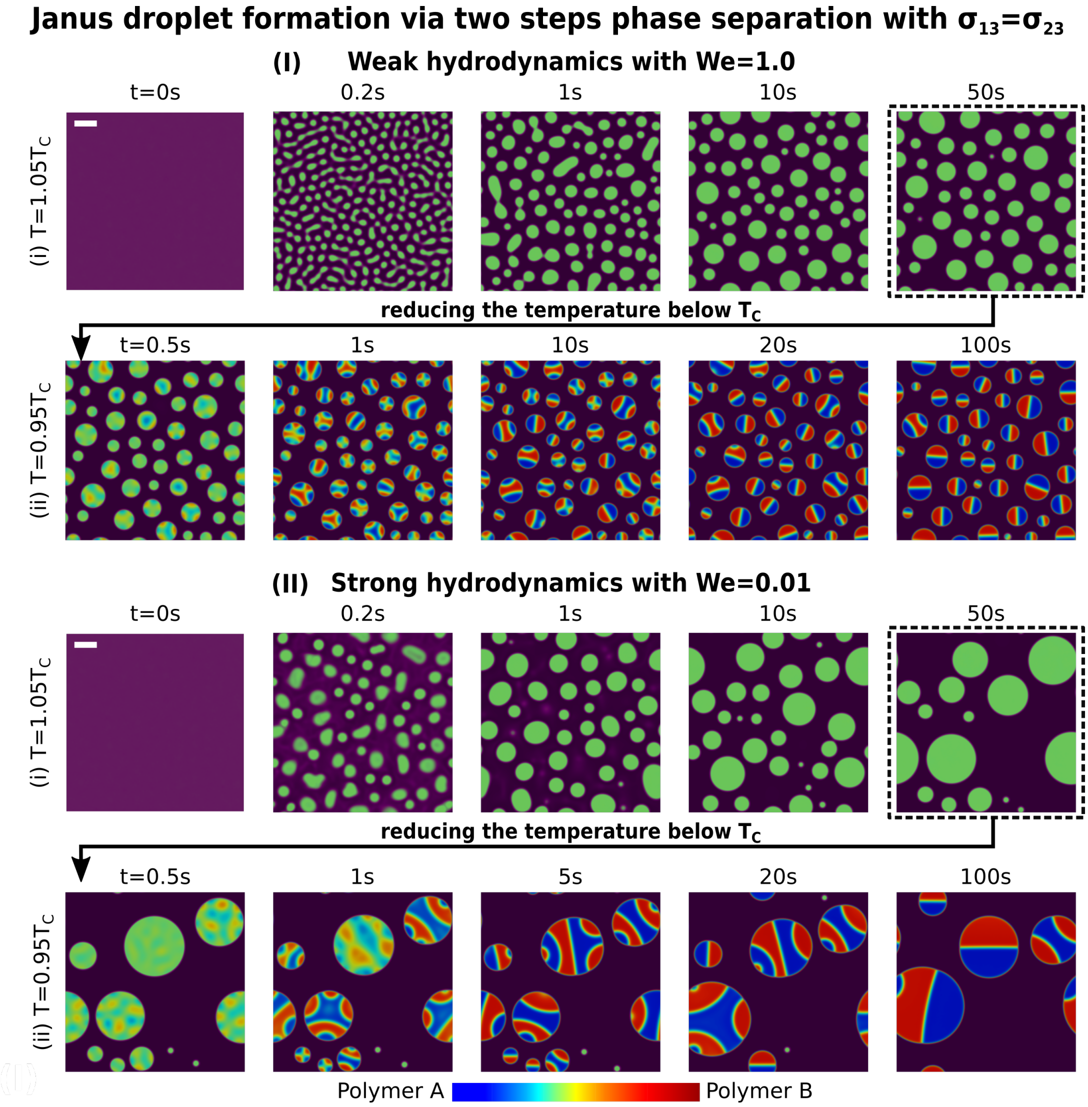

Figure 5.9.: Janus droplet formation via phase separation with the surface tension of polymer A (σ_{13}) equal to the surface tension of polymer B (σ_{23}). (I) The spinodal decomposition coupling with a weak capillary effect with $We = 1$. Step (i): at high temperature: $T = 1.05\,T_c$; step (ii): at low temperature: $T = 0.95\,T_c$. (II) The spinodal decomposition coupling with a weak capillary effect with $We = 0.01$. (i) High temperature: $T = 1.05\,T_c$; (ii) low temperature: $T = 0.95\,T_c$. The simulation domain size is 400 μm × 400 μm.

5.3. Conclusion

In summary, I have presented a multi-component and multi-phase Cahn-Hilliard-Navier-Stokes model to simulate the formation of the Janus droplet via the thermally induced liquid-liquid phase separation. By considering the initial polymer composition, Flory parameters, and the interfacial tension parameters, I elucidate the competing mechanisms for the morphological evolution, namely, i) the diffusion dominated phase separation process, and ii) the minimization of the interfacial energy. Due to the interplay of these two crucial factors, various transient morphologies of the droplets have been observed, including the polygon shaped structures and patchy droplets which need to be investigated in detail in future work. Most importantly, I stress the significance of hydrodynamic effect. Owing to the curtailed diffusivity of entangled long polymer chains, the composition inhomogeneity induced Marangoni effect becomes comparable with the diffusion of polymeric species. Hence, not only the phase separation process of the droplet, but also the droplet coalescence are magnificently accelerated by the Marangoni flow, which results in a broad range for the size of Janus droplets. Further systematic computational studies of material properties and pattern correlations will be considered in the forthcoming researches. As the approach is already capable to be applied in 3 dimensional structures, the 3D simulation of the Janus droplet will be conducted and analysed. I believe that the present research involving Janus droplet formation via diffusion as well as fluid dynamics will shed new light on multi-phase microfluidic manipulation technology for wide applications.

6. Multi-component phase separation inside the electric field[1]

6.1. System definition

In this chapter, I present the Chan-Hilliard-Navier-Stokes-Gauss model based on Ref. [85, 86], to investigate a multi-component fluid system coupled with hydrodynamics and electrodynamics inside the domain Ω enclosed by the boundary S, as schematically illustrated in Fig. 6.1. The domain is subjected to an electrical field $\mathbf{E}$ with voltages Ψ_1 and Ψ_0 at the top and bottom boundaries, respectively. The electrostatic potential is represented by Ψ. The fluid consists of N components and the space $\boldsymbol{x}$ and time t dependent fluid composition is represented by $\boldsymbol{c} = (c_1, c_2, \dots, c_N)$. The number of the immiscible phases in the N-component system depends on the formulation of the chemical free energy $\mathcal{F}$. The density of the fluid $\rho(\boldsymbol{x})$ does not vary with time within the scope of incompressible fluids. The convection velocity is denoted by $\mathbf{u}$. The charge density is denoted by $\rho_e(\boldsymbol{x}, t)$. The system is at a constant temperature and one atmosphere pressure. No mass and heat in-/outflow are considered at the boundaries of the domain. The system energy functional $\mathcal{L}$ is spatial and temporal dependent and consists of three main parts, namely, the chemical free energy functional $\mathcal{F}$, the macroscopic kinetic energy $\mathcal{K}$, and the electric energy functional $\mathcal{U}$

$$\mathcal{L} = \mathcal{F}(\boldsymbol{x}, t, \boldsymbol{c}, \nabla \boldsymbol{c}) + \mathcal{K}(\boldsymbol{x}, t, \rho, \mathbf{u}) + \mathcal{U}(\boldsymbol{x}, t, \rho_e, \nabla \Psi).$$

Other notations applied in this work for the model description are documented in Chapter III. To simulate the phase separation inside the electric field, the CHNSG model is applied. More detailed descriptions is documented in Chapter III.

6.2. Numerical stability and validation

6.2.1. Mesh resolution

In the first part, I present the numerical stability of our model and vary the resolution by changing Δx from 0.5 to 4.0. The initial simulation setup is illustrated in Fig. 6.2(II) in which a droplet with the equilibrium composition $c_m = 0.973$ and diameter $d_0 = 80$ is placed amid a 240×240 fluid matrix with the equilibrium composition $c_d = 0.027$; see Fig. 6.2(II). The electric potential in the domain takes $\Psi_1 = 10$ at the boundary top and

---

[1] Copyright notice: This chapter is licensed under a Creative Commons Attribution-Non Commercial 4.0 International License (CC BY-NC 4.0): https://creativecommons.org/licenses/by-nc/4.0/deed.en

$\Psi_0 = 0$ at the bottom. The conductivity σ of the droplet and matrix are chosen as 5.0 and 1.0, respectively, while their permittivity ε are assigned to be 80.0 and 1.0. The Flory parameter of the free energy density f in Eq. (1.3) is fixed as $\chi = 3.78$, together with the surface parameter $\kappa = 1.0$ and $\epsilon = 4.0$. The density and viscosity of both droplet and matrix are set to be 1.0. After the non-dimensionalization process, we adopt the following non-dimensionalized number in the simulations as

$$\text{P\'e} = 1.0, \quad \text{We} = 1.0, \quad \text{Re} = 1.0, \quad \text{Ca}_E = 1.0.$$

For the solution of the incompressible Navier-Stokes equation and Poisson equation, I select the residual threshold eps= 10^{-7} for the numerical accuracy, which will be discussed in the next part.

Here, two criteria are available for the evaluation process, namely the deformation factor D and the surface charge C_e. The deformation factor reflects the oval shape of the droplet inside the electric field. Fitting the droplet interface with an ellipse, D is calculated as

$$D = \frac{a-b}{a+b}, \tag{6.1}$$

where a and b represent the lengths of the semi-major axis (align with the x-axis) and the semi-minor axis (the y-axis), respectively. In the diffuse interface phase-field model, the droplet interface position denotes the location with $c = 0.5$, based on which a and b are fitted with the least squares method. The surface charge density C_e is integrated by the charge density ρ_e along the y-axis of the oval droplet from the center as

$$C_e = \int_{Ny/2}^{Ny} \rho_e \, dy. \tag{6.2}$$

As shown in Fig. 6.2(I), both D and C_e converge with the reduction in Δx at the constant interface width parameter $\epsilon = 4.0$. The difference is attributed to the calculation of the induced charge density ρ_e, as demonstrated in Fig. 6.2(III) and (V), especially in the x direction. In addition, the electric field distribution at the droplet-matrix interface is also

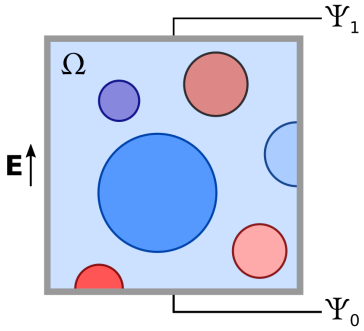

Figure 6.1.: Schematic of the multicomponent fluid system amid the domain Ω within the electric field **E**. The domain boundary S is colored in grey. The voltages at the top and bottom boundaries are Ψ_1 and Ψ_0, respectively.

modified which can be noticed in the inset of Fig. 6.2(IV). And only subtle variance is observed in the concentration distribution of Fig. 6.2(f). To achieve acceptable accuracy and save calculation time, I adhere to $\Delta x = 1.0$ in the following parts.

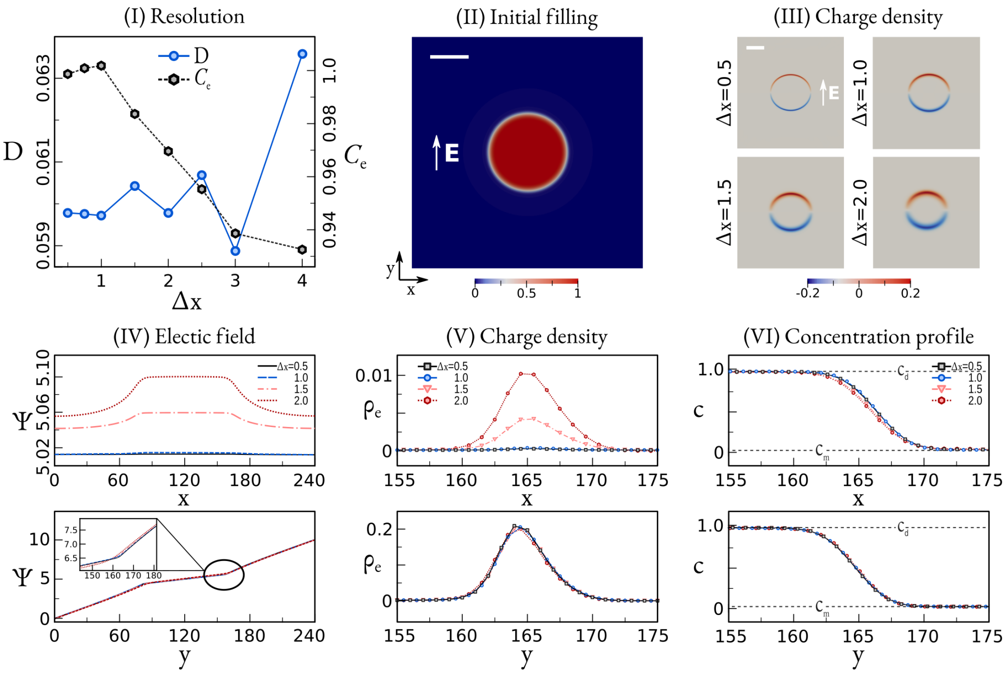

Figure 6.2.: (I) The validation with the mesh resolution Δx. Blue dots: deformation factor D with Δx; black hexagons: surface charge density C_e with Δx. (II) Initial filling of the red droplet inside the blue matrix. The scale bar denotes 40 and the colorbar measures the droplet concentration. (III) Charge density ρ_e at $t = 1e4$ scaled by the colorbar below. (IV) (V) and (VI) illustrate the electric potential Ψ, charge density ρ_e, and droplet concentration c at $t = 1e4$ in x and y directions, respectively.

6.2.2. Interface width-Cahn number Cn

In the second part, the influence of the interface width w on the numerical accuracy is discussed. Here, I alter the model parameter ϵ in the free energy density functional Eq. (2.1) from 0.5 to 4.0. In this way, the so-called Cahn number $\mathrm{Cn} = w/d_0$ to express the ratio of the interface width to the droplet diameter. By setting a larger ϵ, the interface width increases, and so as Cn. The result in Fig. 6.3(I) implies that both the deformation factor D and the surface charge density C_e indicate $\mathrm{Cn} = 0.1$ ($\epsilon = 4.0$) to be a good compromise between accuracy and calculation speed.

Here, I address that the surface charge density C_e is the key value of the validation process, rather than the charge density ρ_e. With the widened interface with Cn, the composition gradient ∇c reduces (see Fig. 6.3(III)) which results in the decreasing permittivity gradient $\nabla \varepsilon = (d\varepsilon/dc)\nabla c$. While the surrounding electric potential Ψ is hardly modified, for there are not huge amounts of induced charges in our simulations. Resulting from this,

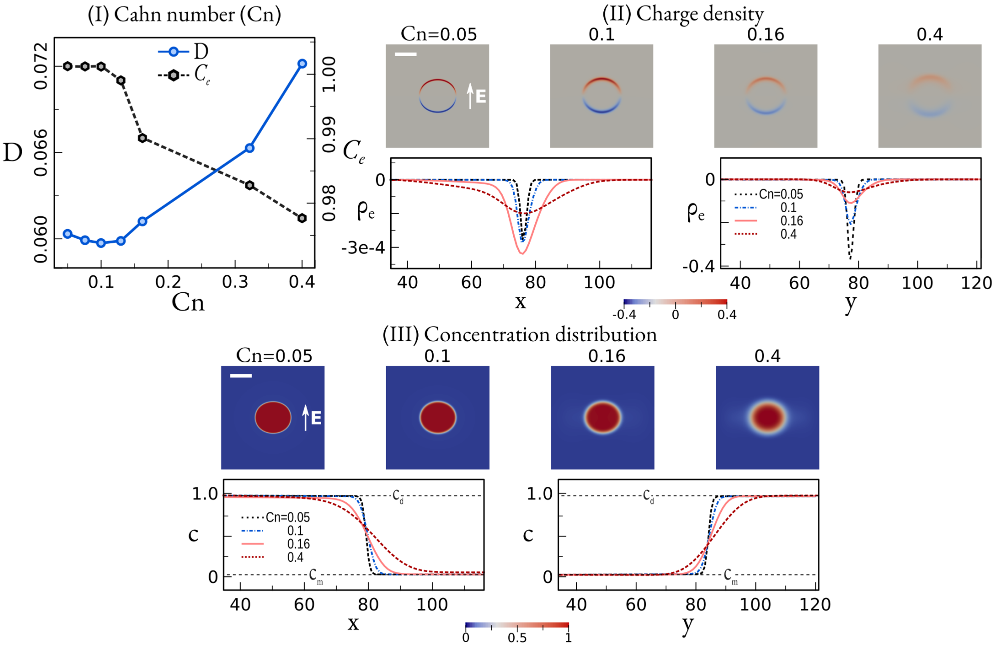

Figure 6.3.: (I) The validation with the Cahn number (Cn=w/d_0). Blue dots: deformation factor D with Cn; black hexagons: surface charge density C_e with Cn. (II) Charge density at $t = 10^4$. Upper row: charge density distribution; lower row: intersections along x and y directions. The upper and lower domain borders are constrained with the electric potential $\Psi_1 = 10$ and $\Psi_0 = 0$, respectively. The scale bar denotes 50 and the colorbar scales ρ_e. (III) Concentration field at $t = 1e4$ with the colorbar below measures the droplet concentration.

the calculated ρ_e by the Poisson equation changes with Cn as

$$\nabla \cdot (\epsilon \nabla \Psi) = \nabla \epsilon \cdot \nabla \Psi + \epsilon \nabla^2 \Psi = \frac{d\epsilon}{dc} \nabla c \cdot \mathbf{E} + \epsilon \nabla^2 \Psi = -\rho_e \tag{6.3}$$

In fact, according to the Gaussian law, the induced charge wrapped by a closed surface should be irrelevant to the interface width. Hence, I choose the more appropriate C_e as the criterion for deciding the resolution Δx and interface width parameter ϵ, rather than the charge density ρ_e.

6.2.3. Residual threshold eps and time step

In this part, I focus on the numerical accuracy of solving the Navier-Stokes equation and Poisson equation. Two factors are investigated, namely the residual threshold eps and the time step Δt. Here, eps controls the accuracy of the Poisson equation solutions for the Navier-Stokes equation, as well as the Gaussian equation. When the absolute residual values of these two equations become smaller than the preset eps, the iteration stops and returns the velocity $\mathbf{u}$ and electrical potential Ψ. As illustrated in Fig. 6.4, the deformation factor D shows hardly any prominent influence by eps and Δt. But the surface charge density C_e converges as eps$\leq 1e-8$ and $\Delta t \leq 1e-4$. So I choose eps$= 1e-8$ and $\Delta t = 1e-4$ in all other simulations of this work.

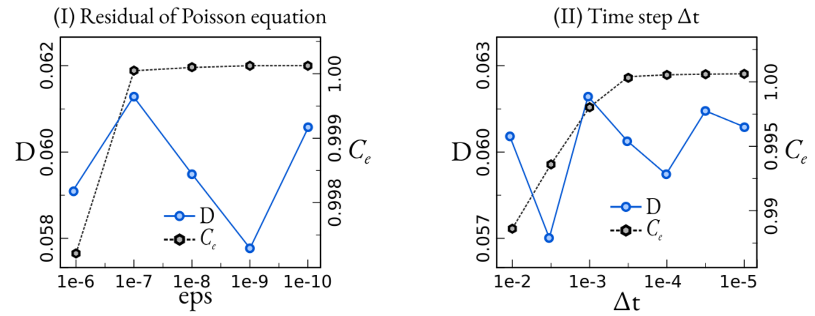

Figure 6.4.: Convergence of the droplet deformation factor D and the surface charge density C_e with (I) the residual threshold of Poisson equation eps and (II) the time step Δt.

6.3. Model validation with Taylor's theory

For the leaky dielectric droplet inside the electric field, its shape is deformed into an ellipse. The deformation factor D has been deduced as a function of permittivity ratio $\varepsilon_d/\varepsilon_m$, conductivity ratio σ_d/σ_m, and the electro-capillary number Ca_E. In Ref. [87], Taylor derived the deformation factor

$$D = \frac{9\,\mathrm{Ca}_E}{16} \frac{(\sigma_d/\sigma_m)^2 + 1.5\,\sigma_d/\sigma_m - 3.5\,\varepsilon_d/\varepsilon_m + 1}{(\sigma_d/\sigma_m + 2)^2}. \tag{6.4}$$

Another derivation in 2-dimensional case is achieved by Feng [88] who presents the following expression,

$$D = \frac{\mathrm{Ca}_E[(\sigma_d/\sigma_m)^2 + \sigma_d/\sigma_m - 3\,\varepsilon_d/\varepsilon_m + 1]}{3(\sigma_d/\sigma_m + 1)^2}. \tag{6.5}$$

In the following parts, I validate our model by changing the permittivity ratio $\varepsilon_d/\varepsilon_m$, conductivity ratio σ_d/σ_m between droplet and matrix, and the electro-capillary number Ca_E. The simulated droplet deformation factor D is compared with both Eqs. (6.4) and (6.5).

6.3.1. Permittivity

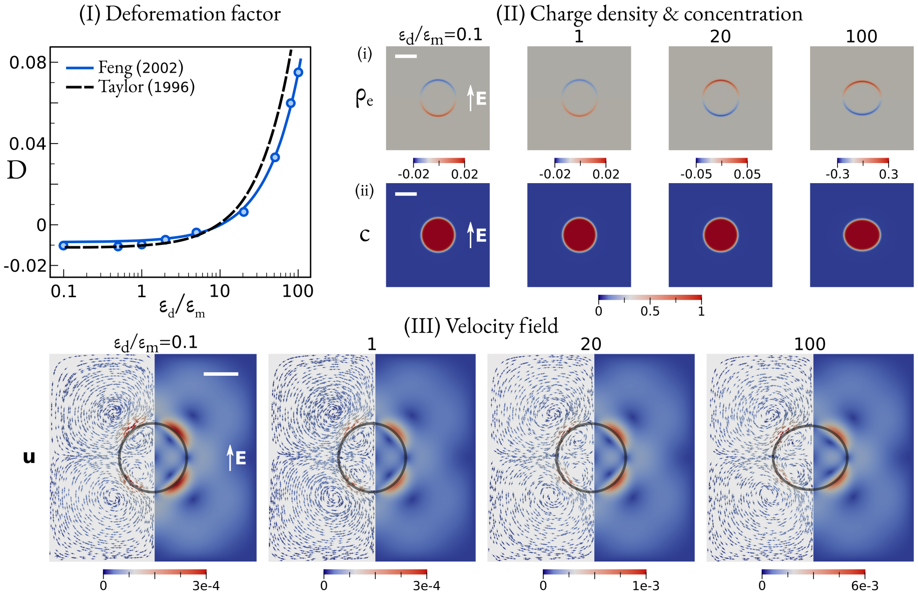

Figure 6.5.: (I) The droplet deformation factor D with the permittivity ratio $\varepsilon_d/\varepsilon_m$ between droplet and matrix, compared with Taylor's (black dashed line) and Feng's theory (blue solid line). (II)(a) The charge density ρ_e and (b) the concentration distribution c. (III) Left half panel: the velocity field $\mathbf{u}$; right half panel: $|\mathbf{u}|$ scaled by the color bar below. The grey circles mark the droplet interfaces.

The initial setup is identical to Sec. 6.2.1, as shown in Fig. 6.2(II). The permittivity ratio $\varepsilon_d/\varepsilon_m$ varies from 0.1 to 100. The simulated deformation factor presents two behaviors, as depicted in Fig. 6.5(I). At $\varepsilon_d/\varepsilon_m < 10.3$, $D < 0$ denotes a prolate droplet shaped under the electric field. While for the setup with $\varepsilon_d/\varepsilon_m > 10.3$, the droplet is stretched in the horizontal direction forming an oblate ellipse with $D > 0$. The droplet morphology snapshots in Fig. 6.5(II) clearly demonstrate the shape changing from prolate to oblate with increasing $\varepsilon_d/\varepsilon_m$. Compared with Eqs. (6.4) and (6.5), a better match gives credit to Feng at a larger permittivity ratio, and the droplets with $\varepsilon_d/\varepsilon_m \leq 1.0$ are more consonant with Taylor's theory. As discussed in previous researches [89, 34], the droplet deformation is propelled by the induced interfacial charges, which change signs at $\varepsilon_d/\varepsilon_m = 10.3$ (see Fig. 6.5(II)). Resulting from this, the Coulomb force and the dielectric force trigger the fluid flow tangent to the droplet interface. For $\varepsilon_d/\varepsilon_m > 10.3$, the material flows from pole to equator, while reversed at $\varepsilon_d/\varepsilon_m < 10.3$, which is illustrated by the velocity vectors in Fig. 6.5(IV). Consequently, the droplet shows diverse ending equilibrium morphologies.

6.3.2. Conductivity

Next, the conductivity ratio between the droplet and matrix σ_d/σ_m is varied from 0.5 up to 100.0 at the constant permittivity ratio $\varepsilon_d/\varepsilon_m = 80.0$. All other simulation parameters are identical to Sec. 6.3.1. The comparison with Taylor and Feng's theory is demonstrated in Fig. 6.6 and the good consistency of the droplet deformation factor D with Feng's equation (blue solid line) can be observed.

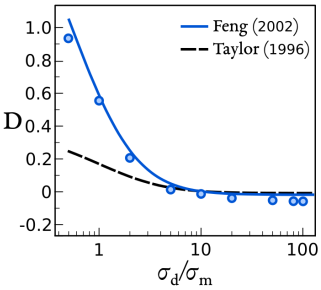

Figure 6.6.: The droplet deformation factor D with the conductivity ratio σ_d/σ_m between droplet and matrix, compared with Taylor's (black dashed line) and Feng's theory (blue solid line).

6.3.3. Electro-capillary number

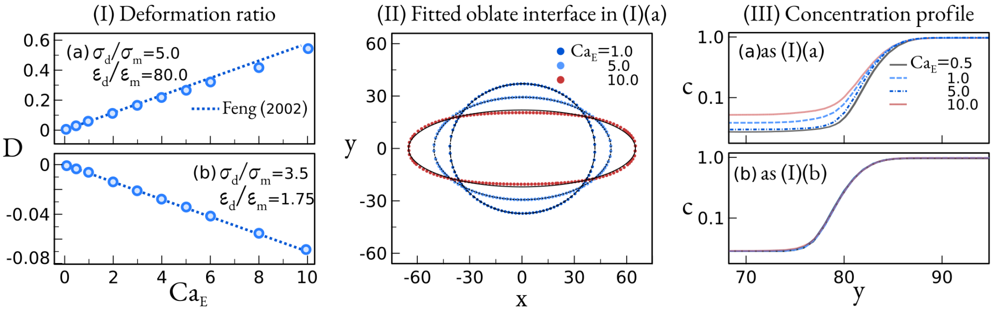

Figure 6.7.: (I) The droplet deformation factor D with the electro-capillary number Ca_E, compared with Feng's theory (blue dashed lines), (a) oblate droplets; (b) prolate drops. (II) The droplet interface with various Ca_E of the oblate drops. Dots: simulated interface positions with $c = 0.5$; lines: elliptical fitting with the least squares method. (III) concentration profiles of the interface intersected at x=0, (a) oblate; (b) prolate.

Next, I alter the electro-capillary number Ca_E. Here, two scenarios are considered, the oblate and prolate droplet (named after the final morphology). Setting the permittivity ratio $\varepsilon_d/\varepsilon_m = 80.0$ and the conductivity ratio $\sigma_d/\sigma_m = 5.0$, the droplet deformation factor D shows a linear relationship with Ca_E, as guided by the blue dashed line in Fig. 6.7(I)(a). Similarly, for the prolate drops, by choosing $\varepsilon_d/\varepsilon_m = 1.75$ and $\sigma_d/\sigma_m = 3.5$, $D \propto \mathrm{Ca}_E$ is in good agreement with Feng's theory. Some discrepancies are expected at large Ca_E setups where the droplet interface deviates from the elliptical shape. Clearly noticeable in Fig. 6.7(II), the interface position marked by the red dots for $\mathrm{Ca}_E = 10.0$ shows large mismatches with the solid ellipse line fitted with the least squares method. In this way, both Taylor and Feng's analytical equations are incapable of describing the real stretched interface. In our model, I observe another mechanism attributing to this derivation which is not considered in previous researches. As I compare the concentration distribution along the interface between different Ca_E in Fig. 6.7(III)(a), the interface widens itself and the matrix equilibrium concentration increases with Ca_E. It indicates that the thermodynamic equilibrium is modified by the external field.

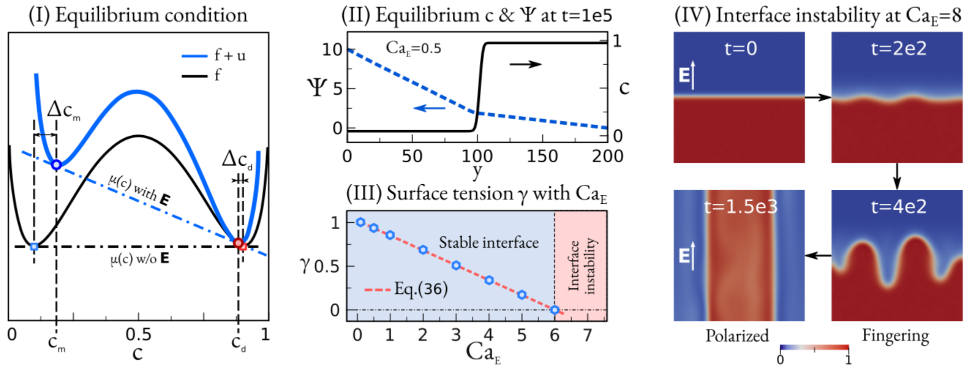

Figure 6.8.: (I) The schematic equilibrium condition. The free energy densities with and without the electric field strength **E** are depicted with the solid blue and black lines, respectively. The dot-dashed lines are the common tangent at equilibrium, with the open dots marking the equilibrium compositions c with **E** and open squares for c without **E**. (II) The equilibrium concentration c and electric potential Ψ at $t = 1e5$ with the electro-capillary number $\mathrm{Ca}_E = 0.5$. (III) Droplet-matrix interfacial tension $\gamma < 0$ with Ca_E number. The simulated values (open dots) fall on the theoretical line with Eq. (6.7). The red-colored region highlights the interfacial instability with $\gamma < 0$ at $\mathrm{Ca}_E \geq 6.0$. (IV) The interface instability evolves with time at $\mathrm{Ca}_E = 8.0$. The color bar scales the composition.

6.4. Thermodynamics with electric fields

To study the electro-thermodynamic equilibrium, a flat droplet-matrix interface is considered, as illustrated in Fig. 6.8(IV)($t = 0$), where the curvature effect is negligible inside the bulk regions with $\kappa\epsilon\nabla^2 c = 0$. In this way, the simplified electrochemical potential reads

$$\mu(c) = \frac{\partial f}{\partial c} - \frac{\partial u}{\partial c} = \frac{\partial f}{\partial c} - \frac{\mathrm{Ca}_E}{2}(\varepsilon_d - \varepsilon_m)\mathbf{E}^2. \tag{6.6}$$

Due to the difference of the conductivity $\sigma(c) = \sigma_d c + \sigma_m(1-c)$, the electric field strength $\mathbf{E}_m$ inside the bulk matrix becomes larger than $\mathbf{E}_d$ amid the bulk droplet, as shown by the simulated equilibrium electric field in Fig. 6.8(II). Moreover, the electric field strength $\mathbf{E}$ changes the energy state of the droplet and matrix, leading to the right-lopsided free energy density $f+u$ which is schematically illustrated in Fig. 6.8(I). At equilibrium, the new equilibrium compositions c_m and c_d of each phase are established by the tilted blue dot-dashed common tangent line. In the matrix phase, the equilibrium concentration c_m shows a larger deviation Δc_m than Δc_d inside the droplet. Due to the equilibrium concentration changes, the surface tension is affected by the electric field and can be expressed by the following integral from $y = 0$ to ∞ as

$$\begin{aligned}\gamma &= \int_0^\infty \left[\Delta f(y) + \Delta u(y) + \frac{\kappa\epsilon}{2}(\nabla c)^2\Big|_y - \frac{\mathrm{Ca}_E}{2}|\nabla\varepsilon|(\nabla\Psi)^2\Big|_y\right] dy \\ &= \int_0^\infty \left[\kappa\epsilon(\nabla c)^2 - \mathrm{Ca}_E|\nabla\varepsilon|\mathbf{E}^2\right] dy \\ &= \gamma^* - \mathrm{Ca}_E \int_0^\infty |\nabla\varepsilon|\mathbf{E}^2 dy. \end{aligned} \tag{6.7}$$

Testified in our simulations shown in Fig. 6.8(III), the surface tension γ follows the linear relationship with Ca_E. A further increase in the electric effect can result in interface instability. As demonstrated in Fig. 6.8(IV) with $\mathrm{Ca}_E = 8.0$, the interface starts to oscillate and develops the fingering morphology at $t = 4e2$. Finally, the droplet phase gets polarized and its interface lays parallel to the electric field direction at $t = 1.5e3$. With further enhancing the dielectric force, the surface tension converges to zero.

Inferring from the above discussion, I emphasize two crucial mechanisms contributing to the fluid deformation inside the electric field. (I) The dielectric force proportional to $-\sum_{i=1}^N c_i(\delta u/\delta c_i) - \rho_e(\delta u/\delta \rho_e)$. (II) The droplet surface tension reduction proportional to $-\mathrm{Ca}_E|\nabla\varepsilon|\mathbf{E}^2$. Resulting from this, the fluid gets stretched and expands its surface area most rapidly in the direction with the largest surface tension decrease. The electric field induced surface tension drop is vastly ignored in previous researches and should be carefully scrutinized for the surface tension force treatment in the front-tracking simulation methods, such as LS and VOF.

In addition, I suggest a more complex phase diagram for the binary fluids inside the electric field, as illustrated in Fig. 6.9(I). According to Gibbs' phase rule, the degree of freedom F = C − P + n is decided by the component number C= 2, the phase number P, and the external factor number n. In isobaric cases, n= 2 represents the two decisive factors, namely the temperature T and electric field strength $\mathbf{E}$. Theoretically, the equilibrium compositions c_m and c_d can be calculated with

$$\begin{gathered}\mu(c_m) = \mu(c_d) = \mu_e, \\ \left[f(c_m) + u(c_m)\right] - \left[f(c_d) + u(c_d)\right] = \mu_e(c_m - c_d), \\ |\mathbf{E}_m| = \frac{\Psi_1 - \Psi_0}{L}\frac{\sigma(c_d)}{\sigma(c_m) + \sigma(c_d)}, \quad |\mathbf{E}_d| = \frac{\Psi_1 - \Psi_0}{L}\frac{\sigma(c_m)}{\sigma(c_m) + \sigma(c_d)}. \end{gathered} \tag{6.8}$$

Instead of the binodal line, the equilibrium composition is expressed by a 3-dimensional binodal surface, as highlighted in Fig. 6.9(I). Simulated at various temperatures T; see

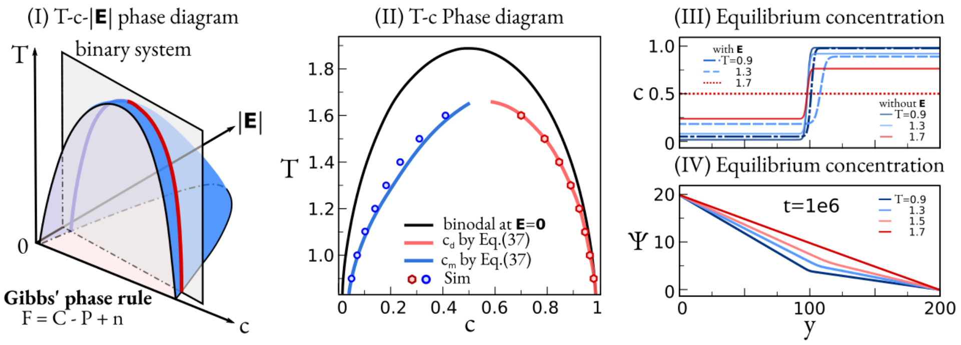

Figure 6.9.: (I) The schematic phase diagram (PD) of the binary fluid system with temperature T-composition c-electric field strength $|\mathbf{E}|$ obeying the Gibbs' phase rule. (II) The binodal compositions with temperature T are influenced by the electric field and deviate from the black binodal line ($\mathbf{E}= 0$). Open dots: simulation as in (III) and (IV); solid colored lines: theory with Eq. (6.8). (III) Equilibrium concentration profile across the interface with temperature T at $\mathbf{E}= \mathbf{0}$ (solid lines) and with $\mathbf{E}$ (dashed lines) as (II). (IV) Equilibrium electrical field Ψ with temperature T at $t = 1e6$ with $\Psi_1 = 20$ at $y = 0$ and $\Psi_0 = 0$ at $y = 200$. Rest parameters are identical to Fig. 6.2.

Fig. 6.9(III) and (IV), the T-c phase diagram for the binary fluid system at $\mathrm{Ca}_E = 1.0$ is recovered in Fig. 6.9(II). Both c_m (blue open dots) and c_d (red open dots) deviate largely from the black solid **E**-free binodal line and show good consistencies with the theoretical colored binodal lines calculated via Eq. (6.8).

6.5. Dynamics with capillary wave theory

In the previous section, thermodynamics, especially the equilibrium states, are discussed. In this section, I study energy dissipation with the help of the capillary wave theory (CWT). For liquid surfaces perturbed by small thermal noises, its energy dissipation obeying CWT has been proved by several experiments [46, 47]. When the perturbation is small, the increase in the surface energy ΔE is proportional to the change in the surface area as

$$\Delta E \approx \frac{\gamma}{2} \int (\nabla h)^2 \, dxdy, \tag{6.9}$$

where the interface position h is marked by the location with the droplet composition $c = 0.5$. After Fourier transformation, Eq. (6.9) is rewritten as

$$\Delta E(q) = \frac{\gamma}{2} \int q^2 \left|\Delta \widetilde{h}(q)\right|^2 dq,$$

where q denotes the wave frequency, and $\Delta \widetilde{h}^2(q)$ stands for the capillary wave amplitude. At equilibrium, each wave mode of the fluctuation has the energy of $k_B T$, which says

$$\left\langle \Delta \widetilde{h}^2(q) \right\rangle = \frac{k_B T}{4\pi^2 q^2 \gamma}. \tag{6.10}$$

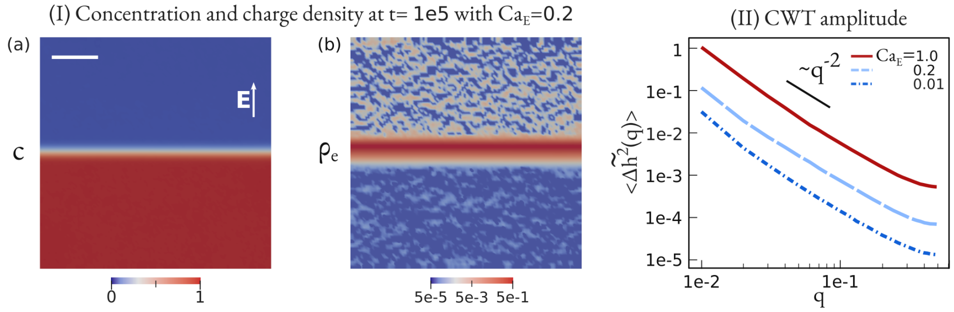

Figure 6.10.: (I) The exemplary composition c and charge density ρ_e perturbed by the composition noise $\xi_c = (0.01, 0.01)$ at $t = 1e5$ with $\mathrm{Ca}_E = 0.1$. The color bar of ρ_e value is in log-scale. (II) The capillary wave amplitudes $\langle \Delta\widetilde{h}^2(q)\rangle$ with the wave frequency q for different Ca_E numbers. The black solid line guides $\langle \Delta\widetilde{h}^2(q)\rangle \sim q^{-2}$.

To validate the energy dissipation of the droplet interface in our electro-hydro-thermodynamic model, a flat fluid-fluid interface is placed in the center of a 100 × 100 domain, as shown in Fig. 6.10(I)(a). All other setups are identical to Sec. 6.3.3. Perturbed by the compositional fluctuation with the amplitude of $\xi_c = (0.01, 0.01)$, the induced charges are clearly visible at both interface and the bulk regions, as demonstrated in Fig. 6.10(I)(b). This observation is totally distinct from the charge distribution without noise; see Fig. 6.2(II). By varying Ca_E from 0.01 to 1.0, the capillary wave amplitude $\left\langle \Delta\widetilde{h}^2(q)\right\rangle$ in Fig. 6.10(II) not only shows the q^{-2} scaling law predicted by the CWT, but also magnifies with the increase in Ca_E. This observation indicates that the leaky dielectric droplet still follows CWT, which suggests the energy dissipation via surface energy reduction.

6.6. Result and discussion

In this section, I discuss the droplet coalescence and spinodal decomposition of an A-B-C ternary system with the electro-hydro-thermodynamic model. Choosing the free energy parameters in Tab. 6.1, the ternary phase diagram in Fig. 6.11 has three local minimal states, as marked by the red open dot for component 1 rich phase A, the blue open dot for component 2 dense phase B, and the purple open square for C. The corresponding equilibrium compositions for phases A, B, and C are $(0.770, 0.115, 0.115)$, $(0.115, 0.770, 0.115)$, and $(0.115, 0.115, 0.770)$, respectively.

6.6.1. Ternary droplet coalescence

For binary system, abundant previous results [89] are available for the droplet coalescence with electro-hydrodynamics. The droplets merge by minimizing the surface energy, resulting in the final morphology of a single droplet. With our multi-component model, I elucidate the ternary droplet coalescence by placing the red droplet (component 1 riched phase A) and another blue droplet (component 2 dense phase B) in a 240 × 480 purple matrix (phase C) domain. The initial droplet radii are 40 and their spacing is set to be 40,

Parameters	Description	Values
$\chi_{12}, \chi_{13}, \chi_{23}$	Flory parameters	2.5, 2.5, 2.5
χ_{123}	Triple interaction parameter	3.5
κ	Surface tension parameter	1.0
ϵ	Interface width parameter	4.0
D_1, D_2, D_3	Diffusivity for each component	1.0, 1.0, 1.0
ρ_1, ρ_2, ρ_3	Density for each component	1.0, 1.0, 1.0
η_1, η_2, η_3	Viscosity for each component	1.0, 1.0, 1.0

Table 6.1.: Simulation parameters for the ternary system.

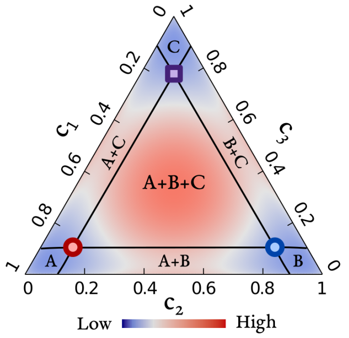

Figure 6.11.: Ternary phase diagram of an A-B-C system, on which the equilibrium composition of A, B, and C are marked by the red open dot, blue open dot, and purple open square, respectively. The parameters of free energy density are tabulated in Tab. 6.1. The color bar measures the free energy density magnitude.

as shown in Fig. 6.12(I)(a). The external electric field parallel to the x-direction is applied with $\Psi_1 = 24.0$ at the left boundary and $\Psi_0 = 0$ at the right. Here, the conductivity for each component is assigned to be $(\sigma_1, \sigma_2, \sigma_3) = (5.0, 1.0, 1.0)$ and a special permittivity setup is chosen as $(\varepsilon_1, \varepsilon_2, \varepsilon_3) = (50.0, 1.0, 5.0)$.

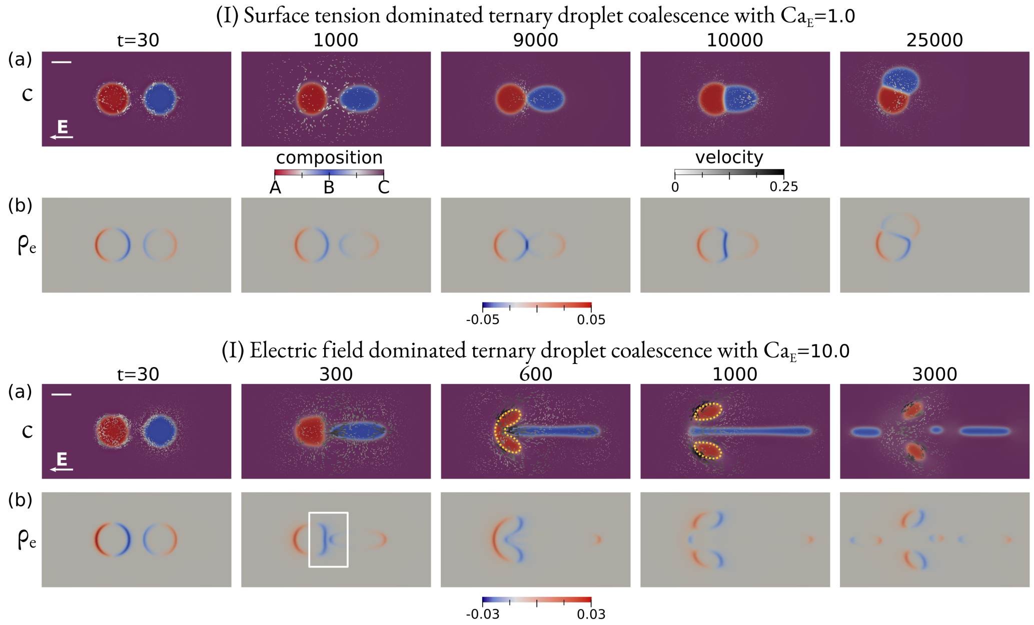

Figure 6.12.: Ternary droplet coalescence coupled with electro-hydrodynamics. (I) Surface tension dominant coalescence with a weak electrostatic effect, $\mathrm{Ca}_E = 1.0$. (a) The composition field $\boldsymbol{c}$ evolves with time and the color bar shows red for droplet A, blue for droplet B, and purple for matrix C. The velocity field is stacked on the same figure. (b) The evolution of the charge density ρ_e with time and the values are scaled by the color bars beneath the figure. (II) The electric field dominated droplet motion with a strong electrostatic effect, $\mathrm{Ca}_E = 10.0$. The velocity magnitude is measured by the vector cone size, as well as the white-black color bar.

Clearly noticeable in charge density distribution in Fig. 6.12(I)(b), the selected permittivity ratio emerges negative charges at the right side of droplet A, directly towards the charges with the same sign on the left side of droplet B. This scenario can never take place in the binary system and the repulsive Coulomb force of the same charges can magnificently alter the droplet coalescence. By setting a weak electric capillary effect with $\mathrm{Ca}_E = 1.0$, the surface tension overwhelms the electric forces. The Coulomb force scaled by Ca_E is too weak to stop the aggregation of the negative charges. At $t = 1e4$, the droplets merge into a Janus particle which is composed of the oblate droplet A and prolate drop B, as depicted in Fig. 6.12(I). After coalescence, the Janus droplet experiences the so-called Quincke rotation [31, 90] counterclockwise. Similar morphological transformations are reported in the Janus droplet [91] and double-emulsion droplet [92].

With further increasing Ca_E to 10.0, the droplet coalescence is entirely denied by the repulsive Coulomb force between A and B, as highlighted by the white squares in

Fig. 6.12(II)(b). The left interface of the red droplet A is firstly deformed into a concave shape, and finally cut into 2 small droplets, as marked by yellow dashed lines in Fig. 6.12(II)(a). Moreover, the strong electrostatic force propels the fluid flow in the whole domain, causing the instability of the elongating blue droplet B which ruptures into 3 satellite drops at $t = 3e3$. Similar droplet breakup has been observed in the electrospinning process [93] and needs to be heeded in future works.

6.6.2. Ternary spinodal decomposition

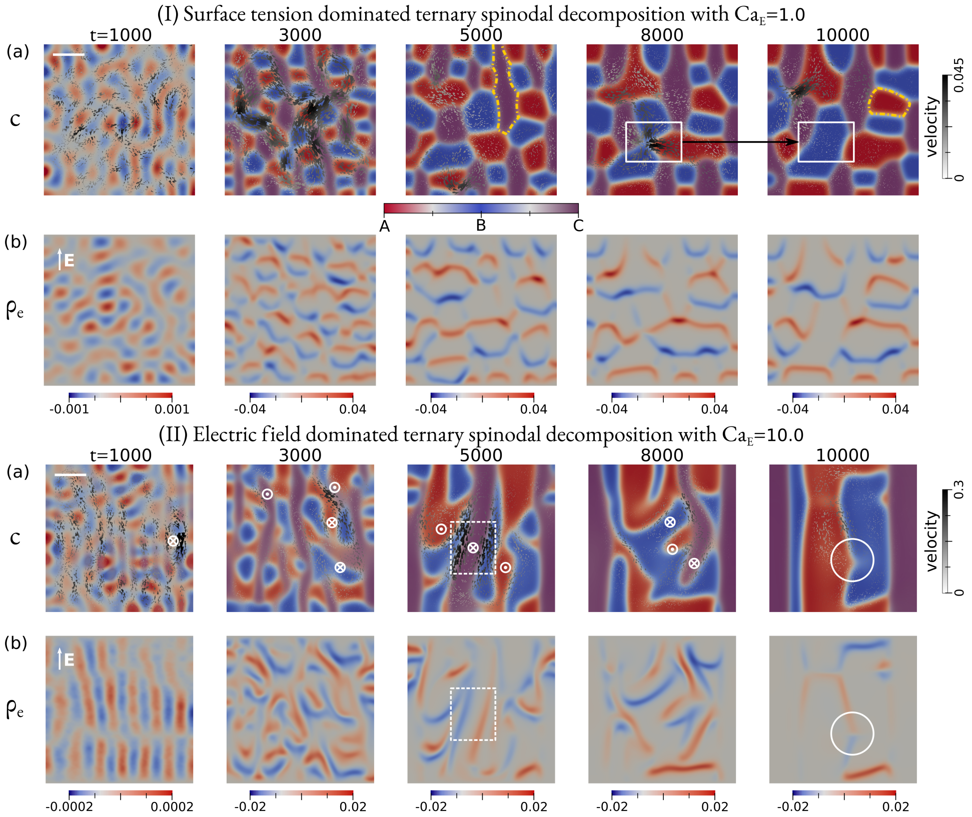

Figure 6.13.: Ternary spinodal decomposition (SP) coupled with electro-hydrodynamics. (I) Surface tension dominant SP with weak $\mathrm{Ca}_E = 1.0$. (a) The composition c stacked by the velocity field (grey cones). Two stretched droplets are highlighted with yellow dot-dashed lines. (b) The charge density ρ_e evolution scaled by the color bars below. (II) The electric field dominated SP with strong $\mathrm{Ca}_E = 10.0$. Some charge-induced vortices are highlighted in white "⊗/⊙" symbols obeying the right-hand rule.

In this part, the influence of electrohydrodynamics on the ternary spinodal decomposition is elucidated. Initially, a homogeneous 200 × 200 domain with composition $\boldsymbol{c} = (0.33, 0.33, 0.34)$ is perturbed by the composition noise with amplitude of $\xi_c = (0.01, 0.01, 0.01)$. The permittivity and conductivity are set to be $(50.0, 25.0, 1.0)$ and $(5.0, 3.0, 1.0)$, and the electric field setup is identical to sec. 6.2.1. Triggered by noises, the phase separation starts and produces a huge amount of interfaces, as shown in Fig. 6.13(I)(a). Due to the selected permittivity ratio, the purple phase C is stretched in y direction by the electric force, while the red phase A elongates in the x direction which is highlighted by the yellow dot-dashed line in Fig. 6.13(I)(a). Since the weak electro-capillary effect with $\mathrm{Ca}_E = 1.0$ is adopted, the surface tension dominates the morphological evolution. The inhomogeneous surface tension induced the so-called Marangoni flow which propels the droplet coalescence. In the white squares of Fig. 6.13(I)(a), the Marangoni flow is sketched by the grey cones. Large flow velocity appears when droplets merge and the fluid flow behaves vastly like the laminar flow with direction perpendicular to the interfaces. Consequently, the final morphology shows only a subtle difference from the spinodal structures with slightly deformed droplets.

By increasing Ca_E to 10.0, the electric effect becomes dominant. The fluid flow is no longer decided by the surface tension itself, and its direction is highly correlated with the charge distribution. Highlighted in the white dashed squares in Fig. 6.13(II), negative charges are induced at the left interface of the purple droplet C, and positive charges on the right side. Therefore, the Coulomb's force results in the upwards fluid flow tangent to the left interface, while the downstream appears on the right. Consequently, the vortex marked by the white "⊗" symbol is produced which rotates the droplet C clockwise. Moreover, the vortex expands to the entire domain until damped by the viscous effect, and results in the rotation of the whole domain. Consequently, the phase separation morphology deviates largely from the spinodal structure in Fig. 6.13(I). In addition, I find the transient state in the white circles in Fig. 6.13(II). Different from the surface tension dominated scenario, the zigzag interface is stabilized by the electric field. Finally, when the induced charges get gradually dissipated by the conduction, all droplets get polarized, forming a lamellar structure parallel to the external field.

6.7. Conclusion

In conclusion, I present a multi-component electro-hydro-thermodynamic model to investigate the droplet behaviors affected by the interplay of diffusion, hydrodynamics, and electric field. The total energy functional for both leaky and perfect dielectric materials is derived and the corresponding energy law is presented. The validation of our model with Taylor and Feng's classic theories is performed in 2D. Most importantly, differing from the previous models, the expression of the electrochemical potential μ is revisited and the dielectric-related correction term is added to recapitulate the models. The modification in the chemical potential leads to a generalized electro-hydro-thermodynamic force including the Kortweg stress and the Maxwell stress. Consequently, the thermodynamic equilibrium is deeply impacted by the electric field which explains the surface tension reduction induced by the electric field that has been observed in many experiments. In addition, our multi-component model enables us to study the ternary droplet coalescence and spinodal decomposition, bringing some interesting observations that can hardly be scrutinized in the binary system. I expect that the present model will help to understand the electrohydrodynamic behaviors of complex droplet systems and deepen our knowledge of droplet/fluid manipulation by the electric field, for instance, in the electrospinning process. Other suggestions for future work could be the electro-wetting/dewetting and ionized surfactant-related phenomena.

7. Conclusion

7.1. Conclusion and remarks

In this doctoral thesis, the investigation primarily focuses on elucidating the behaviors of liquid phase separation (PS) through the utilization of three distinct phase-field models: the Cahn-Hilliard (CH) model, the Cahn-Hilliard-Navier-Stokes (CHNS) model, and the Cahn-Hilliard-Navier-Stokes-Gauss (CHNSG) model. For an in-depth exploration of ternary phase separation predominantly governed by diffusion, an extension of the multicomponent CH model is devised, building upon prior algorithms designed for binary systems. Furthermore, to account for hydrodynamics during PS, the CHNS model is revisited, culminating in an accurate formulation of the surface tension force within the Navier-Stokes (NS) equations, derived from the energy minimization principles. Subsequently, for PS occurring in the presence of an electric field, the CHNSG model is specifically formulated for both leaky and perfect dielectric fluid systems. The respective boundary conditions for electric potential and charge density—namely, Neumann, Dirichlet, and periodic boundary conditions—are applied. Each of these phase-field models undergoes meticulous validation across two critical domains. Firstly, careful attention is paid to numerical stability across all three models, scrutinizing simulation accuracy and convergence by varying resolution and timestep parameters. Specifically, for the CHNS and CHNSG models incorporating NS equations and Gauss' law (including charge), the accuracy and stability of solving the Poisson equation are examined. Secondly, simulation results are rigorously compared against analytical theories or experimental data. For scenarios where interfacial tension significantly influences outcomes, simulated interfacial tensions are validated against experimental values. Simulations involving hydrodynamics entail a comparison of the relationship between droplet pressure and interface curvature with the classic Young-Laplace equation. Additionally, simulations for droplet deformation within an electric field (referred to as electric-hydro-thermodynamic or EHTD cases) are contrasted with analytical theories based on G.I. Taylor and J. Feng.

It is pertinent to note that the initiation of phase separation necessitates perpetual thermal noises, conforming to formulations based on the fluctuation-dissipation theorem (FDT) derived from statistical mechanics. Typically, thermal noise serves as a trigger primarily active during the early stages of PS. Through the simulation of droplet motion under thermal noises, the stochastic CH and CHNS models are effectively validated. The Brownian motion induced by thermal noises is thoroughly discussed, accounting for various parameters such as droplet radii, interfacial tension, temperature, and viscosity. A fundamental characteristic of Brownian particles, as expressed in the quintessential Einstein relation, is the mean squared displacement (MSD), represented by $\langle \Delta \boldsymbol{X}^2 \rangle \sim nD^*t$, where n, D^*, and t correspond to dimension, Brownian coefficient, and time, respectively.

However, the Brownian motion of droplets exhibits pronounced energy dissipation at the interface, a phenomenon not considered in Einstein's deduction based on the rigid body assumption. Particularly, a comprehensive investigation into the differences between two types of thermal noises—composition noise and random body force—is conducted. Although the fluctuation-dissipation theorem prescribes similar formulations for both noises in prior stochastic phase-field models [20], and Langevin mechanics [94], their dissipation mechanisms are significantly diverse. The composition noise stems from fluctuations in chemical free energy and is mitigated by surface tension, while the random body force arises from kinetic energy perturbations and dissipates via Stokes' drag force. An essential motivation for studying noises prior to PS lies in the recognition that thermal noise can profoundly impact late-stage PS by influencing droplet coalescence driven by Brownian motion.

To evaluate the multicomponent Cahn-Hilliard model, simulations are conducted to replicate the formation of multi-layer polymeric emulsions through liquid-liquid phase separation. The evolution of local composition within the droplets during the emulsification process is meticulously tracked, allowing for analysis of the kinetics governing the establishment of 'onion-like' multi-layer structures. The simulation outcomes highlight that surface energy minimization competes significantly with spinodal decomposition in determining transient morphologies of emulsion droplets. Manipulating surface tension, size, and composition of the mixture reveals a spectrum of intermediate microstructures, ranging from multi-chambered droplets to micro-satellite particles. The insights garnered from this study, encompassing multiple emulsion formations via kinetics analysis, offer promising prospects for the advancement of multi-phase microfluidic manipulation technology across diverse applications.

It is essential to emphasize that the CH model exclusively accounts for diffusion as the primary mechanism driving PS. In the study of multi-layer emulsions, minor divergences in morphological evolution between simulation and experiment are attributed to fluid flow phenomena, such as Marangoni flow—an aspect overlooked in the CH model but pervasive in real fluid systems. Consequently, the hydrodynamic effect is explicitly addressed in the CHNS model. To evaluate the multicomponent Cahn-Hilliard-Navier-Stokes model, investigations are conducted concerning the formation of Janus droplets through thermally induced liquid-liquid phase separation. Analogous to the CH model, this study examines the interplay between two dominant mechanisms shaping morphological evolution: i) the diffusion-dominated phase separation process, and ii) interfacial energy minimization. The interplay of these factors yields a diverse array of transient droplet morphologies, including polygonal structures and patchy droplets. Importantly, the significance of the hydrodynamic effect is underscored within the CHNS model. Due to the constrained diffusivity of entangled long polymer chains, the Marangoni effect induced by composition inhomogeneity becomes comparable to the diffusion of polymeric species. Consequently, the phase separation process and droplet coalescence are significantly accelerated by the Marangoni flow, resulting in a broad spectrum of Janus droplet sizes. The CHNS model, by virtue of its simulation of Janus droplet formation, advances the comprehension of morphological evolution during PS, with potential applicability to a myriad of complex fluid systems. This model's versatility renders it amenable to applications in microfluidics, droplet manipulation, and related domains.

Subsequently, the study extends to the multi-component electro-hydro-thermodynamic CHNSG model, focusing on elucidating droplet behaviors influenced by the interplay of diffusion, hydrodynamics, and electric fields. The total energy functional for both leaky and perfect dielectric materials is derived, and the corresponding energy law is presented. The validation of this model against Taylor and Feng's classical theories is meticulously carried out in a 2D context. Notably departing from earlier models, this work revisits the expression for the electrochemical potential (μ) and introduces a dielectric-related correction term to accurately recapitulate the models. This modification in the chemical potential engenders a generalized electro-hydro-thermodynamic force, encompassing Kortweg stress and Maxwell stress. Consequently, the thermodynamic equilibrium is profoundly influenced by the electric field, elucidating the observed reduction in surface tension induced by the electric field in numerous experiments. Additionally, ternary spinodal decomposition and ternary droplet coalescence are investigated within the multi-component model, considering the intricate interplay of composition field, velocity field, and electric field. The fluid's behavior in this scenario diverges significantly from that observed in the CH and CHNS models due to these interactions. The impact of the electric field on interfacial tension is examined from a thermodynamic perspective, yielding good agreement with Gibbs' phase law. A mechanism elucidating the reduction in interfacial tension, associated with the orientation of the interface in response to the electric field, is also presented. The study carefully deliberates on the influence of the electric field on the phase separation process. Notably, as the electric field strength increases, PS transitions from droplet or bi-continuous structures to lamellar structures parallel to the external electric field. The CHNSG model holds promise for potential applications in the design of electronic devices.

7.2. Future directions

The present dissertation primarily delves into an exploration of three phase-field models and their applications pertaining to the phase separation process. In certain complex systems, such as solutions containing long-chain polymeric entities, the behavior of viscoelastic polymer species significantly deviates from that of small molecules, rendering accurate descriptions inadequate via the CH and CHNS models. A thorough review of pertinent literature [95, 96, 97] and discussions concerning the viscoelastic model have been initiated. These discussions hold promise for intriguing observations. For example, when viscoelasticity is integrated, the CHNS model facilitates an investigation into liquid-liquid phase separation within intricate contexts, like living cells and colloid systems. Additionally, stochastic behaviors undergo substantial alterations when droplets engage in Brownian motion within viscoelastic environments. The distinct relaxation time of the viscoelastic surroundings impedes synchronous movement with the droplet, potentially constraining its motion and modifying random motion into non-Gaussian behavior, as observed in experiments [98, 99, 10]. The viscoelastic model provides a platform to explore off-equilibrium multicomponent systems, offering insights into new thermodynamic and dynamic phenomena.

Given that the CHNSG model has been validated to simulate systems with multiple droplets, it can be extended to investigate electrospinning and electrowetting phenomena. The crux lies in the accurate application of boundary conditions on the substrate in contact with the fluid. In the electrospinning process, the substrate acts as the nozzle through which the electrospun polymer solution is extruded. This extension has already been implemented, and future endeavors will involve tests related to Taylor cone formation. In the context of electrowetting, the substrate functions as the electrode attracting or repelling ionized surfactants. By altering the voltage on the substrate, the surfactant concentration is modified, subsequently altering the contact angle of the sessile droplet. Another crucial extension necessitated by the electrowetting model is the exploration of ionized surfactant electromigration. This has been integrated into the Paced3D model, based on the previous works of our group [100, 101, 102, 103] for the wetting phenomenon, requiring further validation. Leveraging this model, the study of multiple droplet microfluidic systems is facilitated. In previous model [104], droplets were artificially assigned different phase variables to prevent coalescence. However, this approach lacks physical basis, merely mimicking electric interactions between surfactants at the droplet interface to stabilize and prevent coalescence. Future research will apply the ionized surfactant model to simulate intriguing structures, enhancing our understanding of physical processes within living cells.

A. Appendix

A.1. Non-dimensionalization

In this section, the non-dimensionalization process is presented. Here, the most complex Cahn-Hilliard-Navier-Stokes-Gauss model for the leaky material is selected as the example. The characteristic scaling factors for all the other physical parameters are shown in Table 2.1. Substituting the scaling factors into the CHNSG model Eqs. (2.34) (2.35) (2.36) (2.37) and (2.38), resulting in

$$
\begin{gathered}
\frac{\widetilde{\nabla}}{x^*} \cdot (u^* \widetilde{\mathbf{u}}) = 0, \\
\frac{\widetilde{\nabla}}{x^*} \cdot \left(\varepsilon^* \widetilde{\varepsilon} \frac{\widetilde{\nabla}}{x^*} U^* \widetilde{\Psi}\right) = -\rho^{e*} \widetilde{\rho}_e, \\
\rho^{e*} \frac{\partial \widetilde{\rho}_e}{\partial (t^* \widetilde{t})} + \left(u^* \widetilde{\mathbf{u}}\right) \cdot \frac{\widetilde{\nabla}}{x^*} \rho^{e*} \widetilde{\rho}_e = \frac{\widetilde{\nabla}}{x^*} \cdot \left(\sigma^* \widetilde{\sigma} \frac{\widetilde{\nabla}}{x^*} U^* \widetilde{\Psi}\right), \\
\mu_i = f^* \frac{\partial \widetilde{f}}{\partial c_i} - 2 \frac{\gamma^* \widetilde{\kappa \epsilon}}{x^*} \widetilde{\nabla}^2 c_i - \frac{\varepsilon^*}{2} \frac{\partial \widetilde{\varepsilon}}{\partial c_i} \left(\frac{U^* \widetilde{\nabla} \widetilde{\Psi}}{x^*}\right)^2, \\
\frac{\partial c_i}{\partial (t^* \widetilde{t})} + \left(u^* \widetilde{\mathbf{u}}\right) \cdot \frac{\widetilde{\nabla} c_i}{x^*} = \frac{\widetilde{\nabla}}{x^{*2}} \cdot \left(\frac{x^*}{\sigma^*} D^* \sum_{j=1}^{N} \widetilde{\mathcal{M}}_{ij} \widetilde{\nabla} \mu_j + D^* \widetilde{\xi}_c\right), \\
\rho^* \widetilde{\rho} \left(\frac{\partial (u^* \widetilde{\mathbf{u}})}{\partial (t^* \widetilde{t}\,)} + (u^* \widetilde{\mathbf{u}}) \cdot \frac{\widetilde{\nabla} (u^* \widetilde{\mathbf{u}})}{x^*}\right) = -\frac{\widetilde{\nabla} (P^* \widetilde{P})}{x^*} - \sum_{i=1}^{N} c_i \frac{\widetilde{\nabla} \mu_i}{x^*} - \rho^{e*} \widetilde{\rho^e} \frac{\widetilde{\nabla}}{x^*} (U^* \widetilde{\Psi}) \\
+ \frac{\widetilde{\nabla}}{x^*} \cdot \left[\eta^* \widetilde{\eta} \frac{\widetilde{\nabla} (u^* \widetilde{\mathbf{u}}) + \widetilde{\nabla} (u^* \widetilde{\mathbf{u}}^T)}{x^*}\right].
\end{gathered}
$$

After simplification, the non-dimensionalized form of the Cahn-Hilliard-Navier-Stokes-Gauss equation reads

$$
\begin{gathered}
\widetilde{\nabla} \cdot \widetilde{\mathbf{u}} = 0, \\
\widetilde{\nabla} \cdot (\widetilde{\varepsilon}\, \widetilde{\nabla} \widetilde{\Psi}) = -\widetilde{\rho}_e, \\
\frac{\partial \widetilde{\rho}_e}{\partial \widetilde{t}} + \widetilde{\mathbf{u}} \cdot \widetilde{\nabla} \widetilde{\rho}_e = \widetilde{\nabla} \cdot \left(\widetilde{\sigma}\, \widetilde{\nabla} \widetilde{\Psi}\right), \\
\frac{\partial c_i}{\partial \widetilde{t}} + \widetilde{\mathbf{u}} \cdot \widetilde{\nabla} c_i = \frac{\widetilde{\nabla}}{\text{Pé}} \cdot \left(\sum_{j=1}^{N} \widetilde{\mathcal{M}}_{ij} \widetilde{\nabla} \widetilde{\mu}_j + \widetilde{\xi}_c\right), \\
\widetilde{\mu}_i = \frac{\partial \widetilde{f}}{\partial c_i} - 2 \widetilde{\kappa}\, \widetilde{\epsilon}\, \widetilde{\nabla}^2 c_i - \frac{\text{Ca}_E}{2} \frac{\partial \widetilde{\varepsilon}}{\partial c_i} \left(\widetilde{\nabla} \widetilde{\Psi}\right)^2, \\
\widetilde{\rho} \left(\frac{\partial \widetilde{\mathbf{u}}}{\partial \widetilde{t}} + \widetilde{\mathbf{u}} \cdot \widetilde{\nabla}\, \widetilde{\mathbf{u}}\right) = -\frac{\widetilde{\nabla}\, \widetilde{p}}{\text{We}} - \sum_{i=1}^{N} \frac{c_i \widetilde{\nabla} \widetilde{\mu}_i}{\text{We}} - \frac{\text{Ca}_E \widetilde{\rho^e}\, \widetilde{\nabla} \widetilde{\Psi}}{\text{We}} + \frac{\widetilde{\nabla} \cdot [\widetilde{\eta}\, (\widetilde{\nabla}\, \widetilde{\mathbf{u}} + \widetilde{\nabla}\, \widetilde{\mathbf{u}}^T)]}{\text{Re}}.
\end{gathered}
$$

The dimensionless quantities Re, We, Ca, and P$\acute{e}$ are calculated as

$$P\acute{e} = \frac{u^* x^*}{D^*}, \quad Re = \frac{\rho^* u^* x^*}{\eta^*}, \quad We = \frac{\rho^* u^{*2} x^*}{\sigma^*}, \quad \mathrm{Ca}_E = \frac{\varepsilon^* E^{*2} x^*}{\sigma^*}.$$

A.2. List of symbols

Notation	Description
Ω	Domain investigated
S	Domain boundary
$\mathcal{L}$	Total energy functional
$\mathcal{F}$	Chemical free energy functional
$\mathcal{S}$	Entropy
$\mathcal{H}$	Enthalpy
$\mathcal{G}$	Interfacial energy functional
$\mathcal{K}$	Kinetic energy
$\mathcal{U}$	Electrical potential energy
g	Chemical free energy density
f	Bulk free energy density
s	Bulk entropy density
h	Bulk enthalpy density
c_i	Concentration of composition i
c_d	Equilibrium droplet concentration
c_m	Equilibrium matrix concentration
N	Number of components
μ	Electrochemical potential
χ	Flory interaction parameter
γ	Surface tension
κ	Surface tension parameter
ϵ	Interface width parameter
k_B	Boltzmann constant
v_m	Lattice volume
T	Temperature
$\boldsymbol{x}$	Position vector
t	Time
D	Diffusivity
$\mathcal{M}$	Mobility
τ	Kinetic parameter for Allen-Cahn model
$\boldsymbol{\xi}_c$	Thermal composition noise amplitude vector
ξ_a	Thermal phase variable noise amplitude
δ_K	Kronecker's delta
λ	Lagrange multiplier

$\mathbf{u}$	Fluid velocity
p	Hydrostatic pressure
P	Grand potential
ρ	Density
η	Dynamic viscosity
$\underline{\underline{\Theta}}$	Thermodynamic stress tensor
$\boldsymbol{f}_c$	Thermodynamic force
$\underline{\underline{\mathrm{T}}}$	Viscous stress tensor
$\underline{\underline{\sigma}}^M$	Maxwell stress tensor
$\boldsymbol{f}_e$	Dielectric force
E	Surface energy
$\langle \Delta h^2(q) \rangle$	Capillary wave amplitude
q	Capillary wave frequency
u	Electrical energy density
Ψ	Electric potential
$\mathbf{E}$	Electric energy strength
σ	Conductivity
ε	Permittivity
ρ^e	Charge density
C_e	Surface charge density
D	Droplet deformation factor
Δx	Mesh resolution
Δt	Simulation time step
eps	Poisson equation residual threshold
Pé	Pélect number
Cn	Cahn number
We	Weber number
Re	Reynold number
Ca_E	Electro-capillary number

A.3. List of Abbreviations

Abbreviation	**Description**
BC	Boundary condition
BM	Brownian motion
CH	Cahn-Hilliard
CHNS	Cahn-Hilliard-Navier-Stokes
CHNSG	Cahn-Hilliard-Navier-Stokes-Gauss
CW	Capillary wave
CWT	Capillary wave theory
DP	Degree of polymerization
EHTD	Electro-hydro-thermodynamic
FDT	Fluctuation-dissipation theorem
FH	Flory-Huggins
NS	Navier-Stokes equations
Pace3D	Parallel Algorithms for Crystal Evolution in 3D
PF	Phase-field
PDE	Partial differential equation
SD	Spinodal decomposition
NIPS	Non-solvent induced phase separation
TIPS	Thermally induced phase separation
PIPS	Polymerization induced phase separation

List of Figures

1.1. Free energy of mixture for a binary system. (I) Entropy s as a function of the composition c. (II) Enthalpy h by different Flory parameter χ. (III) Free energy density $f = s + h$ with the increase in temperature T. 2

1.2. The schematic binary lattice in 2 dimension. Red and blue dots represent the α and β molecules, respectively. The black stick connecting the dots stands for 3 different bonding types. 3

1.3. (I) The free energy density of a binary system and the equilibrium with the dashed common tangent lines for various temperatures. Square: equilibrium binodal compositions; circle: spinodal compositions. (II) The $c - T$ phase diagram corresponding to (I). 4

1.4. The schematic lattices at the interface. The composition varies from red α phase to blue β phase. At the black dashed cell boundaries, c deviates from the cell center by dc. 6

1.5. Flory-Huggins theory for the binary polymer solution. (I) The schematic polymer solution in 2 dimensional lattice. The degree of polymerization (DP) is 4. Red and blue dots represent the solvent and monomer molecules, respectively. The dark blue stick connecting the monomers stands for covalent bond and the thin dashed line indicates the Van der Waals bond. The red square highlights the entanglement. (II) Free energy density with spinodal and binodal compositions. The common tangent line decides the equilibrium. (III) Phase diagram. 7

1.6. Morphological transition of a binary polymer solution from Ref. [14]. Reproduced with permission. Copyright 2017, American Physical Society. The blue and the red areas represent polymer-rich and solvent-rich phases, respectively. (I) Phase separation with time. (II) The delayed equilibrium of polymer phase which reaches the equilibrium composition c_p slower than the solvent phase ($t_s < t_p$). 8

1.7. Morphological transition of a ternary DEP/ethanol/water solution from Ref. [15]. Reproduced with permission. Copyright 2014, Wiley-VCH Verlag GmbH & Co. KGaA, Weinheim. (I) Schematic illustration of a microfluidic glass capillary. (II) Formation of a quintuple droplet over time (in seconds) from a ternary DEP/ethanol/water mixture (0.41/0.42/0.17 vol %). 10

1.8. (I) Schematic illustration of the evaporation induced surfactant inhomogeneity causes fluid flows from Ref. [16]. Copyright 2020 The Author(s). Published by Elsevier Inc. (II) Formation of multiple ejected droplets from the central large drop via phase separation with Marangoni effect from Ref. [17]. The mass fraction of alcohol is increased from 0.4 (left) to 0.5 (right), which decreases the size of the ejected droplets. 10

1.9. Spontaneous motion of droplets. (I) Phase separation microstructures at different times with an initial concentration $c_0 = 0.25$. (II) Schematic pictures for random and directional motions, respectively. (III) An example of single droplet trajectories from the microstructures shown in (II). (IV) Symbols with different colors depict the dimensionless displacements of different droplets shown in (II) as a function of time. The blue straight line illustrates the displacement from Brownian motion and the red dashed line has a slope of 1 corresponding to Marangoni effect. (V) The double droplet motion. Left: Simulation snapshot. Mid: the composition profile of the droplets along the line connecting their centres of mass for two droplets. Right: Enlargement of the composition profile of the left droplet. Reproduced with permission. [20] Copyright 2015, Springer Nature. . . . 12

1.10. Three types of phase separation. (I) Phase diagram. (a) Thermally induced phase separation (TIPS); (b) polymerization induced phase separation (PIPS); (c) non-solvent induced phase separation (NIPS). The open black circle and red square denote the start and end state, respectively. (II) Schematic pictures for phase separation with time. 13

2.1. (a) The blue area denotes the bulk region updated by Eqs. (2.34) (2.35) (2.36) (2.37) (2.38) and (2.39), and the grey cells stand for the boundary where corresponding boundary conditions are adopted. (b) The staggered mesh for the numerical discretization. Four neighboring cells with solid point: scalar variable position in the bulk, hollow point: scalar variable position on the boundary. The vectors, such as the velocity $\boldsymbol{u}$, the electric field strength $\nabla\Psi$, the diffusion flux $\nabla\mu_i$, and the noise term $\boldsymbol{\xi}_i$ in the x (or z), y dimensions are described by the triangle and the square, respectively (dark grey for the boundary, light blue for the bulk). 31

3.1. The numerical convergence of the stochastic Cahn-Hilliard-Navier-Stokes model with composition noise $\boldsymbol{\xi}_i = 0.001$ for a droplet with $r_0 = 20$. (I) The initial filling. The color bar denotes the droplet concentration c_{P}. (II) and (III) show the pressure distribution and the velocity field, respectively, for $\Delta x = 1.0$ at $t = 1 \times 10^4$. The color bars beneath the figure scale the corresponding values. (IV) The Brownian coefficient D^* and the interfacial tension γ with respect to Δx. (V) and (VI) The normalized Young-Laplace pressure $\langle \Delta \mathrm{p} \rangle / \Delta \mathrm{p}^*$ averaged over 1×10^4 frames with Δx and eps, respectively. 37

3.2. Validation of the stochastic CHNS model with the capillary wave theory. Open colored symbols: with hydrodynamics; dashed color lines: without hydrodynamics. (a) The initial unperturbed flat interface. (b) The capillary wave amplitudes $\langle \Delta \widetilde{h}^2(q) \rangle$ according to Eq. (3.7) in the reciprocal space for the perturbed interface with different composition noise amplitudes ξ_i. (c) $\langle \Delta \widetilde{h}^2(q) \rangle$ versus q for different interfacial tensions, γ at noise amplitude $\xi_i = 0.05$. (d) $\langle \Delta \widetilde{h}^2(q) \rangle$ versus q for different viscosities η with noise amplitude $\xi_i = 0.1$. The black solid lines guide the capillary wave theory relationship of $\langle \Delta \widetilde{h}^2(q) \rangle \sim q^{-2}$. The dotted, solid, and dot-dashed lines show different scaling laws, $\langle \Delta \widetilde{h}^2(q) \rangle \sim q^{-1}$, $\sim q^{-2}$, and $\sim q^{-4}$, respectively. 38

3.3. n-dimensional Brownian motion induced by composition noises. (I) Trajectories of the droplet with radius $r_0 = 40$ in (a) 1D, (b) 2D, and (c) 3D. The color bar measures the time sequence. (II) The simulated velocity histograms in (a) 1D, (b) 2D, and (c) 3D, each fitted by half-normal (black line), Rayleigh (red line), and Maxwell (blue line) distributions, respectively. (III) The simulated displacement histograms in x direction, (a) 1D, (b) 2D, and (c) 3D, fitted by normal distributions (solid colored lines). (IV) The mean squared displacement (MSD) $\langle \Delta \mathbf{X}^2 \rangle$ decreases with the dimension n, which disobeys the Einstein-Stokes relation $\langle \Delta \mathbf{X}^2 \rangle \sim nD^* t$. The solid line guides the $\sim t$ tendency. 42

3.4. Equipartition theorem for the composition noise. (I) Droplet Brownian coefficient D^* in different dimensions following distinct scaling laws with the radius r_0, which are guided by the colored lines. Only 2D BM follows the Einstein-Stokes relation $D^* \sim r_0^{-1}$. (II) Contrived example of two types of noise-induced droplet motions based on the lattice model. (a) Composition noise propels only the interface obeying Fick's first law; (b) Random body force displaces the whole droplet following Newton's second law. 43

3.5. Energy dissipation of composition noise perturbed interface. (I) Interface height changes Δh at $t = 100$. (a) 2D, and (b) 3D (the color bar scales Δh). (II) Dispersion relation with different dimensions shows stronger damping for long wave perturbations (small wavevector $\mathbf{q}$). The capillary wave amplitude $\langle \Delta \widetilde{h}^2(\mathbf{q}) \rangle$ for 2D (red lines) and 3D (blue lines) cases with different interface scale L. 46

3.6. 2D Brownian motion of droplets by CHNS model. (a) The Brownian motion coefficient D^*, upper: with noise amplitude ξ_i; mid: with initial radius r_0; lower: with kinetic parameter τ, the dashed red lines guide the $D^* \propto \xi_i^2$, $1/r_0$, and $\mathcal{M}$ relations, respectively. (b) The probability density function (PDF) of particle velocity follows the Rayleigh distribution. Upper: with ξ_i; lower: with r_0. (c) The particle trajectory. The color bar scales the time sequence. 47

3.7. 2D Brownian motion of a droplet for increasing hydrodynamics (Weber number We) with an initial radius $r_0 = 20$ with the composition noise amplitude $\xi_i = 0.001$: (a) Mean squared displacement with time. (b) Upper: the probability density function (PDF) of the velocity; lower: Brownian coefficient D^* with We. (c) Velocity field at $t = 200$. The black circles mark the particle-matrix interface with $\phi = 0.5$. The color bar (log) scales the velocity magnitude. (d) Power spectral density (PSD) of the particle displacement with the wavenumber q shows Brownian relationship $PSD \propto q^{-2}$. 50

3.8. The phase diagram of Brownian motion with various Weber number We and Péclet number Pé. The initial radius is $r_0 = 20$. CHNS model with the noise amplitude $\xi_i = 0.01$ is studied. (a) The motion phase diagram. The dot-dashed line and the dashed line separate the ballistic motion region (orange) from the standard Brownian motion region (blue) and the geometric Brownian motion region (light blue). The light grey region in between the dashed and dot-dashed lines show the transition area. Some exemplary motion trajectories are shown around: pentagon-standard Brownian motion; square-geometrical Brownian motion; triangle-ballistic motion; circle-transition region. (b) The probability density function (PDF) of the droplet displacement. Simulation: colored dots; normal distribution fitting: solid lines. Upper: x direction; lower: y direction. (c) The MSD $\langle \Delta X^2 \rangle$ and fourth cumulant $\langle \Delta X^4 \rangle$ of the example simulations with time. 51

4.1. (I) Middle: the phase diagram of the DEP-water-ethanol system. The magnitude of the free energy density is described by the heat map (red: high; blue: low). The binodal and spinodal compositions are depicted by the red solid line and dashed line, respectively. The white-black dots indicate the initial compositions for the emulsion droplets considered in the simulation with the initial water content $c_2^0 = 0.029, 0.10, 0.15, 0.20, 0.25, 0.30, 0.40, 0.50$. Surrounding: snapshots (1)-(8) depict the simulated morphologies of droplets at the simulation time $t = 2500$. The corresponding initial setups are sequentially numbered in the phase diagram. The scalar bar denotes 20. The color bar beneath illustrates the oil (DEP) composition for all the simulation snapshots in this work. (II) The experiment morphologies of the emulsions with the reconstructed phase diagram based on the experimental results. Reproduced with permission [15]. Copyright 2014, WILEY-VCH Verlag. 56

4.2. (I) The emulsion droplet with an initial composition $\mathbf{c}^0 = (0.101453, 0.5, 0.398547)$ and radius $r^0 = 16$. (II) Mesh resolution study. (a) The equilibrium composition of DEP and water inside the droplet as a function of mesh size. (b) The equilibrium composition of DEP and water outside the droplet as a function of mesh size. The color bar scales the oil (DEP) concentrations. 57

4.3. Phase diagrams of DEP-water-ethanol system with different Flory-Huggins parameters. Solid dark red lines: binodal; dashed red lines: spinodal. (M) the phase diagram in the main text with $\chi_{12} = 3.0$, $\chi_{13} = \chi_{23} = 0.5$, $\chi_{123} = -3.0$; (T) top: $\chi_{13} = \chi_{23} = -2.0$; (B) bottom: $\chi_{13} = \chi_{23} = 2.0$; (L) left: $\chi_{123} = -6.0$; (R) right: $\chi_{123} = 3.0$. Color bar labels the magnitude of the free energy density f. 59

4.4. (I) The phase diagram of the DEP-water-ethanol system. The binodal and spinodal compositions are plotted with the solid line and dashed line, respectively. The white-red square with error bars depict the simulated spinodal line. The triangles a, b, c, d label four initial compositions to valid the spinodal decomposition with simulation snapshots shown in (II). Two pairs of white-black dots linked with tie lines point the binodal compositions. (III) depicts the validation of the binodal compositions. The color bar scales the oil (DEP) concentrations. 60

4.5. The morphological evolution of the emulsion with respect to the surface tension σ_2. (I) Trajectory diagrams with the kinetic pathways of 3 specific compositions. The red/blue lines trace the compositions with the max/min oil content (c_1) amidst the droplets, while the gold line guides the evolving composition at the droplet center. (a) $\sigma_2/\sigma_2^0 = 10.0$, (b) $\sigma_2/\sigma_2^0 = 5.0$, and (c) $\sigma_2/\sigma_2^0 = 1.0$. All initial setups are consistent with the composition (7) in Fig. 4.1(I). The snapshots beneath the trajectory diagrams picturize the oil distributions at three crucial moments: I (initial), M (mid), and E (end), which are labeled in the respective trajectory diagrams as well. (II) Emulsion morphologies with decreasing σ_2 at an intermediate state ($t = 1250$). From (a) to (f), σ_2/σ_2^0 declines from 10 to 0.1. The scale bar denotes 20. 63

4.6. Morphology diagram with respect to the initial water content c_2^0 and droplet outermost radius r_1. The diagram is divided into three areas: (L), (M), and (R). Typical emulsion morphologies in each area are shown at the top of the figure: (L) Emulsion encapsulating water droplets; (M) onion-like oil-water layers; (R) breakup of oil-rich layers into satellites. The colored circles from red to gray present the number of emulsion layers (from single to septuple), which is in good agreement with the prediction of the dot dashed iso-multiplicity lines fitted with the simulation results. 64

4.7. (I) (a) The emulsion morphology for composition (5) in Fig. 4.1 with the initial radius varying from 10 to 100. The snapshots are taken at the time with maximal multiplicity. (b) The linear scaling law for composition (5) between the radius of ith and $(i+1)$th layers as $r_{i+1} = ar_i + b$. The inset: upper: the dependence of r_i on the initial radius r^0. Lower: the rainbow order colors from red to violet represent the numbers of the oil-water interfaces adding from 1 to 7. (II) and (III) The morphology evolution of the emulsion for the initial compositions (2) and (8) in Fig. 4.1, respectively. All scale bars denote 20. 66

4.8. (I)-(V) The linear scaling law for (a) the radius of the ith layer r_i vs. the radius of initial droplet r^0 and (b) the radius of $(i + 1)$th layer r_{i+1} vs. the radius of its inner successor layer (ith) r_i. (I)-(V) stand for compositions (3)-(7) with initial water composition c_2^0 ranging from 0.2 to 0.4 marked in the Fig. (1) of the main text. The linear relationship between the radius of ith and $(i + 1)$th layers is fitted as $r_{i+1} = ar_i + b$. (VI) The functional relationship for the parameter a vs. initial water composition c_2^0 and b vs. c_2^0. 67

5.1. (I) Left: the ternary phase diagram of the polymer A-polymer B-solvent system at $T = T_H$ ($T_H = 1.05T_c$). The magnitude of the free energy density is described by the heat map (red: high; blue: low). The binodal and spinodal compositions are depicted by the dark red solid lines and dashed lines, respectively. The white triangle indicates the initial compositions with $c_1 = c_2 = 0.15$. The equilibrium compositions of droplet and matrix are labelled with the green circle and the white square, respectively. Right: the phase diagram at $T = T_L$ ($T_L = 0.95\,T_c$). The green circle corresponds to the initial homogeneous composition in the droplet resulting from the phase separation at $T = T_H$. The Janus symbols mark the equilibrium compositions in each Janus hemispheres. (II) Upper row: the microstructure evolution for the production of homogeneous polymer droplets at $T = T_H$. Lower row: the formation of Janus particles via spinodal decomposition when reducing the temperature to $T = T_L$. The simulation domain size is 400 μm × 400 μm. In this work, all the white scale bars denote 50 μm and each color bar scales the polymer composition, if not specified. 73

5.2. The Janus droplet formation with 3 initial radii: 20, 40, and 80 μm. In simulations, all droplets are placed in their individual domains and are stitched in a domain for a better comparison. 75

5.3. (I) The morphological evolution via sub-droplet coalescence by unequal initial polymer A & B composition ratios; upper panel: polymer A:B = 3:7; lower panel: polymer A:B = 7:3. The initial droplet size is 80 μm. (II) The confocal microscopy images of Janus particle formation by the sub-droplet coalescence in the dextran-PEG (green dyed)-Water system. Reproduced with permission from Ref. [76], copyright 2016 WILEY-VCH Verlag GmbH & Co. KGaA, Weinheim. 76

5.4. (I) Left: the equilibrium interfacial tension $\sigma_{\alpha\beta}$ of the A-rich droplet α and B-rich matrix β with the sharp interface model. Right: the schematic integral routine with black open arrow on the phase diagram for the calculation of $\sigma_{\alpha\beta}$ in the Cahn-Hilliard model. (II) The formation of Janus particle via the spinodal decomposition with increasing interfacial tension parameters $\sigma_1 = \sigma_2$. The initial droplet sizes are 20 μm. (III) The contact angle θ between two hemispheres versus $\sigma_1 = \sigma_2$. Black cross: calculated with Eq. (5.5); orange open dot: fitted with simulation. 78

5.5. (I) The free energy density at $T = 0.95\,T_c$ for different Flory parameters χ_{12} between polymer A and polymer B. The light red shadow regions mark the miscibility gaps. (II) The formation of the Janus droplet with the enhancing χ_{12}. The blue highlighted snapshots display the transient pentagon and triangle droplet shapes. The initial droplet sizes are $20\,\mu$m. 80

5.6. (I) The symmetric kinetics of the Janus droplet formation with the same interfacial tensions $\sigma_{13} = \sigma_{23}$. (i) The kinetic pathway of the maximal polymer A rich region (turquoise solid line) and the maximal polymer B rich region (red solid line) on the phase diagram. The dot-dashed lines indicate the tie lines for the pseudo-binary equilibrium between polymer droplets and solvent matrix; (ii) the Janus droplet formation with initial droplet size $r_0 = 20\,\mu$m; (iii) the time sequence of the composition with maximal c_1/c_2 (blue/red solid line). The dot-dashed horizontal line indicates the spinodal composition. (II) The asymmetric kinetics of the Janus droplet formation with unequal interfacial tensions $\sigma_{13} > \sigma_{23}$. The initial droplet size is $20\,\mu$m. (III) The microscopy images of Janus particle formation via the asymmetric phase separation in a three phase system. Bright: dextran (DEX); grey: poly(2-ethyl-2-oxazoline) (PEtOx), and grey matrix: polyethylene glycol (PEG). Reproduced with permission from Ref. [78], copyright 2021, American Chemical Society. 82

5.7. (I) The single Janus droplet formation with asymmetric interfacial tensions $\sigma_{13} > \sigma_{23}$ and the hydrodynamic effect $We = 1.0$. The initial droplet size is $20\,\mu$m. (i) Composition field; (ii) pressure distribution; (iii) velocity field and the stream lines. The white translucent circles mark the Janus droplet interface with solvent composition $c_3 = 0.5$. Each color bar beneath shows the respective magnitude. (II) The asymmetric kinetics of the Janus droplet with the hydrodynamic effect ($We = 1.0$) and unequal interfacial tension $\sigma_{13} > \sigma_{23}$. (i) The kinetic pathway of the maximal polymer A/B dense region (turquoise/red solid line) on the phase diagram. (ii) The time sequence of the composition with maximal c_1/c_2 (blue/red solid line). . . 85

5.8. Janus droplet formation via phase separation with the surface tension of polymer A (σ_{13}) larger than the surface tension of polymer B (σ_{23}). (I) The spinodal decomposition coupling with a weak capillary effect with $We = 1$. Step (i): at high temperature: $T = 1.05\,T_c$; step (ii): at low temperature: $T = 0.95\,T_c$. (II) The spinodal decomposition coupling with a weak capillary effect with $We = 0.01$. (i) High temperature: $T = 1.05\,T_c$; (ii) low temperature: $T = 0.95\,T_c$. The simulation domain size is $400\,\mu\text{m} \times 400\,\mu$m. 87

5.9. Janus droplet formation via phase separation with the surface tension of polymer A (σ_{13}) equal to the surface tension of polymer B (σ_{23}). (I) The spinodal decomposition coupling with a weak capillary effect with $We = 1$. Step (i): at high temperature: $T = 1.05\,T_c$; step (ii): at low temperature: $T = 0.95\,T_c$. (II) The spinodal decomposition coupling with a weak capillary effect with $We = 0.01$. (i) High temperature: $T = 1.05\,T_c$; (ii) low temperature: $T = 0.95\,T_c$. The simulation domain size is $400\,\mu\text{m} \times 400\,\mu$m. 88

6.1. Schematic of the multicomponent fluid system amid the domain Ω within the electric field $\mathbf{E}$. The domain boundary S is colored in grey. The voltages at the top and bottom boundaries are Ψ_1 and Ψ_0, respectively. 92

6.2. (I) The validation with the mesh resolution Δx. Blue dots: deformation factor D with Δx; black hexagons: surface charge density C_e with Δx. (II) Initial filling of the red droplet inside the blue matrix. The scale bar denotes 40 and the colorbar measures the droplet concentration. (III) Charge density ρ_e at $t = 1e4$ scaled by the colorbar below. (IV) (V) and (VI) illustrate the electric potential Ψ, charge density ρ_e, and droplet concentration c at $t = 1e4$ in x and y directions, respectively. 93

6.3. (I) The validation with the Cahn number (Cn=w/d_0). Blue dots: deformation factor D with Cn; black hexagons: surface charge density C_e with Cn. (II) Charge density at $t = 10^4$. Upper row: charge density distribution; lower row: intersections along x and y directions. The upper and lower domain borders are constrained with the electric potential $\Psi_1 = 10$ and $\Psi_0 = 0$, respectively. The scale bar denotes 50 and the colorbar scales ρ_e. (III) Concentration field at $t = 1e4$ with the colorbar below measures the droplet concentration. 94

6.4. Convergence of the droplet deformation factor D and the surface charge density C_e with (I) the residual threshold of Poisson equation eps and (II) the time step Δt. 95

6.5. (I) The droplet deformation factor D with the permittivity ratio $\varepsilon_d/\varepsilon_m$ between droplet and matrix, compared with Taylor's (black dashed line) and Feng's theory (blue solid line). (II)(a) The charge density ρ_e and (b) the concentration distribution c. (III) Left half panel: the velocity field $\mathbf{u}$; right half panel: $|\mathbf{u}|$ scaled by the color bar below. The grey circles mark the droplet interfaces. 96

6.6. The droplet deformation factor D with the conductivity ratio σ_d/σ_m between droplet and matrix, compared with Taylor's (black dashed line) and Feng's theory (blue solid line). 97

6.7. (I) The droplet deformation factor D with the electro-capillary number Ca_E, compared with Feng's theory (blue dashed lines), (a) oblate droplets; (b) prolate drops. (II) The droplet interface with various Ca_E of the oblate drops. Dots: simulated interface positions with $c = 0.5$; lines: elliptical fitting with the least squares method. (III) concentration profiles of the interface intersected at x=0, (a) oblate; (b) prolate. 97

6.8. (I) The schematic equilibrium condition. The free energy densities with and without the electric field strength **E** are depicted with the solid blue and black lines, respectively. The dot-dashed lines are the common tangent at equilibrium, with the open dots marking the equilibrium compositions c with **E** and open squares for c without **E**. (II) The equilibrium concentration c and electric potential Ψ at $t = 1e5$ with the electro-capillary number $\mathrm{Ca}_E = 0.5$. (III) Droplet-matrix interfacial tension $\gamma < 0$ with Ca_E number. The simulated values (open dots) fall on the theoretical line with Eq. (6.7). The red-colored region highlights the interfacial instability with $\gamma < 0$ at $\mathrm{Ca}_E \geq 6.0$. (IV) The interface instability evolves with time at $\mathrm{Ca}_E = 8.0$. The color bar scales the composition. 98

6.9. (I) The schematic phase diagram (PD) of the binary fluid system with temperature T-composition c-electric field strength $|\mathbf{E}|$ obeying the Gibbs' phase rule. (II) The binodal compositions with temperature T are influenced by the electric field and deviate from the black binodal line (**E**= 0). Open dots: simulation as in (III) and (IV); solid colored lines: theory with Eq. (6.8). (III) Equilibrium concentration profile across the interface with temperature T at $\mathbf{E}= \mathbf{0}$ (solid lines) and with **E** (dashed lines) as (II). (IV) Equilibrium electrical field Ψ with temperature T at $t = 1e6$ with $\Psi_1 = 20$ at $y = 0$ and $\Psi_0 = 0$ at $y = 200$. Rest parameters are identical to Fig. 6.2. . 100

6.10. (I) The exemplary composition c and charge density ρ_e perturbed by the composition noise $\xi_c = (0.01, 0.01)$ at $t = 1e5$ with $\mathrm{Ca}_E = 0.1$. The color bar of ρ_e value is in log-scale. (II) The capillary wave amplitudes $\langle \Delta \widetilde{h}^2(q) \rangle$ with the wave frequency q for different Ca_E numbers. The black solid line guides $\langle \Delta \widetilde{h}^2(q) \rangle \sim q^{-2}$. 101

6.11. Ternary phase diagram of an A-B-C system, on which the equilibrium composition of A, B, and C are marked by the red open dot, blue open dot, and purple open square, respectively. The parameters of free energy density are tabulated in Tab. 6.1. The color bar measures the free energy density magnitude. 102

6.12. Ternary droplet coalescence coupled with electro-hydrodynamics. (I) Surface tension dominant coalescence with a weak electrostatic effect, $\mathrm{Ca}_E = 1.0$. (a) The composition field $\boldsymbol{c}$ evolves with time and the color bar shows red for droplet A, blue for droplet B, and purple for matrix C. The velocity field is stacked on the same figure. (b) The evolution of the charge density ρ_e with time and the values are scaled by the color bars beneath the figure. (II) The electric field dominated droplet motion with a strong electrostatic effect, $\mathrm{Ca}_E = 10.0$. The velocity magnitude is measured by the vector cone size, as well as the white-black color bar. 103

6.13. Ternary spinodal decomposition (SP) coupled with electro-hydrodynamics. (I) Surface tension dominant SP with weak $\mathrm{Ca}_E = 1.0$. (a) The composition c stacked by the velocity field (grey cones). Two stretched droplets are highlighted with yellow dot-dashed lines. (b) The charge density ρ_e evolution scaled by the color bars below. (II) The electric field dominated SP with strong $\mathrm{Ca}_E = 10.0$. Some charge-induced vortices are highlighted in white "$\otimes/\odot$" symbols obeying the right-hand rule. 104

List of Tables

2.1. Scaling factors for physical parameters of the Cahn-Hilliard-Navier-Stokes-Gauss model. 30

5.1. Free energy parameters of the ternary system for phase separations. . . 72

6.1. Simulation parameters for the ternary system. 102

Bibliography

[1] A. Dobry and F. Boyer-Kawenoki. "Phase separation in polymer solution". In: *Journal of Polymer Science* 2.1 (1947), pp. 90–100.

[2] H. Tanaka. "Viscoelastic phase separation". In: *Journal of Physics: Condensed Matter* 12.15 (2000), R207.

[3] G. Batrouni and R. Scalettar. "Phase separation in supersolids". In: *Physical Review Letters* 84.7 (2000), p. 1599.

[4] S. Boeynaems, S. Alberti, N. L. Fawzi, T. Mittag, M. Polymenidou, F. Rousseau, J. Schymkowitz, J. Shorter, B. Wolozin, L. Van Den Bosch, et al. "Protein phase separation: a new phase in cell biology". In: *Trends in cell biology* 28.6 (2018), pp. 420–435.

[5] S. S. Dams and I. M. Walker. "[5] Multiple emulsions as targetable delivery systems". In: *Methods in enzymology*. Vol. 149. Elsevier, 1987, pp. 51–64.

[6] Y. Onuki, M. Morishita, and K. Takayama. "Formulation optimization of water-in-oil-water multiple emulsion for intestinal insulin delivery". In: *Journal of controlled Release* 97.1 (2004), pp. 91–99.

[7] J. Bibette, M.-F. Ficheux, F. L. Calderon, and L. Bonnakdar. *Method for releasing an active principle contained a multiple emulsion*. US Patent 6,627,603. Sept. 2003.

[8] P. Couvreur, M. J. Blanco-Prieto, F. Puisieux, B. Roques, and E. Fattal. "Multiple emulsion technology for the design of microspheres containing peptides and oligopeptides". In: *Advanced drug delivery reviews* 28.1 (1997), pp. 85–96.

[9] G. Pontrelli, E. J. Carr, A. Tiribocchi, and S. Succi. "Modeling drug delivery from multiple emulsions". In: *Physical review E* 102.2 (2020), p. 023114.

[10] D. S. Lee, C.-H. Choi, D. W. Sanders, L. Beckers, J. A. Riback, C. P. Brangwynne, and N. S. Wingreen. "Size distributions of intracellular condensates reflect competition between coalescence and nucleation". In: *Nature Physics* 19.4 (2023), pp. 586–596.

[11] A. F. Esfanjani, S. M. Jafari, and E. Assadpour. "Preparation of a multiple emulsion based on pectin-whey protein complex for encapsulation of saffron extract nanodroplets". In: *Food chemistry* 221 (2017), pp. 1962–1969.

[12] J. Weiss, I. Scherze, and G. Muschiolik. "Polysaccharide gel with multiple emulsion". In: *Food Hydrocolloids* 19.3 (2005), pp. 605–615.

[13] J. W. Cahn and J. E. Hilliard. "Free energy of a nonuniform system. I. Interfacial free energy". In: *The Journal of chemical physics* 28.2 (1958), pp. 258–267.

[14] G. Zhang, T. Yang, S. Yang, and Y. Wang. “Morphological-evolution pathway during phase separation in polymer solutions with highly asymmetrical miscibility gap”. In: *Physical Review E* 96.3 (2017), p. 032501.

[15] M. F. Haase and J. Brujic. “Tailoring of high-order multiple emulsions by the liquid–liquid phase separation of ternary mixtures”. In: *Angewandte Chemie* 126.44 (2014), pp. 11987–11991.

[16] R. Van Gaalen, C Diddens, H. Wijshoff, and J. Kuerten. “Marangoni circulation in evaporating droplets in the presence of soluble surfactants”. In: *Journal of colloid and interface science* 584 (2021), pp. 622–633.

[17] G. Durey, H. Kwon, Q. Magdelaine, M. Casiulis, J. Mazet, L. Keiser, H. Bense, P. Colinet, J. Bico, and E. Reyssat. “Marangoni bursting: Evaporation-induced emulsification of a two-component droplet”. In: *Physical Review Fluids* 3.10 (2018), p. 100501.

[18] F. Wang, M. Selzer, and B. Nestler. “On the motion of droplets driven by solutal Marangoni convection in alloy systems with a miscibility gap”. In: *Physica D: Nonlinear Phenomena* 307 (2015), pp. 82–96.

[19] F. Wang, P. Altschuh, L. Ratke, H. Zhang, M. Selzer, and B. Nestler. “Progress report on phase separation in polymer solutions”. In: *Advanced Materials* 31.26 (2019), p. 1806733.

[20] R. Shimizu and H. Tanaka. “A novel coarsening mechanism of droplets in immiscible fluid mixtures”. In: *Nature communications* 6.1 (2015), pp. 1–11.

[21] F. Wang, R. Mukherjee, M. Selzer, and B. Nestler. “Numerical study on solutal Marangoni instability in finite systems with a miscibility gap”. In: *Physics of Fluids* 26.12 (2014).

[22] L. D. Zarzar, J. A. Kalow, X. He, J. J. Walish, and T. M. Swager. “Optical visualization and quantification of enzyme activity using dynamic droplet lenses”. In: *Proceedings of the National Academy of Sciences* 114.15 (2017), pp. 3821–3825.

[23] R. K. Shah, J.-W. Kim, and D. A. Weitz. “Janus supraparticles by induced phase separation of nanoparticles in droplets”. In: *Advanced Materials* 21.19 (2009), pp. 1949–1953.

[24] T. Nisisako. “Recent advances in microfluidic production of Janus droplets and particles”. In: *Current opinion in colloid & interface science* 25 (2016), pp. 1–12.

[25] E. Poggi and J.-F. Gohy. “Janus particles: from synthesis to application”. In: *Colloid and Polymer Science* 295.11 (2017), pp. 2083–2108.

[26] F. Wang, L. Ratke, H. Zhang, P. Altschuh, and B. Nestler. “A phase-field study on polymerization-induced phase separation occasioned by diffusion and capillary flow—a mechanism for the formation of porous microstructures in membranes”. In: *Journal of Sol-Gel Science and Technology* 94 (2020), pp. 356–374.

[27] Z. Dong, H. Cui, H. Zhang, F. Wang, X. Zhan, F. Mayer, B. Nestler, M. Wegener, and P. A. Levkin. “3D printing of inherently nanoporous polymers via polymerization-induced phase separation”. In: *Nature communications* 12.1 (2021), p. 247.

[28] H. Zhang, Y. Wu, F. Wang, F. Guo, and B. Nestler. “Phase-Field Modeling of Multiple Emulsions Via Spinodal Decomposition”. In: *Langmuir* 37.17 (2021), pp. 5275–5281.

[29] F Wang, A Choudhury, M Selzer, R Mukherjee, and B Nestler. “Effect of solutal Marangoni convection on motion, coarsening, and coalescence of droplets in a monotectic system”. In: *Physical Review E* 86.6 (2012), p. 066318.

[30] D. Saville. “Electrohydrodynamics: the Taylor-Melcher leaky dielectric model”. In: *Annual review of fluid mechanics* 29.1 (1997), pp. 27–64.

[31] D. Das and D. Saintillan. “Electrohydrodynamics of viscous drops in strong electric fields: numerical simulations”. In: *Journal of Fluid Mechanics* 829 (2017), pp. 127–152.

[32] P. J. Flory. “Thermodynamics of high polymer solutions”. In: *The Journal of chemical physics* 10.1 (1942), pp. 51–61.

[33] P. C. Hohenberg and B. I. Halperin. “Theory of dynamic critical phenomena”. In: *Reviews of Modern Physics* 49.3 (1977), p. 435.

[34] X. Liu, Z. Chai, and B. Shi. “A phase-field-based lattice Boltzmann modeling of two-phase electro-hydrodynamic flows”. In: *Physics of Fluids* 31.9 (2019), p. 092103.

[35] Y. Lin. “Two-phase electro-hydrodynamic flow modeling by a conservative level set model”. In: *Electrophoresis* 34.5 (2013), pp. 736–744.

[36] B. Van Poppel, O. Desjardins, and J. Daily. “A ghost fluid, level set methodology for simulating multiphase electrohydrodynamic flows with application to liquid fuel injection”. In: *Journal of Computational Physics* 229.20 (2010), pp. 7977–7996.

[37] G. Tomar, D. Gerlach, G. Biswas, N. Alleborn, A. Sharma, F. Durst, S. W. Welch, and A. Delgado. “Two-phase electrohydrodynamic simulations using a volume-of-fluid approach”. In: *Journal of Computational Physics* 227.2 (2007), pp. 1267–1285.

[38] Y. Zu and Y. Yan. “A numerical investigation of electrohydrodynamic (EHD) effects on bubble deformation under pseudo-nucleate boiling conditions”. In: *International Journal of Heat and Fluid Flow* 30.4 (2009), pp. 761–767.

[39] P. Azizian, M. Azarmanesh, M. Dejam, M. Mohammadi, M. Shamsi, A. Sanati-Nezhad, and A. A. Mohamad. “Electrohydrodynamic formation of single and double emulsions for low interfacial tension multiphase systems within microfluidics”. In: *Chemical Engineering Science* 195 (2019), pp. 201–207.

[40] P. Yue, C. Zhou, and J. J. Feng. “Sharp-interface limit of the Cahn–Hilliard model for moving contact lines”. In: *Journal of Fluid Mechanics* 645 (2010), pp. 279–294.

[41] J. A. Stratton. *Electromagnetic theory*. Vol. 33. John Wiley & Sons, 2007.

[42] A. J. Chorin. “A numerical method for solving incompressible viscous flow problems”. In: *Journal of computational physics* 135.2 (1997), pp. 118–125.

[43] H. Zhang, F. Wang, L. Ratke, and B. Nestler. “Brownian motion of droplets induced by thermal noise”. In: *Physical Review E* 109.2 (2024), p. 024208.

[44] K. Huang and I. Szlufarska. “Effect of interfaces on the nearby Brownian motion”. In: *Nature communications* 6.1 (2015), pp. 1–6.

[45] J. Mo and M. G. Raizen. “Highly resolved Brownian motion in space and in time”. In: *Annual Review of Fluid Mechanics* 51 (2019), pp. 403–428.

[46] M. P. Fisher, D. S. Fisher, and J. D. Weeks. “Agreement of capillary-wave theory with exact results for the interface profile of the two-dimensional Ising model”. In: *Physical Review Letters* 48.5 (1982), p. 368.

[47] H. T. Davis. “Capillary waves and the mean field theory of interfaces”. In: *The Journal of Chemical Physics* 67.8 (1977), pp. 3636–3641.

[48] A. Pushkarev and V. Zakharov. “Turbulence of capillary waves—theory and numerical simulation”. In: *Physica D: Nonlinear Phenomena* 135.1-2 (2000), pp. 98–116.

[49] B. Z. Shang, N. K. Voulgarakis, and J.-W. Chu. “Fluctuating hydrodynamics for multiscale simulation of inhomogeneous fluids: Mapping all-atom molecular dynamics to capillary waves”. In: *The Journal of chemical physics* 135.4 (2011).

[50] A. Chaudhri, J. B. Bell, A. L. Garcia, and A. Donev. “Modeling multiphase flow using fluctuating hydrodynamics”. In: *Physical Review E* 90.3 (2014), p. 033014.

[51] A. Choudhury and B. Nestler. “Grand-potential formulation for multicomponent phase transformations combined with thin-interface asymptotics of the double-obstacle potential”. In: *Physical Review E* 85.2 (2012), p. 021602.

[52] A. J. Ladd. “Numerical simulations of particulate suspensions via a discretized Boltzmann equation. Part 2. Numerical results”. In: *Journal of fluid mechanics* 271 (1994), pp. 311–339.

[53] D. Nie and J. Lin. “A fluctuating lattice-Boltzmann model for direct numerical simulation of particle Brownian motion”. In: *Particuology* 7.6 (2009), pp. 501–506.

[54] A. Alexandre, M. Lavaud, N. Fares, E. Millan, Y. Louyer, T. Salez, Y. Amarouchene, T. Guérin, and D. S. Dean. “Non-Gaussian diffusion near surfaces”. In: *Physical Review Letters* 130.7 (2023), p. 077101.

[55] M. V. Chubynsky and G. W. Slater. “Diffusing diffusivity: a model for anomalous, yet Brownian, diffusion”. In: *Physical review letters* 113.9 (2014), p. 098302.

[56] A. Golovin, A Nir, and L. Pismen. “Spontaneous motion of two droplets caused by mass transfer”. In: *Industrial & engineering chemistry research* 34.10 (1995), pp. 3278–3288.

[57] H. Tanaka. “Coarsening mechanisms of droplet spinodal decomposition in binary fluid mixtures”. In: *The Journal of chemical physics* 105.22 (1996), pp. 10099–10114.

[58] L. Shang, Y. Cheng, and Y. Zhao. “Emerging droplet microfluidics”. In: *Chemical reviews* 117.12 (2017), pp. 7964–8040.

[59] W. Li, L. Zhang, X. Ge, B. Xu, W. Zhang, L. Qu, C.-H. Choi, J. Xu, A. Zhang, H. Lee, et al. “Microfluidic fabrication of microparticles for biomedical applications”. In: *Chemical Society Reviews* 47.15 (2018), pp. 5646–5683.

[60] L. D. Zarzar, V. Sresht, E. M. Sletten, J. A. Kalow, D. Blankschtein, and T. M. Swager. “Dynamically reconfigurable complex emulsions via tunable interfacial tensions”. In: *Nature* 518.7540 (2015), pp. 520–524.

[61] M. F. Haase, K. J. Stebe, and D. Lee. “Continuous fabrication of hierarchical and asymmetric bijel microparticles, fibers, and membranes by solvent transfer-induced phase separation (STRIPS)”. In: *Advanced Materials* 27.44 (2015), pp. 7065–7071.

[62] N. G. Min, M. Ku, J. Yang, and S.-H. Kim. “Microfluidic production of uniform microcarriers with multicompartments through phase separation in emulsion drops”. In: *Chemistry of Materials* 28.5 (2016), pp. 1430–1438.

[63] Q. Zhang, M. Xu, X. Liu, W. Zhao, C. Zong, Y. Yu, Q. Wang, and H. Gai. “Fabrication of Janus droplets by evaporation driven liquid–liquid phase separation”. In: *Chemical Communications* 52.28 (2016), pp. 5015–5018.

[64] S. Geiger, S. Tokgoz, A. Fructus, N. Jager-Lezer, M. Seiller, C. Lacombe, and J.-L. Grossiord. “Kinetics of swelling–breakdown of a W/O/W multiple emulsion: possible mechanisms for the lipophilic surfactant effect”. In: *Journal of Controlled release* 52.1-2 (1998), pp. 99–107.

[65] N. Gaiti, A. Aserin, and Y. Cohen. “Mechanistic considerations on the release of electrolytes from multiple emulsions stabilized by BSA and nonionic surfactants”. In: *Journal of controlled release* 29.1-2 (1994), pp. 41–51.

[66] J. Jiao and D. J. Burgess. “Rheology and stability of water-in-oil-in-water multiple emulsions containing Span 83 and Tween 80”. In: *Aaps Pharmsci* 5.1 (2003), pp. 62–73.

[67] D. M. Mueth, J. C. Crocker, S. E. Esipov, and D. G. Grier. “Origin of stratification in creaming emulsions”. In: *Physical review letters* 77.3 (1996), p. 578.

[68] H. Zhang, F. Wang, and B. Nestler. “Janus Droplet Formation via Thermally Induced Phase Separation: A Numerical Model with Diffusion and Convection”. In: *Langmuir* 38.22 (2022), pp. 6882–6895.

[69] M. Rubinstein, R. H. Colby, et al. *Polymer physics*. Vol. 23. Oxford university press New York, 2003.

[70] Y. Zhao, P. Inbar, H. P. Chokshi, A. W. Malick, and D. S. Choi. “Prediction of the thermal phase diagram of amorphous solid dispersions by Flory–Huggins theory”. In: *Journal of pharmaceutical sciences* 100.8 (2011), pp. 3196–3207.

[71] M. Yanagisawa, S. Nigorikawa, T. Sakaue, K. Fujiwara, and M. Tokita. “Multiple patterns of polymer gels in microspheres due to the interplay among phase separation, wetting, and gelation”. In: *Proceedings of the National Academy of Sciences* 111.45 (2014), pp. 15894–15899.

[72] L. Wang, M. Pan, S. Song, L. Zhu, J. Yuan, and G. Liu. “Intriguing morphology evolution from noncrosslinked poly (tert-butyl acrylate) seeds with polar functional groups in soap-free emulsion polymerization of styrene”. In: *Langmuir* 32.31 (2016), pp. 7829–7840.

[73] P.-G. de Gennes. “Dynamics of fluctuations and spinodal decomposition in polymer blends”. In: *The Journal of Chemical Physics* 72.9 (1980), pp. 4756–4763.

[74] D. A. Huse. “Corrections to late-stage behavior in spinodal decomposition: Lifshitz-Slyozov scaling and Monte Carlo simulations”. In: *Physical Review B* 34.11 (1986), p. 7845.

[75] T. Küpper and N. Masbaum. “Simulation of particle growth and Ostwald ripening via the Cahn-Hilliard equation”. In: *Acta metallurgica et materialia* 42.6 (1994), pp. 1847–1858.

[76] H. Yuan, Q. Ma, Y. Song, M. Y. Tang, Y. K. Chan, and H. C. Shum. “Phase-Separation-Induced Formation of Janus Droplets Based on Aqueous Two-Phase Systems”. In: *Macromolecular Chemistry and Physics* 218.2 (2017), p. 1600422.

[77] B. Liu, H. Möhwald, and D. Wang. “Synthesis of Janus particles via kinetic control of phase separation in emulsion droplets”. In: *Chemical Communications* 49.84 (2013), pp. 9746–9748.

[78] Q. Song, Y. Chao, Y. Zhang, and H. C. Shum. “Controlled Formation of All-Aqueous Janus Droplets by Liquid–Liquid Phase Separation of an Aqueous Three-Phase System”. In: *The Journal of Physical Chemistry B* 125.2 (2021), pp. 562–570.

[79] A. H. Groeschel, A. Walther, T. I. Loebling, J. Schmelz, A. Hanisch, H. Schmalz, and A. H. Mueller. “Facile, solution-based synthesis of soft, nanoscale Janus particles with tunable Janus balance”. In: *Journal of the American Chemical Society* 134.33 (2012), pp. 13850–13860.

[80] G. H. Ma, Z. G. Su, S. Omi, D. Sundberg, and J. Stubbs. “Microencapsulation of oil with poly (styrene-N, N-dimethyl-aminoethyl methacrylate) by SPG emulsification technique: Effects of conversion and composition of oil phase”. In: *Journal of colloid and interface science* 266.2 (2003), pp. 282–294.

[81] S.-H. Lee, H.-H. Baek, J. H. Kim, and S.-W. Choi. “Core-shell poly (d, l-lactide-co-glycolide)/poly (ethyl 2-cyano-acrylate) microparticles with doxorubicin to reduce initial burst release”. In: *Macromolecular research* 17.12 (2009), pp. 1010–1014.

[82] C.-H. Choi, D. A. Weitz, and C.-S. Lee. “One step formation of controllable complex emulsions: from functional particles to simultaneous encapsulation of hydrophilic and hydrophobic agents into desired position”. In: *Advanced materials* 25.18 (2013), pp. 2536–2541.

[83] C. Cui, C. Zeng, C. Wang, and L. Zhang. “Complex emulsions by extracting water from homogeneous solutions comprised of aqueous three-phase systems”. In: *Langmuir* 33.44 (2017), pp. 12670–12680.

[84] L. Ratke and W. Thieringer. “The influence of particle motion on Ostwald ripening in liquids”. In: *Acta Metallurgica* 33.10 (1985), pp. 1793–1802.

[85] H. Zhang, F. Wang, and B. Nestler. “Multi-component electro-hydro-thermodynamic model with phase-field method. I. Dielectric”. In: *Journal of Computational Physics* 505 (2024), p. 112907.

[86] H. Zhang, F. Wang, and B. Nestler. “Electric-field induced phase separation and dielectric breakdown in leaky dielectric mixtures: Thermodynamics and kinetics”. In: *The Journal of Chemical Physics* 161.4 (2024).

[87] G. I. Taylor. “Studies in electrohydrodynamics. I. The circulation produced in a drop by an electric field”. In: *Proceedings of the Royal Society of London. Series A. Mathematical and Physical Sciences* 291.1425 (1966), pp. 159–166.

[88] J. Q. Feng. “A 2D electrohydrodynamic model for electrorotation of fluid drops”. In: *Journal of colloid and interface science* 246.1 (2002), pp. 112–121.

[89] Y. Lin, P. Skjetne, and A. Carlson. “A phase field model for multiphase electrohydrodynamic flow”. In: *International Journal of Multiphase Flow* 45 (2012), pp. 1–11.

[90] D. Das and D. Saintillan. “A three-dimensional small-deformation theory for electrohydrodynamics of dielectric drops”. In: *Journal of Fluid Mechanics* 914 (2021), A22.

[91] X. Ji, R. Li, G. Liu, W. Jia, M. Sun, Y. Liu, Y. Luo, and Z. Cheng. “Phase separation-based electrospun Janus nanofibers loaded with Rana chensinensis skin peptides/silver nanoparticles for wound healing”. In: *Materials & Design* 207 (2021), p. 109864.

[92] M. S. Abbasi, R. Song, and J. Lee. “Breakups of an encapsulated surfactant-laden aqueous droplet under a DC electric field”. In: *Soft Matter* 15.43 (2019), pp. 8905–8911.

[93] A. Kaltbeitzel, K. Friedemann, A. Turshatov, C. Schönecker, I. Lieberwirth, K. Landfester, and D. Crespy. “STED analysis of droplet deformation during emulsion electrospinning”. In: *Macromolecular Chemistry and Physics* 218.9 (2017), p. 1600547.

[94] J. Tóthová, G. Vasziová, L. Glod, and V. Lisỳ. “Langevin theory of anomalous Brownian motion made simple”. In: *European journal of physics* 32.3 (2011), p. 645.

[95] P. Yue, C. Zhou, J. J. Feng, C. F. Ollivier-Gooch, and H. H. Hu. “Phase-field simulations of interfacial dynamics in viscoelastic fluids using finite elements with adaptive meshing”. In: *Journal of Computational Physics* 219.1 (2006), pp. 47–67.

[96] D. Borzacchiello, E. Leriche, B. Blottière, and J. Guillet. “Three-dimensional finite volume computation of viscoelastic fluid encapsulation by phase-field modeling”. In: *Journal of Non-Newtonian Fluid Mechanics* 200 (2013), pp. 52–64.

[97] R. Shen, H. Waisman, and L. Guo. “Fracture of viscoelastic solids modeled with a modified phase field method”. In: *Computer Methods in Applied Mechanics and Engineering* 346 (2019), pp. 862–890.

[98] B. Wang, J. Kuo, S. C. Bae, and S. Granick. “When Brownian diffusion is not Gaussian”. In: *Nature materials* 11.6 (2012), pp. 481–485.

[99] A. V. Chechkin, F. Seno, R. Metzler, and I. M. Sokolov. “Brownian yet non-Gaussian diffusion: from superstatistics to subordination of diffusing diffusivities”. In: *Physical Review X* 7.2 (2017), p. 021002.

[100] Y. Wu, F. Wang, S. Ma, M. Selzer, and B. Nestler. “How do chemical patterns affect equilibrium droplet shapes?” In: *Soft matter* 16.26 (2020), pp. 6115–6127.

[101] F. Wang and B. Nestler. “Wetting transition and phase separation on flat substrates and in porous structures”. In: *The Journal of Chemical Physics* 154.9 (2021).

[102] F. Wang, Y. Wu, and B. Nestler. "Wetting Effect on Patterned Substrate". In: *Advanced Materials* (2023), p. 2210745.

[103] F. Wang, H. Zhang, Y. Wu, and B. Nestler. "A thermodynamically consistent diffuse interface model for the wetting phenomenon of miscible and immiscible ternary fluids". In: *Journal of Fluid Mechanics* 970 (2023), A17.

[104] A Tiribocchi, A Montessori, S Aime, M Milani, M Lauricella, S Succi, and D Weitz. "Novel nonequilibrium steady states in multiple emulsions". In: *Physics of Fluids* 32.1 (2020), p. 017102.